Karlsruhe Institute of Technology

Structural characteristics of Typhoon Sinlaku (2008) during its extratropical transition: an observational study

Strukturelle Eigenschaften von Taifun Sinlaku (2008) während seiner außertropischen Umwandlung: eine Beobachtungsstudie

Diploma Thesis of

Julian F. D. Quinting

in Meteorology

at the Institute for
Meteorology and Climate Research

Reviewer:	Prof. Dr. S. C. Jones
Second reviewer:	Prof. Dr. Ch. Kottmeier

Duration: 15. October 2010 – 17. October 2011

Contents

1. Überblick

Etwa 80 tropische Wirbelstürme entwickeln sich jedes Jahr über den Ozeanen und sind verantwortlich für ökonomische und sozio-ökonomische Schäden (Emanuel, 2003). Auf ihrer nordwärtigen Zugbahn (auf der Nordhalbkugel) gelangen etwa 45% Stürme in den Einfluss der Strömung der mittleren Breiten mit der sie auf verschiedene Art und Weise wechselwirken können (Jones, 2003). Die Art der Wechselwirkung entscheidet über eine mögliche Intensivierung des Sturms als außertropisches Tief (außertropische Umwandlung) oder einen baldigen Zerfall. Um eine Einsicht in die Wechselwirkung mit der Strömung der mittleren Breiten zu erhalten und die Konsequenzen dieser Wechselwirkungen besser vorhersagen zu können, wurde im Jahr 2008 die "THORPEX Pacific Asian Regional Campaign" (T-PARC)[1] durchgeführt. Über einen Zeitraum von drei Monaten wurden über dem Pazifik Messungen sowohl während der Entstehung von tropischen Wirbelstürmen als auch während der Umwandlung in außertropische Systeme vorgenommen. Bei den Messungen kam eine Vielzahl von flugzeuggetragenen Instrumenten zum Einsatz: unter anderem Wind-Lidar, Wasserdampf-Lidar, Doppler Radar und Dropsonden. Zahlreiche Messungen fanden während der Umwandlungsphase des Taifuns "Sinlaku" statt. "Sinlaku" entwickelte sich am 08.09.2008 östlich der Philippinen und intensivierte sich zu einem Taifun der vierten Kategorie auf der Saffir-Simpson-Skala. Auf seiner Zugbahn überquerte der Sturm Taiwan und schwächte sich östlich von Japan ab. Auf Grund einer nahezu zonalen Strömung der mittleren Breiten in der Umgebung des Sturms und folglich nicht vorhandenen Wettersystemen der mittleren Breiten (Trog, Rücken) erfolgte keine Umwandlung in ein außertropisches Tiefdrucksystem. Während des Zerfalls des tropischen Wirbelsturms entwickelten sich bei Wechselwirkung mit der baroklinen Zone kräftige konvektive Systeme. Eines dieser Systeme (am 20.09.) wurde während der T-PARC Messkampagne von zwei Messflugzeugen simultan durchflogen und die Struktur mit Hilfe von Dropsonden und einem flugzeuggetragenen Doppler-Radargerät (ELDORA) gut erfasst. Diese Messdaten ermöglichten ein Bild der thermodynamischen und dynamischen Struktur der Konvektion, bzw. des sich abschwächenden Taifuns zu gewinnen.

[1] http://met.nps.edu/~tparc/index.html

Bevor jedoch auf die kleinskalige Struktur der Konvektion eingegangen wird, soll der folgende Absatz eine kurze Übersicht über die synoptische Situation während der außertropischen Umwandlung geben. Bereits am 16.09. stufte der japanische Wetterdienst "Sinlaku" von einem Taifun der ersten Kategorie zu einem tropischen Sturm herab. Vieles deutete zu diesem Zeitpunkt auf eine außertropische Umwandlung hin. Anstatt diese zu vollziehen intensivierte sich der tropische Sturm jedoch wieder und erreichte am 19.09. erneute die Stärke eines Taifuns der ersten Kategorie. Eine genaue Beschreibung der Ereignisse vom 16.09. bis 19.09. findet sich in Sanabia (2010). Am 19.09. zeichnete sich die großskalige synoptische Situation durch ein Tiefdruckgebiet nordöstlich des Sturms, die subtropische Antizyklone südlich "Sinlakus" und einen schwachen Höhentrog westlich von "Sinlaku" aus (s. Abb. 3.2). Diese Anordnung von Taifun zu Tiefdruckgebiet der mittleren Breiten entspricht der in Harr (2000) beschriebenen "Nord-Ost-Wetterlage". Eine Intensivierung des Sturms als außertropisches Tief ist bei dieser Konstellation nicht zu erwarten. Um eine mögliche Wechselwirkung mit dem westlichen und nordöstlichen Höhentrog auszuschließen, wurde der quasigeostrophische Antrieb (Deveson et al., 2002) aus den operationellen Analysen des ECMWF berechnet. Dieses zeigte sowohl am 19.09. als auch am 20.09. in der oberen Troposphähre in der Umgebung "Sinlakus" keine Antriebe für Hebungsprozesse (s. Abb. 3.5). Besonders der schwache Höhentrog westlich des tropischen Sturms zeigte nur schwachen quasigeostrophischen Antrieb, so dass eine Wechselwirkung mit "Sinlaku" ausgeschlossen werden kann. In der unteren Troposphähre hingegen zeigte sich besonders am 20.09., 06 UTC, also zur Zeit der starken Konvektion, ein kräftiger quasigeostrophischer Hebungsantrieb. Dieser Hebungsantrieb lässt sich auf die Wechselwirkung des tropischen Sturms mit der zonal orientierten baroklinen Zone nördlich davon zurückführen: an der Ostseite "Sinlakus" kam es zu starker Warmluftadvektion, die wiederum zu großskaliger Hebung führte. Auf der Westseite hingegen ist ein starker Antrieb für Absinken zu finden, welcher auf Kaltluftadvektion schließen lässt. Die Ausbildung eines Dipols in der Temperaturadvektion während der außertropischen Umwandlung wurde auch von Klein et al. (2000) beobachtet.

Von weiterem Interesse während der Umwandlungsphase war die Ausbildung von Strukturen typisch für die mittleren Breiten. Wie in Harr et al. (2000) beschrieben, kommt es während der außertropischen Umwandlung zu starker Warmfrontogenese nordöstlich der tropischen Stürme. Um "Sinlaku" hinsichtlich der Frontogenese zu untersuchen, wurde diese nach Keyser et al. (1988) berechnet. Es zeigte sich ab dem 19.09., 06 UTC der Beginn einer starken Warmfrontogenese im nordöstlichen Quadranten "Sinlakus" (s. Abb. 3.7). Diese erreichte ihr Maximum von 1.1 $K\ (100km \cdot h)^{-1}$ im Mittel am 20.09., 06 UTC. Damit begann im Gegensatz zu Harr et al. die Frontogenese bereits 30 Stunden vor der von den Wetterdiensten angenommenen außertropischen Umwandlung. Die starke Frontogenese am 20.09. deutet darauf hin, dass "Sinlaku" bereits Strukturen der mittleren Breiten angenommen hatte und sich damit in der außertropischen Umwandlung befand.

In den Satellitenbildern zeigte sich vor der Entwicklung der hochreichenden Konvektion am 20.09. das Vordringen trockener und kalter Luft aus Richtung Japan (s. Abb. 3.2 (b)-(h)). Gleichzeitig deuteten die Wasserdampf-Satellitenbilder auf den Transport feuchter warmer Luftmassen in Richtung der hochreichenden Konvektion hin. Um die Herkunft

dieser Luftmassen zu bestimmen, wurden 48 Stunden Rückwärtstrajektorien berechnet. Diese Trajektorien zeigen, dass die trocken-kalte Luft ihren Ursprung über Japan hat. Innerhalb von 48 Stunden sanken diese Luftmassen um 500 hPa und blieben dabei vergleichsweise trocken mit Werten zwischen $4 - 7\ g\ kg^{-1}$ (s. Abb. 3.4 (a)). Wesentlich feuchtere Luftmassen gelangten in das konvektive Gebiet aus südlichen Richtungen. Trajektorien zeigten, dass diese Luftmassen in der unteren Troposphähre entlang der Westseite der subtropischen Antizyklone nordwärts transportiert wurden. Die spezifische Feuchte war dabei meist höher als $15\ g\ kg^{-1}$. In Vertikalschnitten durch die barokline Zone zeigte sich, dass diese feuchten Luftmassen entlang den nordwärts geneigten Isentropen aufstiegen.
Diese aus der Analyse des ECMWF gewonnenen Einsichten sollen im Folgenden durch die Auswertung von Messdaten aus der T-PARC Messkampagne bestätigt werden.
Verwendung fand dabei das kürzlich von Dr. Michael Bell entwickelte Softwaretool SAMURAI (**S**pline **A**nalysis at **M**esoscale **U**tilizing **R**adar and **A**ircraft **I**nstrumentation). Bei diesem Softwaretool handelt es sich um ein 3D-Var Datenassimilationssystem, welches über die Minimierung einer Kostenfunktion den wahrscheinlichsten Zustand der Atmosphähre aus den Beobachtungsdaten ableitet. Mit einer Auflösung von $5\ km \times 5\ km$ wurden die Beobachtungsdaten (Dropsondendaten, Radardaten, Satellitenwinde) auf einem Gebiet von $400\ km \times 400\ km$ assimiliert und daraus dynamische und thermodynamische Größen abgeleitet. Als Hintergrund für die Datenassimilation diente die operationelle Analyse des ECMWF vom 20.09., 06 UTC. Diese Analyse wurde gewählt, da sie am nächsten an der Beobachtungszeit zwischen 05:00 UTC bis 08:00 UTC liegt.
Eine Analyse der abgeleiteten Felder zeigt verschiedene tropische und außertropische Strukturen, die im Folgenden beschrieben werden sollen. Die Reflektivitätsmuster zeigen zwei grundlegend unterschiedliche Strukturen. Zum einen entwickelt sich südlich der baroklinen Zone ein hochreichend konvektives System mit einem weit nach Süden reichenden Cirrusschirm (s. Abb. 6.2). Nördlich der baroklinen Zone deuten die Reflektivitätsmuster (helles Band und Fallstreifen) auf ein Gebiet mit stratiformem Niederschlag hin (s. Abb. 6.3). Vertikalschnitte durch die beiden Niederschlagsgebiete zeigen in der hochreichenden Konvektionen nahezu senkrechtes Aufsteigen bis in den Cirrusschirm (s. Abb. 6.5 (f)). In die hochreichende Konvektion strömt in der unteren Troposphähre aus Richtung Süden feucht warme Luft ein, die nördlich davon entlang der baroklinen Zone aufsteigt (s. Abb. 6.7 (b)). Dieses Aufsteigen entlang der baroklinen Zone führt zur Ausbildung des stratiformen Niederschlags. Südlich der hochreichenden Konvektion zeigt sich in der feucht-statischen Energie (analog der äquivalent potentiellen Temperatur) eine potentielle Instabilität. Der Bereich des stratiformen Niederschlags ist hingegen gekennzeichnet durch eine stabile Schichtung. Diese resultiert aus dem Aufsteigen der feucht-warmen Luft aus Richtung Süden über eine kalte und trockene nordöstliche Strömung. Der Entwurf eines konzeptionellen Modells für das konvektive System und der Vergleich mit früheren Arbeiten zeigt, dass das konvektive System während der außertropischen Umwandlung Strukturen eines mesoskalig konvektiven Systems aufweist. Größte Übereinstimmungen zeigen sich mit einem konzeptionellen Modell entwickelt von Bryan und Fritsch (2000) (s. Abb. 6.10). Eine detaillierte Beschreibung der Struktur dieses Systems und weiterer Strukturen, wie etwa einer Kaltfront, erfolgt im Kapitel 6.

Bereits die Analyse des ECMWF-Modells zeigte eine starke Warmfrontogenese am 20.09., 06 UTC. Auch in den Beobachtungsdaten bzw. der daraus abgeleiteten SAMURAI Analyse zeigen sich Strukturen einer Warmfront. Dieses sind zum Einen ein zyklonaler Windsprung und zum Anderen ein horizontaler Temperaturgradient von 4 K (70 km)$^{-1}$. Vertikalschnitte durch die Warmfront zeigen eine thermische direkte Zirkulation mit Aufsteigen südlich und Absinken nördlich der Front (s. Abb. 6.11). Um den Einfluss der Frontogenese auf die Vertikalbewegung zu bestimmen, wurde die Divergenz des **Q** Vektors nach Hoskins et al., 1978 berechnet. Konvergenz, die auf positive Vertikalbewegung hindeutet, zeigt sich südlich der Front, Divergenz, die auf Absinken hindeutet, zeigt sich nördlich der Front (s. Abb. 6.18). Dieses lässt darauf schließen, dass die Frontogenese zur Entwicklung der thermisch direkten Zirkulation beigetragen hat. Das Maximum der **Q** Vektor Konvergenz befindet sich im Bereich der hochreichenden Konvektion. Dieses deutet darauf hin, dass die Konvergenz in einer potentiell instabilen Schichtung zu erzwungener Hebung geführt und somit die Entwicklung der starken Konvektion begünstigt hat. Eine Abschätzung über die weitere Entwicklung des Temperaturfeldes erfolgt mit Hilfe der **Q** Vektor Komponenten $\mathbf{Q}_n$ und $\mathbf{Q}_s$. Diese Abschätzung zeigt, dass die Frontogenese noch nicht abgeschlossen ist und sich der Temperaturgradient weiter verstärken wird. Außerdem deutet die Divergenz von $\mathbf{Q}_s$ auf die Entwicklung einer thermischen Welle hin.
Abschließend wird der Unterschied zwischen der Analyse des ECMWF und der Analyse der Beobachtungsdaten erläutert. Insgesamt zeigt die ECMWF Analyse eine Unterschätzung dynamischer und thermodynamischer Größen. Besonders gravierend fällt diese in der unteren Troposphähre aus. Dort werden vor allem die Windgeschwindigkeiten der feuchtwarmen südlichen Strömung sowie der kalten-trockenen östlichen Strömung unterschätzt (s. Abb. 7.3). In Vertikalschnitten zeigt sich zudem, dass die Dynamik der Konvektion nur unzureichend wiedergegeben wird. Während das ECMWF das Aufsteigen entlang der baroklinen Zone wiedergibt, ist die Vertikalbewegung in der starken Konvektion selbst nicht zu finden (s. Abb. 7.4).

Introduction

Each year tropical cyclones (TCs) develop over the oceans and are responsible for economic and social-economic damages all over the world. About 45% of TCs move poleward, recurve and interact with the midlatitude flow (Jones et al., 2003). During this interaction, the decaying tropical cyclones (translation speed $\approx 5\ m\ s^{-1}$) evolve into fast moving and rapidly developing extratropical cyclones (translation speed $\approx 20\ m\ s^{-1}$). This extratropical transition (ET) is accompanied by high impact weather such as intense rainfall, high seas and even hurricane-force winds. As a result, these transforming TCs often pose a serious threat to land and maritime activities at latitudes that do not typically experience these events.

Another important aspect of ET is the influence of the decaying TCs on the synoptic situation in the downstream region (in the northern hemisphere Europe and North America). Almost every year one tropical cyclone that undergoes ET reaches central Europe (Hart and Evans, 2001). Furthermore, the predictability is typically reduced across the downstream region following an ET event. Even high impact weather in the downstream region can be triggered by a downstream development in succession of ET. These impacts occur due to the excitation of large scale propagating Rossby wave-like disturbances which modify the midlatitude flow downstream (Harr, 2010). A big challenge in current meteorological research is, to extend the prediction of possible high impact weather in the downstream region and to understand the main physical processes during the transition.

In response to this challenge the "THORPEX Pacific Asian Regional Campaign" (T-PARC)[2] was conducted in the North Pacific region in summer and autumn 2008. Several tropical cyclones were investigated during this field campaign with various measuring instruments (dropsondes, airborne Doppler radar, lidar). To obtain detailed insights into the tropical cyclones during this period an airborne Doppler radar scanned the structure of mature or decaying TCs. During T-PARC Typhoon Sinlaku underwent ET on 21st of September 2008. Typhoon Sinlaku was investigated with four research aircraft from its development in the tropics to its decay in the midlatitudes. As a result a unique dataset was obtained of its entire lifecycle. Shortly before ET, during the interaction with the midlatitude baroclinic zone, the satellite imagery showed the development of deep convection. Shortly after this development two research aircraft investigated the structure of the deep convection using radar data and dropsondes. The dataset obtained during these research flights presents, therefore, a unique opportunity to gain insight into the structure of the typhoon during its interaction with the baroclinic zone. As a consequence, this

[2] http://met.nps.edu/~tparc/index.html

study focuses on the interaction of Sinlaku with the baroclinic zone and describes the main features during this interaction based on an analysis of operational ECMWF analysis data and the T-PARC observational data. The various observational data (radar, dropsonde, satellite data) are combined in the recently developed 3D-VAR data assimilation software tool SAMURAI. Therefore, the structure of the deep convection is described and analyzed on the basis of the assimilated observational data. In contrast to numerical weather prediction systems, this assimilation technique has the advantage of being a lot closer to observational data and, therefore, to the true state of the atmosphere.
The structure of this thesis is as follows: In chapter 2 the main aspects of tropical cyclones and extratropical transition are explained. Chapter 3 introduces the T-PARC campaign and gives an overview of the synoptic situation during the ET of Typhoon Sinlaku based on the operational analysis of ECMWF. In Chapter 4 the principles of airborne radar meteorology are presented. The chapter closes with a description of the quality control accomplished on the radar raw data. Chapter 5 introduces the background of the 3D-VAR data assimilation technique SAMURAI, including a description of the configuration applied for the data assimilation. The main structures of the typhoon during its interaction with the baroclinic zone identified in the SAMURAI analysis are presented in chapter 6. Moreover, the structural characteristics are brought together to evaluate the interactions between those structures and their impact on the typhoon. Chapter 7 presents a comparison between the ECMWF analysis and the SAMURAI output to identify wrong or missing representations in the ECMWF. The thesis closes with a summary of the main results and a discussion of unanswered questions in chapter 8.

2. Background

2.1 Tropical cyclones

Tropical cylones occur in nearly all ocean basins of the world. Worldwide about 80 TCs develop over the ocean each year (Emanuel, 2003). Favoured conditions for a development are a preexisting atmospheric disturbance equatorward of 5° latitude, sea surface temperatures that exceed $296K$ in an ocean layer of 50 m, high humidity in the mid-troposphere and low vertical shear of the horizontal wind (Riehl, 1950). After the development of a tropical depression (maximum averaged winds of 17 $m\ s^{-1}$) the storms generally move west-northwestwards (west-southwestwards in the southern hemisphere) with a translation speed of $2-10\ m\ s^{-1}$. This translation speed is mainly determined by the background wind (steering flow) in which the cyclone is embedded.
In the case of strong heat transfer from the ocean and low vertical wind shear, the tropical depression can intensify to a tropical storm (maximum averaged winds in the range of 18 to 32 $m\ s^{-1}$) or even a TC (maximum averaged winds greater than 33 $m\ s^{-1}$). Tropical cyclones typically form in the summer or early autumn with a peak activity over the western North Pacific in the late summer. Mature tropical cyclones can be described as approximately axis-symmetric vortices with a strong cyclonic circulation (primary circulation). Winds reach a maximum strength between $10-100\ km$ from the center and decrease outside this area proportional to $r^{-1/2}$, where r is the radius. The maximum winds occur near to the surface and decrease slowly upward. At radii between 100 and 1000 km, the wind speed of the TC becomes indistinguishable from the environmental winds (Emanuel, 2003).
The energy source for tropical cyclones is the latent heat transfer from the warm ocean waters. Due to friction, air spirals in the boundary layer from outer regions towards the cyclone center, which is characterized by a sea level pressure minimum. On its path towards the center the air assimilates energy as a result of strong latent heat fluxes. In the eyewall region (ring/rings of deep convection surrounding the circulation center) convergence forces ascent of the inflowing air along isentropes. Water vapour condenses and assimilated water evaporates to the free atmosphere. As a consequence, the eyewall region

is characterized by the strongest upward motion. Near the top of the storm the air flows out in a divergent region, is deflected by Coriolis force and rotates anticyclonically. The inflow in the planetary boundary layer, the ascent in the eyewall and the outflow at the top of the storm form the secondary circulation. In the case of ideal conditions, TCs can reach high latitudes where they often recurve east-northeastward due to westerly winds in the midlatitudes (on northern hemisphere). On their northward track they usually reach regions with cold water and consequently dissipate. Another possibility is that the cyclones interact with the midlatitude flow and re-intensify as an extratropical cyclone. This process is known as extratropical transition (ET). This transition is accompanied by an increased translation speed as well as asymmetric structures in the wind field, in the thermal structure and in the precipitation pattern.

2.2 Extratropical Transition

The ET of tropical cyclones contains elements of tropical and extratropical meteorology. As a result, it is a big challenge to understand the characteristics and processes during ET and forecast these events as well as possible. Studies in recent years have shown that the acceleration of a TC into midlatitude regions leads on the one hand to an expansion and asymmetry in the wind field (Evans and Hart, 2008) and, on the other hand, to a decrease of the TC's intensity. In addition, large scale forcing of ascent by the midlatitude flow leads to an enlarged region of heavy precipitation. The mechanisms which are responsible for these precipitation events are not well resolved in the current operational techniques. Furthermore, the increasing translation speed during an ET event results in a decreased warning time for high impact weather. As a consequence it is a big challenge to predict high impact weather correctly and to improve forecasts of these complex processes.

Various important physical characteristics have been noticed during the ET process. Many diagnostic and statistical techniques have been developed to define these characteristics which are often related to the interaction between a decaying TC and the midlatitude environment. There have been several approaches to define the ET in the last decades but no consistent operational definition of ET exists until now. The Japan Meteorological Agency (JMA), for example, defined the ET as the dissipation of TC remnants while translating into the midlatitude environment (Kitabake, 2002). Another classification was proposed by Foley and Hanstrum (1994) for the Indian Ocean. They define the ET event as completed when a large-scale easterly flow exists to the south of a decaying cyclone. Evans and Hart (2003) presented the last approach of defining ET which is becoming increasingly used by the operational centers. Their definition gives an objective definition of ET and is based on the 900-600 hPa thickness asymmetry of transforming cyclones. This thickness is strongly influenced by low level frontogenesis that typically occurs during ET (see description below). Due to cold air to the north and warm air to the south the thickness asymmetry can be evaluated optimally by differences between the 900-600 hPa thickness averaged over a semicircle to the north of the cyclone and the 900-600 hPa thickness averaged over a semicircle to the south of the cyclone. Evans and Hart defined

the ET onset by a difference of more than 10 m. The completion of ET was defined by differentiating between a warm-core (tropical cyclone) and a cold-core (extratropical cyclone) structures. By calculating the cyclone isobaric height gradient within a radius of 500 km around the cyclone center a cold-cored cyclone can be identified by an increasing gradient. Hence, a warm-cored cyclone can be identified by an decreasing gradient. The time of ET completion is therefore defined by detecting an increasing gradient. The advantage of Evans' and Hart's method is its objectivity, the fact that it can be calculated quite easily from the height fields and the possibility to estimate the time of ET by using the output of weather predictions systems.

A fourth approach to define the ET and a conceptual model of ET was presented by Klein et al. (2000). In an examination of 30 ET cases they found that almost all cases transformed from a warm-core vortex into a baroclinic, extratropical cyclone. Based on the analysis of infrared satellite imagery they divided the ET into two stages. During the first stage, the transformation stage (Fig. 2.1), the tropical cyclone is located equatorward of the baroclinic zone. The recurved cyclone interacts with the pre-existing lower-tropospheric baroclinic zone. This interaction is accompanied by a low-level dipole of temperature advection (warm temperature advection to the east, cold temperature advection to the west), a vertical motion dipole, the decay of the TC warm core, lower-tropospheric frontogenesis and ascent along the tilted isentropes at the baroclinic zone (Harr et al., 2000). The cloud structure of the remnant TC becomes quite asymmetric during this stage. This asymmetry is mainly caused by vertical shear, meridional moisture variations, orography, decreasing sea surface temperatures and increasing sea surface temperature gradients. The reasons for strong moisture gradients are mainly two different flows advecting completely different air masses. One flow advects dry airmasses from the west and north towards the cyclone. These dry airmasses usually originate from the mid- to upper troposphere and descend on their way towards the cyclone. The dry air on the western side of the cyclone is labeled as 1 in figure 2.1. The dry equatorward flow can be identified in satellite imagery as a dry intrusion (labeled as 2 in Fig. 2.1) and causes little deep convection to the west of the cyclone. The second flow advects warm moist air from the tropics and subtropics along the western border of the subtropical anticyclone (labeled as 3 in Fig. 2.1). This southerly flow enters the southern and eastern quadrant of the tropical cyclone. The result of this moist southerly flow is maintenance of deep convection in these quadrants due to low level instability. The combination of the two flows leads to a completely asymmetric structure of the convection surrounding the cyclone. A closed eyewall, surrounding the cyclone's center does not exist any longer. The characteristic pattern of cloud and precipitation has been defined by Shimazu (1998) as the "delta rain" region. The already mentioned poleward flow of moist, warm air interacts moreover with the midlatitude baroclinic zone (labeled as 4 in Fig. 2.1). The flow ascends along the isentropes of the baroclinic zone and strongly resembles a warm conveyor belt of an extratropical cyclone. Due to the confluence of this warm, upper-tropospheric outflow with the polar jet, usually a cirrus shield with a sharp cloud edge appears to the north of the cyclone. The above described mechanisms proceed until the cloud pattern is similar to that in the upper right panel in figure 2.1. At this stage the transformed cyclone resembles an extratropical cyclone. It is characterized

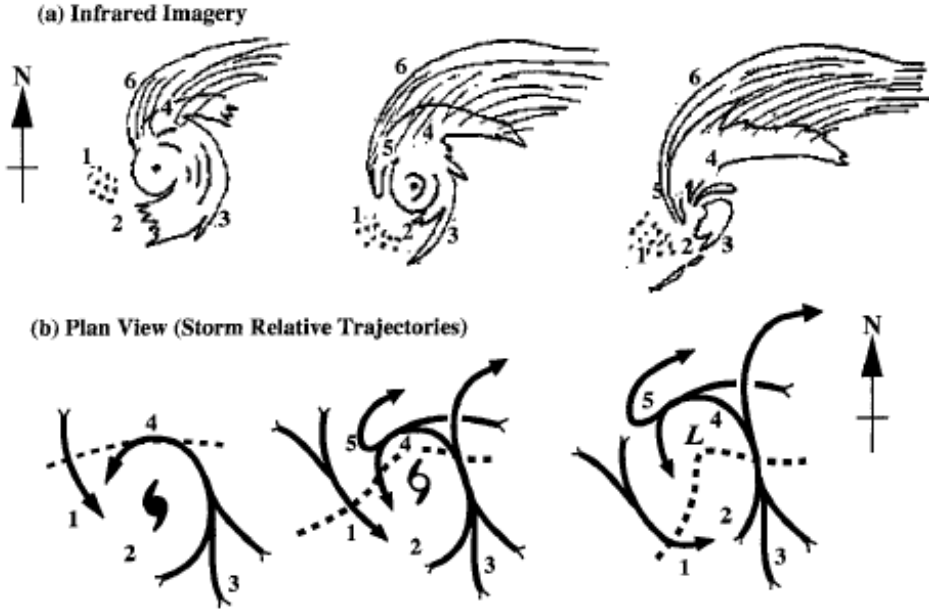

Figure 2.1: Conceptual model of transformation stage of ET, with labeled areas as follows: 1) environmental equatorward flow of cooler, drier air (with corresponding open cell cumulus); 2) decreased tropical cyclone convection in the western quadrant (with corresponding dry slot) in step 1, which extends throughout the southern quadrant in steps 2 and 3; 3) environmental poleward flow of warm, moist air is ingested into tropical cyclone circulation, which maintains convection in the eastern quadrant and results in an asymmetric distribution of clouds and precipitation in steps 1 and 2; steps 2 and 3 also feature a southerly jet that ascends tilted isentropic surfaces; 4) ascent of warm, moist inflow over tilted isentropic surfaces associated with baroclinic zone (dashed line) in middle and lower panels; 5) ascent (undercut by dry-adiabatic descent) that produces cloudbands wrapping westwards and equatorward around the storm center; dry-adiabatic descent occurs close enough to the circulation center to produce erosion of eyewall convection in step 3; 6) cirrus shield with a sharp cloud edge if confluent with polar jet. Fig. 5 from Klein et al., 2000.

by multilayer clouds to the north of the cyclone resembling a midlatitude warm front and a weaker cloud band to the southeast resembling a cold front.

The frontogenesis occurring during the transformation stage and leading to the mentioned cloud pattern has been examined by Harr and Elsberry (2000). The examination of two transforming tropical cyclones showed similar characteristics concerning frontogenesis. The transforming TC, reaching the midlatitude baroclinic zone, leads to the deformation of the temperature field and contributed to warm frontogenesis north and east of the TC center. Furthermore, the cyclonic rotation of the temperature gradient leads to an arching of the baroclinic zone, respectively to the amplification of the thermal wave. The enhancing of the temperature gradient in the warm frontal region results in stronger warm air advection. The strong warm air advection causes on the one hand vertical upward motion, on the other a windshift to the right with height potentially increases the vertical wind shear. In contrast, to the west of the cyclone, sinking motion (labeled as 2 in Fig. 2.1) associated

with advection of cold air contributes to frontolysis. Concerning the time of ET, Harr and Elsberry (2000) detected a remarkable increase of warm frontogenesis 12 hours before the designated time of ET.
Another important factor that contributes to structural changes during ET is the increased vertical wind shear and the consequential vertical tilt in the dynamic structure. These transformations of the TC's structure develop asymmetries in the temperature, vertical motion, precipitation and clouds (Jones, 1995, 2000a,b; Frank and Ritchie, 1999, 2001; Reasor, 2004), whereupon the magnitudes of these changes depend on the strength of the shear and the tilt. Jones (1995, 2000a,b) showed that the magnitude of vertical tilt of TCs depends on the strength of the shear, the strength and the size of the tropical cyclone, the environmental Brunt-Väisälä frequency, and the Coriolis parameter. To remain a balanced flow in a tilted TC warm- and cold anomalies must develop. Jones showed in dry dynamics simulations that the warm anomaly develops on the up-tilt side and a cold anomaly on the down-tilt side of the typhoon. As a consequence the isentropes are perturbed which leads to maximum ascent to the right of the tilt vector and descent to the left of the tilt vector. In these described studies the vertical shear was set to about 2 $m\ s^{-1}(100hPa)^{-1}$. As the vertical shear during an ET event reaches values of more than 5 $m\ s^{-1}(100hPa)^{-1}$, the influence of stronger vertical shear still has to be investigated.
Several studies (Thorncroft and Jones, 2000; Klein et al., 2000) showed that the upper-level potential vorticity (PV) of the decaying TC, defined as $PV = -g\eta\frac{\partial\Theta}{\partial p}$, is eroded due to the strong vertical shear. The outcome of this is a mid- to lower tropospheric PV anomaly, which is either vertically stacked or has a downshear tilt. Jones (2000b) suggested that the erosion of the PV anomaly at upper levels is due to differential advection by the vertical shear or due to pieces of PV breaking off from the main PV anomaly at upper levels.

A westward tilt of PV may also be helpful for re-intensification of the decaying TC to occur. This tilt is associated with an interaction with an approaching upper-level PV anomaly from the west (e.g. strong midlatitude trough). In this case, the re-intensification could proceed as described in the Petterssen scheme (Petterssen and Smebye, 1971). In those situations the type-B cyclogenesis is modified by the lower-level remnants of the tropical cyclone and potentially enhanced due to the reduced stability in the presence of moist tropical air. Klein et al. (2002) found that re-intensification occurred when dynamic and thermodynamic processes created a favorable region for an extratropical development. This favorable region developed especially when the TC outflow enhanced the entrance region of a downstream jet streak and when the TC interacted with the baroclinic zone. Furthermore, the development or non-development in these situations depended strongly on the phasing between the poleward moving TC and the upper-level trough.
The stage of this extratropical development and the deepening as an extratropical cyclone was defined by Klein et al. as the re-intensification stage. Because not all of the decaying TCs necessarily strengthen, but rather dissipate, Jones et al. (2003) called the "re-intensification-stage" as the "extratropical stage". This stage is characterized by an interaction between the decaying TC and a low-level baroclinic zone. This interaction leads to an increased gradient of equivalent potential temperature, an arching of the tem-

perature field and, as a result, to warm frontogenesis. Cold frontogenesis during this stage is often suppressed due to the descent of cold air from upstream of the cyclone (Harr and Elsberry, 2000). In the absence of a strong baroclinic zone, an upper-level trough or another preexisting extratropical system, the remnants of the TC would be expected to continue to decay.

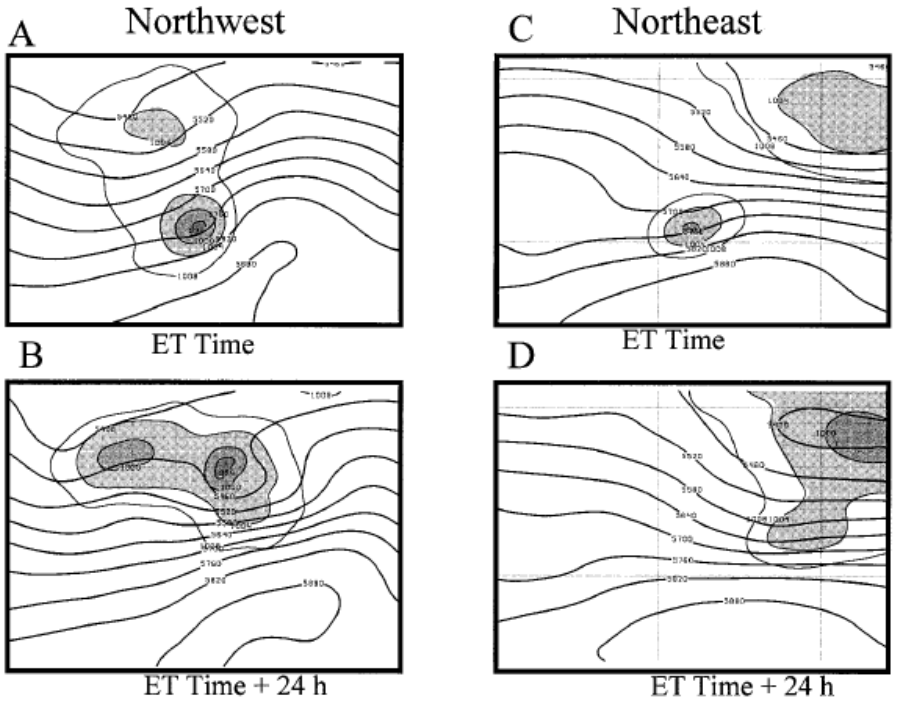

Figure 2.2: Composite 500 hPa height [m] and sea level pressure (hPa, only below 1008 hPa with shading in 4 hPa increments starting at 1004 hPa) analyses based on grouping of cases in a northwest pattern at the ET time (A), (B) ET+24 h, and in a northeast pattern at the (C) ET time and (D) ET+24 h. The composite northwest pattern is based on 13 cases and the northeast pattern is based on 17 cases (Fig. 1 from Harr et al., 2000).

Harr and Elsberry (2000) documented, that the re-intensification is influenced by the primary midlatitude circulation pattern into which the decaying TC moves. They characterized the interaction based on whether the midlatitude circulation (midlatitude low pressure system) was to the northwest or to the northeast of the TC. In the northwest pattern the transforming TC typically moves north-northeast during the re-intensification as an extratropical cyclone. The TC that undergoes ET in the northeast pattern moves eastward into the strong zonal flow between the preexisting midlatitude cyclone and the subtropical ridge to the southeast. As described in Klein et al. (2000), the systems in a northwest pattern tended to have a lower sea level pressure after 36 h of re-intensification than those in a northeast pattern. The two different patterns furthermore influence the strength of the frontogenesis and the following development of a thermal wave. Harr and Elsberry (2000) found out, that in the northeast-pattern the frontogenesis is much weaker than in the northwest-pattern. The weaker frontogenesis results in lower dynamical forcings such as thermal advection and deformation. As a consequence, the thermal wave associated with the transforming cyclone does not amplify significantly. The midlatitude

low to the northeast rather prevents the cyclone from coupling with the upstream midlatitude trough than developing into a separate extratropical cyclone. Instead, the cyclones entering this pattern remain as an open wave and soon decay.
As this short overview on recent studies shows, "the" definition of ET does not exist and still more work needs to be done on this complex process. More research on the influence of vertical shear on TCs during ET is needful as well. Moreover, the downstream impact of tropical cyclones, which is not described in this study, still poses serious problems in numerical weather prediction.

3. Typhoon Sinlaku during T-PARC 2008

The summer phase of the "THORPEX[1] Pacific Asian Regional Campaign" (T-PARC) was conducted together with TCS08[2] during August-October 2008 over the western North Pacific. It focused on the shorter-range dynamics and the forecast skill in the eastern Asian and western North Pacific region, and the downstream impact on the medium-range predictability in North America. The focus of T-PARC/TCS08 was on different aspects of typhoon activity, i.e. formation, intensification, structural changes, motion and ET (Harr and Jones, 2011). For example, the measurement strategy investigated circulations of the tropical North Pacific monsoon environment which were connected with enhanced and reduced periods of deep convection, tropical cyclone formation, tropical cyclone intensification and tropical cyclone structural changes. Another main aspect of the field campaign was a measurement strategy for ET and possible downstream impacts. This strategy was based on the poleward movement of a decaying cyclone and the following extratropical cyclogenesis following an interaction with a midlatitude circulation pattern. In addition, a targeted observation measurement strategy focused on the identification of regions in which additional in situ observations may reduce errors in tropical cyclone track forecasts. As these measurement strategies require operations over a large area (from the tropics to the midlatitudes), four aircrafts (NRL P-3, USAF WC-130J, DLR Falcon, DOTSTAR Astra) were employed to measure the structure of tropical cyclones and the environment surrounding the cyclones with dropsondes, Doppler radar, Doppler wind lidar and DIAL water vapour lidar systems. These aircrafts operated on 76 missions in 515 flight hours. During T-PARC, the operations were conducted on four typhoons, one tropical depression and six non-developing tropical disturbances. 28 missions were conducted on Typhoon Sinlaku, so that measurements are available from the genesis in the tropics to ET. Twelve of these measurement were proceeded during the ET between the 17th and 21st of September. Therefore, Sinlaku was the first case with three aircrafts investigating the tropical cyclone core, the tropical cyclone-midlatitude interface and the midlatitude impact region simultaneously.

[1] http://www.wmo.int/thorpex
[2] http://www.met.nps.edu/~tparc/TCS-08.html

Typhoon Sinlaku developed in the western North Pacific on 8 September and strengthened quickly to typhoon intensity on 9 September 2008. In the following days, Sinlaku tracked northward along 125°E (Fig. 3.1 (a)). On 10 September, the central pressure dropped down to 935 hPa. With maximum winds of 230 km/h, Sinlaku reached the strength of a category four typhoon (based on the Saffir-Simpson-Scale) on this day. Two days later, Sinlaku turned northwestward and approached Taiwan where it made landfall on 13 September. In Taiwan Sinlaku caused heavy precipitation of 626 mm in 24 hours [3]. After landfall, the cyclone weakened rapidly and the central pressure increased to 985 hPa on 14 September.

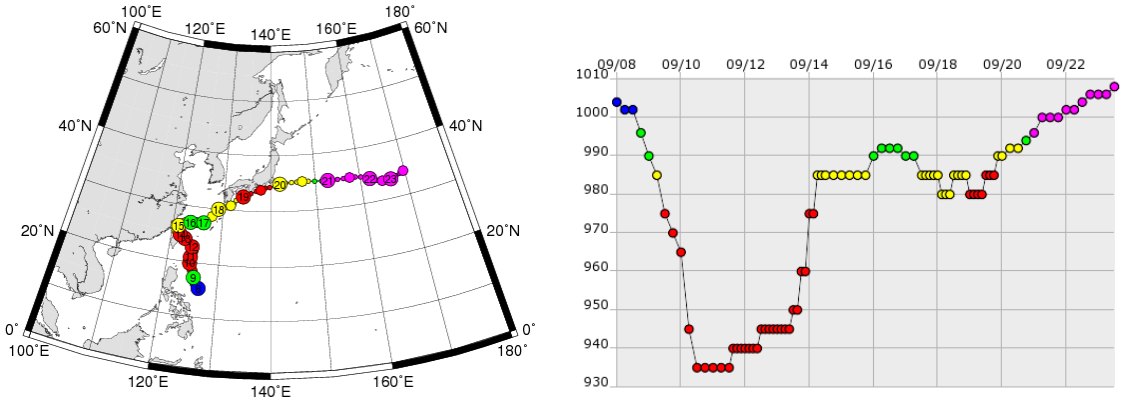

(a) (b)

Figure 3.1: Best track of Sinlaku (a) and central pressure chart (b) (Digital Typhoon).

On the same date, Sinlaku reached its western most position and recurved. Moving east-northeastward over the East China Sea the cyclone weakened to a tropical storm on 16 September. Satellite images show that the Ex-typhoon had a completely asymmetric structure indicating that Sinlaku entered the transformation stage of ET on this day. Surprisingly, Sinlaku did not complete ET but rather re-intensified as a tropical cyclone northwest of the Ryukyu Islands and turned northeastward toward Kyushu. During this re-intensification, several convective bursts occurred on the eastern side of the low level circulation center (Sanabia, 2010) and the convection reorganized to form an eyewall on 19 September. On this day, between 0000-1200 UTC, Sinlaku re-gained typhoon intensity. Although the tropical cyclone was much weaker than during landfall in Taiwan it caused heavy precipitation as well. In Osawe rain of 768 mm in 36 hours was measured. One day later, on 20 September Sinlaku interacted with the baroclinic zone, moved eastward along 35°N but did not re-intensify as an extratropical cyclone. The ET of Sinlaku was investigated by three research aircrafts. The NRL-P3 and the C-130 investigated the convection surrounding the cyclone by dropsondes and airborne radar measurements. These measurements provide insights into the structure of the transforming typhoon on three days. Sinlaku's outflow and the interaction with the polar jet was investigated by the DRL-Falcon with several dropsondes and a DIAL water vapour lidar system.
The focus of this study will be on the analysis and description of a strong convective development which occurred on 20 September during the interaction between Sinlaku and the

[3] http://www.wettergefahren-fruehwarnung.de/Ereignis/20080922_e.html

baroclinic zone. This convective evolution was investigated simultaneously by the NRL P-3 and C-130. Therefore, a unique dataset of observations of the cyclone's interaction with the baroclinic zone exists. These measurements show the small- to mesoscale structure at single point of time. To gain insights into the large-scale temporal evolution between 19 September and 20 September the synoptic situation will be described in the following. To investigate the influence of upper-level forcing or frontogenesis on Sinlaku's ET these mechanisms are evaluated separately. Furthermore, the origin of airmasses being advected towards the cyclone before the deep convective development needs to be studied also. The intent of describing and evaluating large-scall processes is to obtain a first impression of the atmospheric conditions before and during the deep convective development. Its small-scale structure will then be evaluated with the help of observational data later in this study.

3.1 Synoptic situation during the ET of Sinlaku

The following section examines the synoptic-scale flow pattern leading up to the time examined in detail later in this study. The principle data set used here is the ECMWF operational analysis with a horizontal resolution of $0.25° \times 0.25°$. In addition, satellite imagery is used to describe the convective structure during the ET. On 19 September 12 UTC Sinlaku is located at 33.7°N and 138°E to the south of Japan. At this time moderate convection occurs to the northeast of the circulation center with cloud top temperatures of 205 K (Fig. 3.2 (b)). By this time the transforming typhoon has lost a lot of its symmetric structure. In contrast, twelve hours before Sinlaku had a closed eyewall and the cloud pattern was a lot more symmetric. At that time Sinlaku was still classified as a category-one typhoon (Fig. 3.1(b)). To the north of the cyclone a cirrus shield indicates the confluence between the typhoon's outflow and the polar jet (Bader et al., 1995). The flow pattern at upper levels (250 hPa) is determined by a weak trough to the west-northwest of the decaying typhoon and the subtropical anticyclone to the south of Sinlaku (Fig. 3.2 (a)). Furthermore, a deep trough with a corresponding low pressure system is located to the northeast. The axis of this deep trough is along 150°E with the jetstreak of 65 $m\ s^{-1}$ on its southern flank at about 44°N. Thirty six hours earlier the jet streak was much weaker and strengthened until this point of time most probably in response to Sinlaku's outflow. On 19 September, 12 UTC (Fig. 3.2 (a)), Sinlaku is located about 5° south of the jetstream between the three synoptic scale patterns mentioned above. The southern branch of a split jetstream directly to the north of Sinlaku shows at this time maximum winds of 40 $m\ s^{-1}$. The flow pattern resembles the northeast pattern of Harr and Elsberry (2000). As described in Harr and Elsberry (2000) an eastward motion (due to westerly steering flow) of the cyclone can be expected in the following days into the strong zonal flow between the preexisting midlatitude cyclone and the subtropical anticyclone to the south.

The large-scale synoptic flow pattern does not change significantly during the next twelve hours (Fig. 3.2 (c)). The transitioning cyclone has moved east-northeastward into an upper-level zonal flow and is located at 35°N and 142°E still to the southwest of the primary midlatitude circulation pattern with its axis now along 154°E. The jet streak is

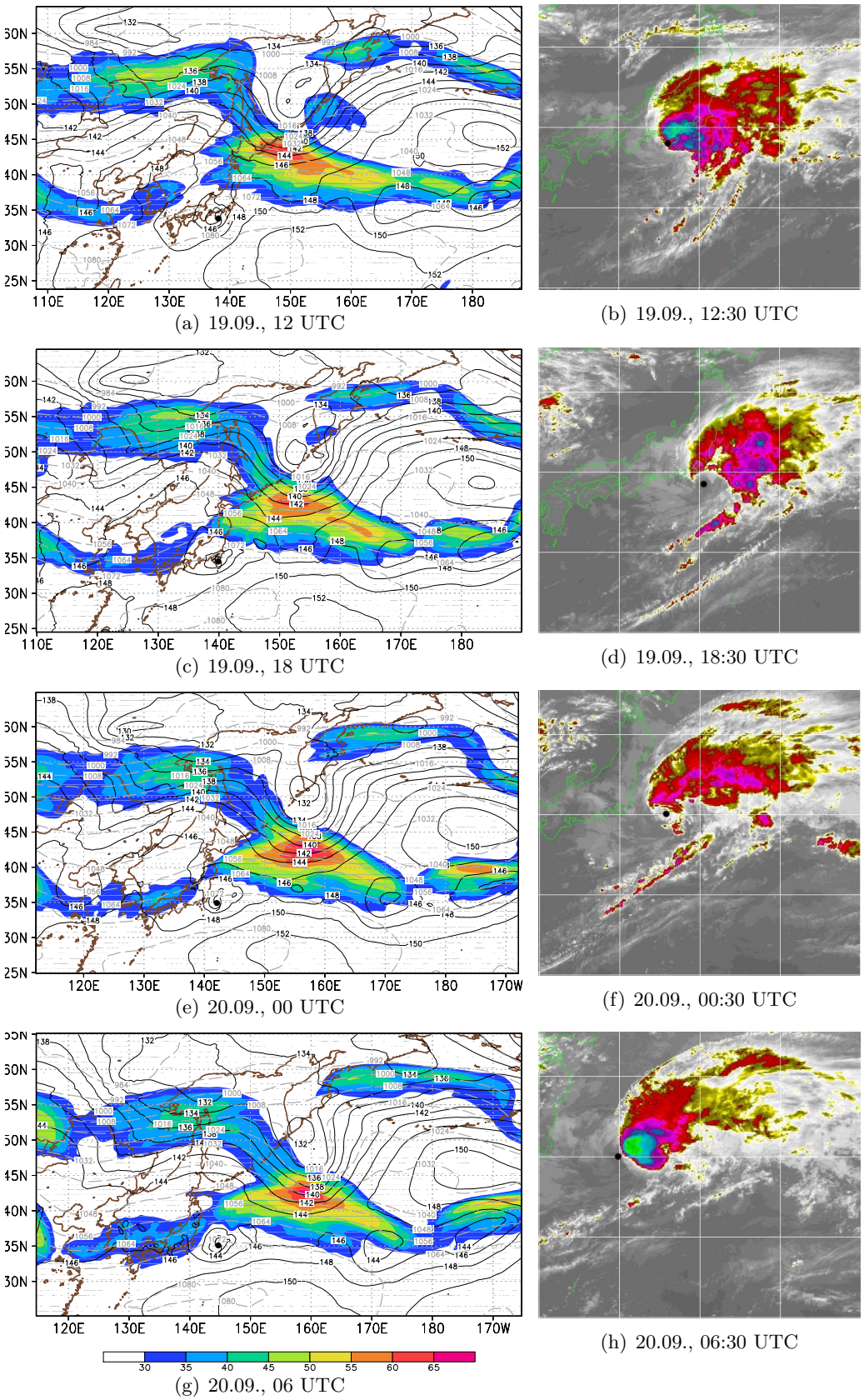

(a) 19.09., 12 UTC

(b) 19.09., 12:30 UTC

(c) 19.09., 18 UTC

(d) 19.09., 18:30 UTC

(e) 20.09., 00 UTC

(f) 20.09., 00:30 UTC

(g) 20.09., 06 UTC

(h) 20.09., 06:30 UTC

Figure 3.2: Wind speed [$m\ s^{-1}$] shaded, geopotential [gpdm] at 850 hPa in black solid contours and geopotential at 250 hPa in grey dashed contours from 19 September, 12 UTC to 20 September, 06 UTC, cyclone symbols denote best track position of Sinlaku; MTSAT IR image from 19 September at 12:30 UTC to 20 September, 06:30 UTC, the black dots highlight position of the low level circulation center.

still located on the southern flank of this low pressure system (Fig. 3.2 (c)). The convection surrounding the cyclone has weakened until this time. There is a broad region of moderate convection to the northeast of the cyclone center and the cloud top temperatures do not reach 215 K (Fig. 3.2 (d)). Some bands of moderate convection extend to the south of the cyclone, suggesting that cold frontogenesis is occurring at this time. An important feature develops on the southern and western side of the TC. Infrared and water vapour satellite imagery show dry air masses being advected towards the cyclone center. The development of this dry intrusion starts on 19 September, 16 UTC. On 19 September, 18:30 UTC, dry air can be seen exactly above the low level circulation center (Fig. 3.2 (d)). The region of dry air extends from the Philippines in the south to South Korea in the north, and from China in the west to the moist air to the east of Sinlaku (not shown). The dry intrusion wrapping around the TC is located between $32°N$ and $35°N$ and extends to $142°E$. It leads to a remarkable drying of Sinlaku's environment, to lower values of convective available potential energy and, as a consequence, to weaker convective activity. Until 20 September, 00 UTC, the dry intrusion wraps around the remnant circulation and seems to reach the circulation center on 20 September, 02 UTC. Measurements of a radiosonde released in Tateno (Japan) at this time show a dry layer above 550 hPa which represent the dry intrusion (Fig. 3.3 (a)). The dry air is advected by west-northwesterly winds towards the cyclone and descends slowly on its way, as trajectory calculations will show later in this study. The dropsonde measurements show also a marked shift with height in the direction of the horizontal wind. Below 800 hPa northerly and easterly winds of 20 $m\ s^{-1}$ can be seen in a moist environment. Above this level, the winds shift to westerly in a much drier environment and strengthen significantly to 40 $m\ s^{-1}$. An explanation for this strong windshift with height is that the remnant circulation of Typhoon Sinlaku is present below 800 hPa and the midlatitude westerly flow above. This strong vertical shear accelerates the TC's decay. Furthermore, the convective available potential energy in the region of the radiosounding does not exceed 200 $J\ kg^{-1}$. This suggests, as mentioned above, that the dry intrusion reduces the potential for convective activity on the western side of the cyclone. This again enhances the asymmetric cloud structure seen in the satellite imagery.

The radiosonde measurements are in agreement with the MTSAT water vapour images as these satellite measurements represent a layer above 600 hPa and exhibit a dry layer as well in this region (Fig. 3.3 (b)). As Fig. 3.3 (a) shows, the ECMWF analysis represents the thermodynamic as well as the dynamic structure quite well. Only in the boundary layer a difference concerning the wind direction and strength exists. A detailed view of this dry intrusion can be found later in this study.
On 20 September 00 UTC, Sinlaku is still located to the south of the jetstreak but now to the east of a weak jet entrance region (Fig. 3.2 (e)). The wind speed in the jetstream to the west of Sinlaku increased by 5 to 10 $m\ s^{-1}$ during the previous six hours. Sinlaku's location to the east of a jet entrance region suggests a restrengthening due to upper level forcing. The upper level forcing affecting the cyclone will be discussed later. However, the synoptic situation with respect to the troughs to the west and the northeast has not changed significantly. The tongue of dry air continues to wrap around the circulation center and is located to the south and east (Fig. 3.2 (f)). The cyclone center is close

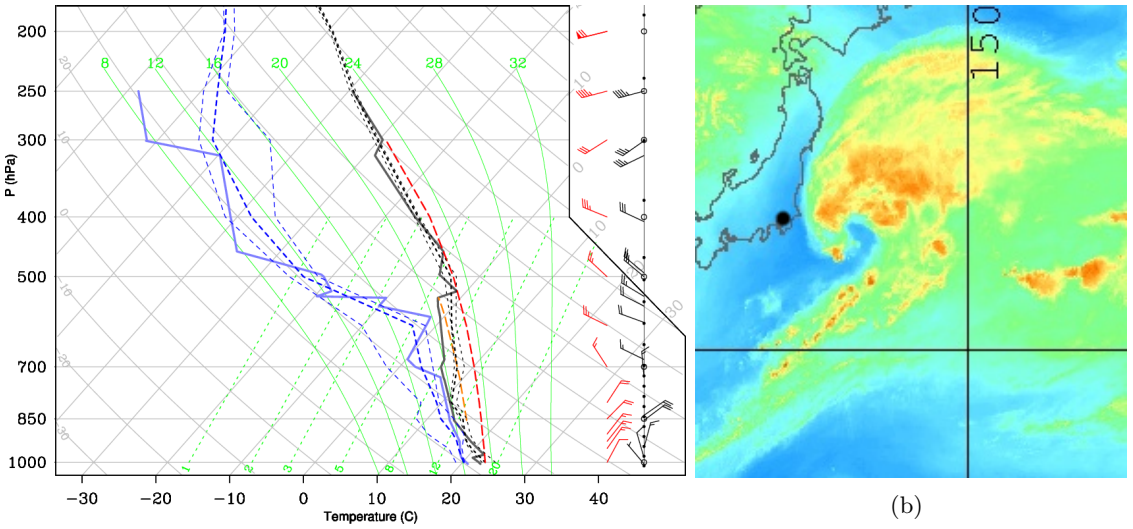

(a) (b)

Figure 3.3: (a) shows measurements of a radiosonde released in Japan on 20 September, 00 UTC (black dot in (b) denotes location of radiosonde measurement) in comparison to ECMWF analysis. Dashed lines show ECMWF analysis (blue=dew point, black=temperature), where the thick dashed line is the ECMWF analysis at the grid point next to the sounding and thin dashed lines are the standard deviation of the ECMWF analysis in a box of 3×3 grid points around the measurement location; solid lines are radiosonde measurements (blue=dew point, black=temperature). Red wind barbs are from ECMWF analysis, black wind barbs are from radiosonde measurements. Yellow dashed line denotes CAPE calculated from radiosounding (186 $J\ kg^{-1}$), red dashed line denotes CAPE calculated from ECMWF analysis (586 $J\ kg^{-1}$). (b) MTSAT water vapour image on 19 September at 23:30 UTC.

to moderate convection to the north which extends eastward to 150° E. The moderate convection is nearly zonally oriented and therefore almost parallel to the baroclinic zone (not shown). This suggests that the moderate convection results from ascent along the northward tilted isentropes of the baroclinic zone.

On 20 September, 06 UTC a weak southern jet approaches Sinlaku from west. The importance of this jet with respect to shear and to the tilt of the cyclone will be evaluated later. A cirrus edge to the north of Sinlaku indicates furthermore the confluence of the cyclone's outflow with the jet to the north. This outflow and the interaction between a cyclone and the polar jet has been investigated in detail for Typhoon Jangmi (2008) by Grams (2011). On 20 September, 06 UTC deep convection develops to the east of the low level circulation center at 144°E and 35°N (Fig. 3.2 (h)). In a time period of one hour the cloud top temperature decreases from 233 K to values of about 195 K in the region of the deep convection. An almost circular expansion of cold cloud tops indicates intense convective development. The system maintains its intensity until 06:30 UTC. With respect to the extent of the system and the cloud top temperatures, the satellite images indicate a mesoscale convective complex (MCC). The necessary criterion for an MCC with cloud top temperatures lower than 221 K in an area of 50,000 square kilometer (Maddox, 1980) is fulfilled in this case in terms of the satellite imagery. The development of this deep convec-

tion is the main focus of this study. However, during its decay the convection departs from the low level circulation center according to the satellite imagery (not shown). A strong steering flow at upper levels of about 20 $m\ s^{-1}$ most probably favors this development. At the end of the decay the deep convective system is located at 150°E and 35°N at 14:00 UTC, whereas the position of the low level circulation center is 148°E and 34°N at this time.

To evaluate the origin of the various air masses being advected toward the cyclone on 20 September, 06 UTC (the time when the convective system developed), 48 h backward trajectories were calculated with the software tool LAGRANTO (Wernli and Davies, 1997). One important question with respect to the structural changes of Sinlaku is the origin of the dry intrusion. As seen in figure 3.3, dry air is located to the west of Sinlaku in a westerly flow. On 20 September, 06 UTC, the ECMWF analysis at 850 hPa shows a tongue of dry air to the south and west of the typhoon (Fig. 3.4 (b)). Backward trajectories with a temporal resolution of one hour were calculated ending in a domain from 140.0°E to 145.0°E and from 32.5°N to 37.5°N in a layer between 900 hPa and 800 hPa. As a second criterion descent of the air parcels during these 48 h is required. With a third criterion the characteristics of the dry intrusion were specified by calculating only those trajectories not exceeding a specific humidity of 7 $g\ kg^{-1}$ at final time.

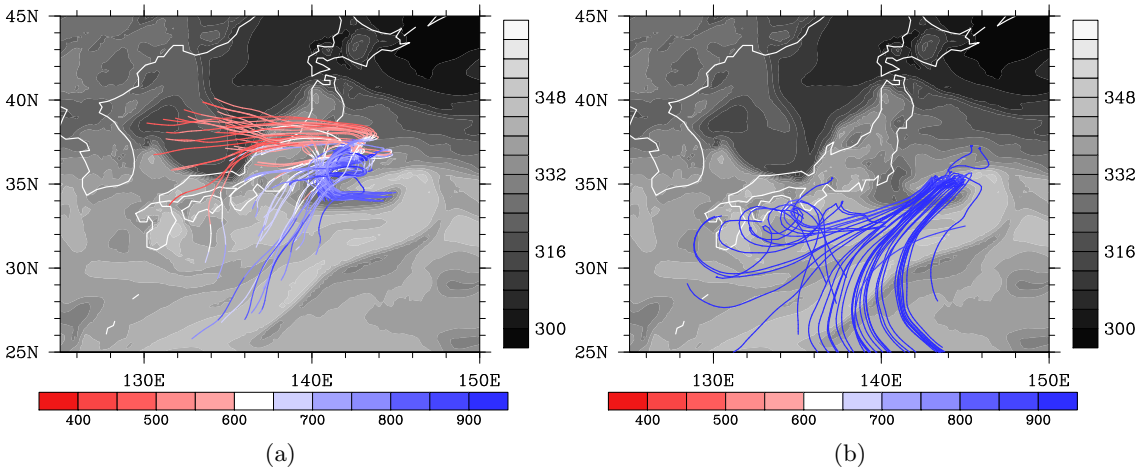

Figure 3.4: (a) and (b): 48 h backward trajectories ending in Sinlaku's environment on 20th September, 06 UTC (details in text) with specific humidity less than 7 $g\ kg^{-1}$ (a) and specific humidity greater than 14 $g\ kg^{-1}$ (b), color along trajectories denotes pressure [hPa] (horizontal color bar), shaded is equivalent potential temperature [K] at 850 hPa on 20 September 06 UTC (vertical color bar).

The majority of parcels meeting these criteria have their origin over Japan to the west-northwest of Sinlaku (Fig. 3.4 (b)). Parcels descend from 400 hPa to 900 hPa during this time period. At the beginning the airparcels have a nearly constant height of 400 hPa and are located in a zonally orientated flow. At 140°E the air parcels suddenly turn southward and descend rapidly to 900 hPa. This descent is probably caused by downward motion to the west of the typhoon along the isentropes of the baroclinic zone. The TC's influence on this sudden southward and downward motion needs to be investigated in

further studies. Between 19 September, 00 UTC and 20 September, 00 UTC, the dry air passes partially the region of the radiosounding in Tateno. As a result, the measurement of the radiosounding in Tateno is expected to represent a part of the dry intrusion. At the starting time on 18 September, 06 UTC, the air parcels along the trajectories show a specific humidity of less than 4 $g\ kg^{-1}$ (not shown). During their descent, the parcels moisten but still have a low specific humidity (4 $g\ kg^{-1} - 7\ g\ kg^{-1}$) on 20 September, 06 UTC, especially in comparison to the surrounding moist tropical air with values of more than 16 $g\ kg^{-1}$. A minority of airparcels originates from lower levels (800 to 900 hPa) to the southeast of Japan. These air parcels are advected first northward into regions of cooler and drier air masses. At about 36°N the airparcels then turn southward and reach the dry intrusion.

A second important question is the origin of trajectories ending in the convective region. To calculate these trajectories an ascent of the air parcels as well as a specific humidity of greater than 14 $g\ kg^{-1}$ at final time is required. In figure 3.4 (a) a marked area of warm moist air exists to the south and east of the cyclone. Trajectories cross this region on their way towards the region of the deep convection. This indicates, assuming constant equivalent potential temperature along the trajectories, that a moist southerly flow along the western side of the subtropical anticyclone advects warm moist air towards the deep convection. Noticeable are furthermore those trajectories which passed the coast of Japan on the first day of the trajectory calculations. Cyclonic trajectories indicate that the parcels following these trajectories already passed the cyclone but did not ascend into the upper-level flow. A comparison with the best track data indicates that the trajectories passed the cyclone between 19 September, 00 UTC and 19 September, 12 UTC. These parcels stayed at low levels and were advected towards the cyclone for a second time on 20 September, 06 UTC, i.e. they passed through the cyclone's circulation twice. It cannot even be excluded, that the air parcels stayed within the cyclone's circulation.

The moist southerly flow near the surface in combination with the dry intrusion above probably leads to a significant destabilization and therefore favors the conditions for a deep convective development. The interaction between the moist southerly flow and the dry air above will be discussed in chapter 6.6. Vertical cross sections show that these moist and warm airparcels from the southerly flow ascend along the baroclinic zone and consequently lead to a moistening of the midtroposphere (not shown). In addition, the ascent along the isentropes of the baroclinic zone leads to a rather extratropical stratiform cloud and precipitation structure as it is seen in the satellite imagery (for example in Fig. 3.3 (b)).

3.2 Quasigeostrophic Forcing

To assess a possible interaction between Sinlaku and either the weak upstream trough to the west (as one would expect in a northwest pattern (Harr and Elsberry, 2000)) or the deep downstream trough to the east, a quasigeostrophic forcing is calculated (Deveson et al., 2002). The advantage of solving and analyzing the quasigeostrophic ω equation is, that positive vertical motion only exists due to positive differential warm air advection

or positive differential vorticity advection increasing with height. This fact simplifies the interpretation of the ω equation enormously. The quasi-geostrophic ω equation is

$$N^2\nabla_h^2\omega + f^2\frac{\partial^2\omega}{\partial z^2} = f\frac{\partial}{\partial z}\left(\vec{v}_g \cdot \nabla\zeta_g\right) - \frac{g}{\Theta_0}\nabla_h^2\left(\vec{v}_g \cdot \nabla\Theta\right) \tag{3.1}$$

where N is the Brunt-Väisälä frequency, ω the vertical velocity, g the gravitational acceleration, f the Coriolis parameter, $\vec{v}_g$ the geostrophic wind, ζ_g the relative vorticity and Θ the temperature, and Θ_0 a reference potential temperature. Due to increased baroclinicity, at lower levels (below 750 hPa) forcing of vertical motion due to temperature advection is the determining factor in this layer. In contrast, differential vorticity advection determines the quasigeostrophic forcing of vertical motion at upper levels (between 650 hPa and 200 hPa).

As a consequence, the quasigeostrophic vertical forcing in these two layers will be described and analyzed separately. At lower levels on 19 September 12 UTC an area of moderate forcing of vertical motion surrounds the decaying TC (Fig. 3.5 (a)). This area shows the typical ET dipole pattern which is characterized by upward motion on the eastern side and downward motion on the western side. The quasigeostrophic forcing of vertical motion reaches values of 0.01 $m\ s^{-1}$ at this time. The dipole pattern is caused mainly by thermal advection on both sides of the cyclone and is typical for the transformation stage during ET (Klein et al., 2000). The reason for the thermal advection in the transformation stage is the interaction of the cyclonic wind field with areas of increased temperature gradients. At upper levels the weak trough to the west only forces weak vertical motion of 0.005 $m\ s^{-1}$ about 18° west of Sinlaku so that an upper level forcing by vorticity advection comparable to that described by Petterssen and Smebye (1971) does not exist at that time (Fig. 3.5 (b)). Hence, a strengthening of Sinlaku by upper level-forcing cannot be expected during the next six hours. Strong positive forcing of vertical motion at upper levels can be seen on the eastern side of the TC and negative forcing on the western side. A reason for this is the interaction of the shear and the vorticity tower of the typhoon. As the westerly winds across the vorticity tower increase with height, the positive advection of vorticity on the eastern side of the typhoon increases with height also. The consequence of this is positive vorticity advection increasing with height. Following the ω equation this leads to ascent. The reverse is true on the western side of Sinlaku. Moreover, strong positive forcing of vertical motion can be seen ahead of the deep trough to the northeast of the TC due to positive vorticity advection, as it is typical for midlatitude systems. This signal is separated clearly from Sinlaku, so that an interaction between this trough and the TC can be ruled out.

The intensity of the trough to the west of Sinlaku does not change significantly, so that it does not provide favorable conditions for a strengthening of the TC during the following six hours to 20 September, 00 UTC. The quasigeostrophic forcing at upper levels in front of this trough is still quite weak and does not influence the intensity of the TC, e.g. by positive differential vorticity advection (not shown). A dipole of quasigeostrophic forcing

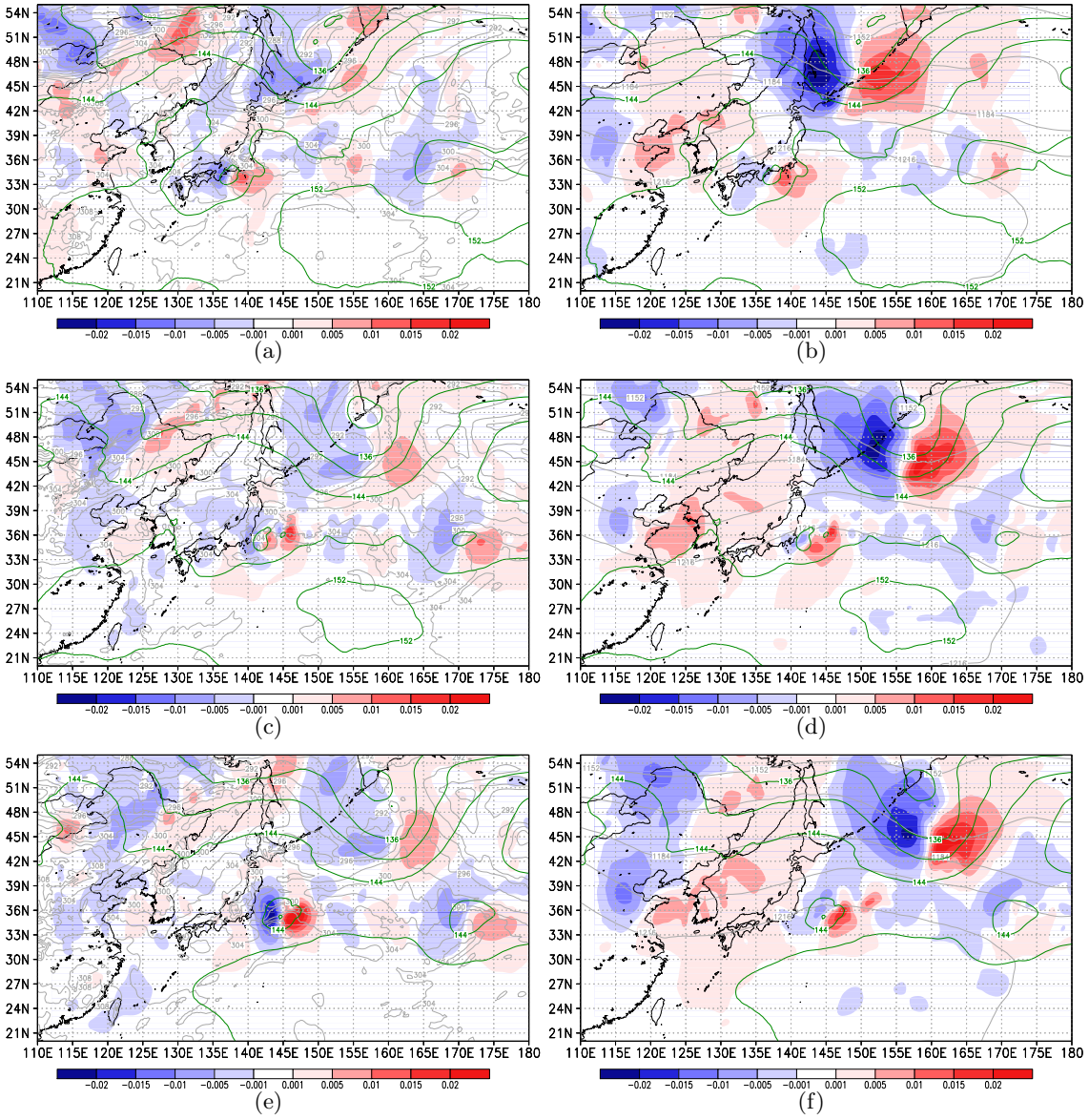

Figure 3.5: Quasigeostrophic forcing of vertical motion [$m\ s^{-1}$] below 750 hPa (a, c, e) and above 650 hPa (b ,d, f) shaded, potential temperature at 900 hPa (K) (grey) (a, c, e), geopotential [gpdm] at 200 hPa (grey) (b, d, f) and geopotential at 850 hPa (green) on 19 September, 12 UTC (top row), 20 September, 00 UTC (middle row) and 20 September, 06 UTC (bottom row).

at upper levels still exists and is, as mentioned above, the result of westerly shear across the cyclone (at this time 23 $m\ s^{-1}$ between 900 hPa and 200 hPa using the convention of the TC community of giving shear between two levels in $m\ s^{-1}$). The TC typical dipole structure at lower levels has almost vanished; quasigeostrophic vertical forcing reaches values of 0.007 $m\ s^{-1}$. The reason for this decreased quasigeostrophic vertical motion might be a reduced temperature advection due to a weaker TC circulation after having interacted with Japan's orography especially on its western side where the northerly flow decreased significantly. A notable feature exists about 3° east to the main circulation at 37°N and 146°E on 20 September 00 UTC (Fig. 3.5 (c, d)). At lower- and upper-levels strong quasigeostrophic forcing of vertical motion can be seen (about 0.015 $m\ s^{-1}$). Comparing this

maximum to the temperature advection in this region, a local maximum of temperature advection can be seen just below this vertical motion pattern (not shown). The reason for the local maximum in temperature advection is an increased temperature gradient in a region of warm frontogenesis which will be described later in this chapter. Moreover, the geopotential at 850 hPa shows a weak negative pressure anomaly in this region. This region with lower pressure induced a second cyclonic circulation and enhanced the wind speed and consequently led to stronger advection. An interesting fact is, that the deep convection developed soon after this time in the same region. Therefore it could be worth a try investigating the influence of this circulation to the east of Sinlaku on the deep convective development. At upper levels a dipole of quasigeostrophic forcing, probably due to vertical shear still surrounds the TC. The shear had increased slightly until that time due to the cyclone's position to the east of a jet entrance region. Upper level forcing can be seen also to the east of the low level pressure anomaly mentioned previously. This low level pressure anomaly is collocated with a local maximum of PV (not shown). As a consequence it can be assumed that the shear of this PV maximum forced quasigeostrophic motion as well. It is important to note with regards to the deep convective development that the upper level forcing is not induced by a midlatitude trough. Regions of upper level forcing ahead of a midlatitude trough are located too far west and northeast of the convective development.

During the following six hours, until 20 September 06 UTC, the quasigeostrophic forcing changes significantly although the synoptic pattern at upper levels does not change very much. Sinlaku moves eastward with an increasing translation speed and is positioned about 5° south of the jetstreak (Fig. 3.2 (g)). The trough to the northeast of the decaying TC is located at 160°E whereas the weak trough to the west remains quasi-stationary along 122°E. However, the low level forcing strengthens considerably and the ET typical dipole pattern can be seen again (Fig. 3.5 (e)). At this time, the quasigeostrophic forcing of ascent reaches more than 0.02 $m\ s^{-1}$. On the western side, values of the same magnitude can be seen for quasigeostrophic forcing of descent. This could be explained by a restrengthening of the TC circulation. In particular, strong southerly winds on the eastern side and the interaction with a baroclinic zone to the northeast of the TC lead to warm frontogenesis. For a more detailed description of this interaction see subsection below. Calculating the average of warm air advection in a box of $2° \times 2°$ east of Sinlaku a maximum of approximately 0.6 $K\ h^{-1}$ can be seen on 20th September 06 UTC (not shown). This value is the second highest mean temperature advection seen during the entire lifecycle of this typhoon. Furthermore, a dipole pattern of cold and warm air advection can be noticed around the cyclone center which is strongly correlated to the quasigeostrophic vertical motion.

At upper levels there is a strong quasigeostrophic vertical upward motion also (Fig. 3.5 (f)). That is probably induced by the vertical interaction with the sheared cyclone. At this time the shear between 900 hPa and 200 hPa is more than 25 $m\ s^{-1}$ (Fig. 3.6). The shear was calculated on two different ways from the ECMWF analysis following Davis et al. (2008). The "non-harmonic" shear was calculated by averaging the wind difference between 200 hPa and 900 hPa in a radius of 600 km around the storm center. By calcu-

lating the shear with this method, the wind field of the storm itself is still included. As the shear of the environment is of main interest the wind field of the storm itself needs to be removed. This has been done with the calculation of the "harmonic" shear. For this calculation the wind calculated from the difference of divergence between 900 hPa and 200 hPa $\vec{v}_\chi$ and the wind calculated from the difference of vorticity between 900 hPa and 200 hPa $\vec{v}_\psi$ are subtracted from the "non-harmonic" shear. The resulting wind field is averaged again in radius of 600 km around the storm center and only represents the environmental flow.

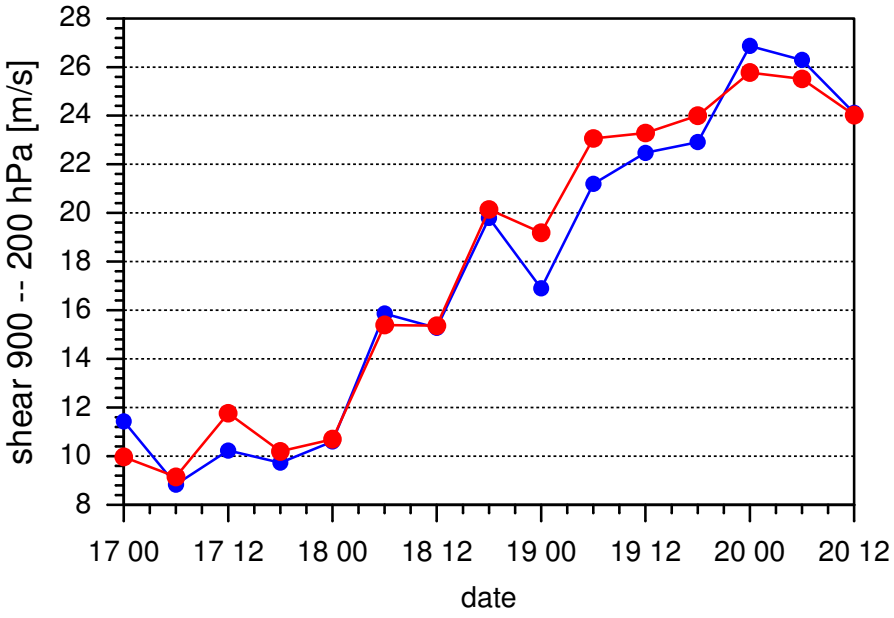

Figure 3.6: Vertical wind shear between 900 hPa and 200 hPa from 17 September 00 UTC to 20 September 12 UTC. Blue line denotes "harmonic" shear, red line "non-harmonic" shear.

As vertical cross sections show, the strong vertical shear leads to a tilt of the vortex and to positive differential vorticity advection increasing with height on its eastern side (not shown).

During the following twelve hours, the quasigeostrophic vertical motion does not change significantly (not shown). The dipole pattern still exists due to continuing warm and cold air advection. Sinlaku itself is now located north of the subtropical anticyclone and below a zonally orientated flow which leads to a strong vertical westerly shear. The weak trough to the west of the TC does not propagate eastward but strengthens slightly and initiates the development of a low pressure system north of the decaying Sinlaku. A further notable feature is the weakening of the jetstreak to the east of the decayed Sinlaku.

3.3 Frontogenesis

To investigate the development of extratropical structures during the transition and compare those to the results of recent studies (e. g. Harr and Elsberry, 2000), the frontogenesis function

$$\vec{F} = F_n\vec{n} + F_s\vec{s} \tag{3.2}$$

$$= -\frac{1}{2}|\nabla_h\Theta|(E\cos 2\beta - \nabla\cdot\vec{v})\vec{n} + \frac{1}{2}|\nabla_h\Theta|(E\sin 2\beta - \vec{k}\cdot\nabla\times\vec{v})\vec{s} \tag{3.3}$$

was calculated (Keyser et al., 1988). In this equation F_n denotes the scalar frontogenesis function and F_s the rotational frontogenesis function. Scalar frontogenesis leads to an increasing temperature gradient as a result of convergence. Rotational frontogenesis instead contributes to a cyclonic rotation of the temperature gradient in the case of an interaction between a cyclonic wind field and a temperature gradient. Therefore, the interaction of positive- and negative rotational frontogenesis amplifies a thermal wave. The unit vector $\vec{n}$ points towards colder air (perpendicular to the isentropes) in a Cartesian coordinate system and the unit vector $\vec{s}$ is tangential to the isentropes, $\vec{v}$ is the horizontal wind vector, E is the resultant of the deformation field $E = (E_{st}^2+E_{sh}^2)^{1/2}$ (E_{st}=stretching, E_{sh}=shearing) and β is the angle between the local orientation of the isentropes and the orientation of the axis of dilatation. On 19 September, 06 UTC, a weak warm scalar frontogenesis can be seen to the north east of Sinlaku with values up to 3 $K\ (h\cdot 100km)^{-1}$ (not shown). The average of the frontogenesis in a box to the northeast of Sinlaku shows very low values of about 0.05 $K\ (h\cdot 100km)^{-1}$ (Fig. 3.7 (d)). The potential temperature at 900 hPa reaches values of about 303 K near the cyclone center, but neither a clear warm core structure nor a strong baroclinic environment can be seen at this time as the temperature field is strongly influenced by Japan's orography. The wind field around the cyclone is nearly symmetric although maximum horizontal winds occur on the southeastern side of the cyclone.
Six hours later, the warm frontogenesis has strengthened considerably and extends more than six degrees to the east of the circulation center with values up to 3 $K\ (h\cdot 100km)^{-1}$ and on average 0.6 $K\ (h\cdot 100km)^{-1}$ (Fig. 3.7 (a, d)). At this time, Sinlaku is only 0.5° to the south of a region with an increased temperature gradient (about 3 $K\ (100km)^{-1}$). However, Sinlaku's warm core is still visible at this time. A rotational frontogenesis can be seen especially along the coast of Japan due to strong windshift to the north of the circulation center probably induced by Japan's orography. On the eastern side of the TC, a strong southerly flow impinges on a weak baroclinic region and converges with an easterly flow north of it. This convergence leads to scalar frontogenesis along the isentropes and therefore to an increasing temperature gradient and a strengthening of the baroclinic zone. Furthermore, it can be assumed that the southerly flow on the eastern side of the decaying TC ascends along the isentropes which leads to the formation of stratiform precipitation to the east and northeast of Sinlaku. The satellite image in figure 3.2 (d) shows this stratiform precipitation region especially to the east of the TC center.

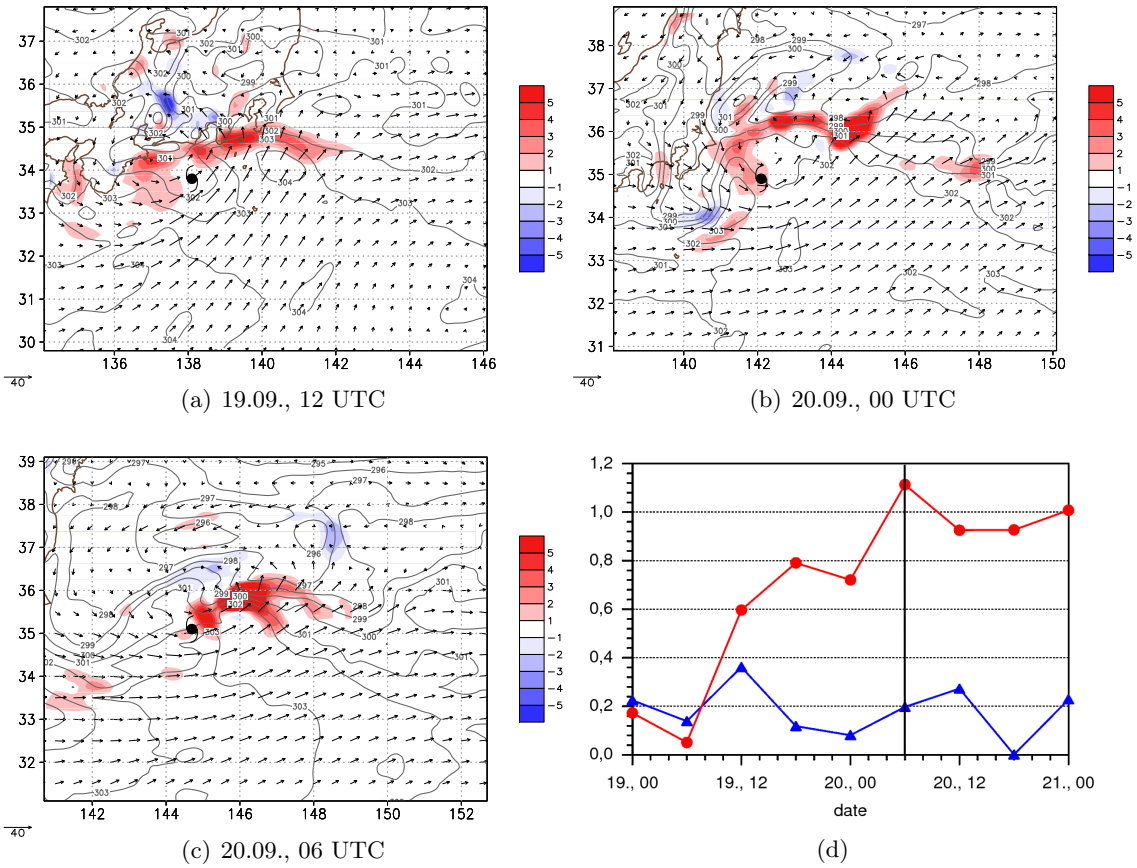

(a) 19.09., 12 UTC (b) 20.09., 00 UTC

(c) 20.09., 06 UTC (d)

Figure 3.7: Frontogenesis at 900 hPa (shaded) $(F_n + F_s)$ at 19 September 12 UTC (a), 20 September 00 UTC (b), and 20 September 06 UTC (c). Gray contours are potential temperature at 900 hPa. Vectors are horizontal wind at 900 hPa. Average frontogenesis $[K\ (100\ km \cdot h)^{-1}]$ (d) defined over a $2° \times 2°$ box to the northeast (NE) (red line) and the southwest (SW) (blue line) of the storm position from 19th September, 00 UTC to 21st September, 00 UTC. Black line denotes time when the deep convection developed and research flights were carried out.

Trajectory calculations indicate the ascent along the isentropes as well (not shown).
By 19 September 18 UTC the cyclone and the temperature gradient northeast of it have move northward and are now located at about 35°N. In contrast to the situation six hours earlier the increased temperature gradient extends farther to the east of the cyclone center. The southerly flow to the east of the cyclone center strengthens a little and wind speeds exceed of 40 $m\ s^{-1}$ at 900 hPa. This stronger southerly flow leads to increased frontogenesis and, as a result, to a temperature gradient of about 4 $K\ (100km)^{-1}$. On average the frontogenesis at this time reaches values of about 0.8 $K\ (h \cdot 100km)^{-1}$ (Fig. 3.7 (d)). Mentionable is also a weaker "second" baroclinic zone along 39°N, 4° north of Sinlaku and north of the baroclinic zone described previously. This baroclinic zone is an extension (occlusion, warm front) of the low pressure system, i.e. the primary midlatitude circulation pattern, to the northeast of Sinlaku. Whereas the temperature gradient close to the TC is zonally orientated at this time, six hours later on 20 September 00 UTC, the baroclinic zone arches as it is typical for midlatitude systems (Fig. 3.7 (c)). A slight cold front had

developed at this time in the south western quadrant of Sinlaku due to an increase of the circulation on the western side of the transforming cyclone and the southward advection of relatively cold air masses. This increased circulation, especially on the western side, can be explained by weaker frictional force of the Japan island. Around this time, the MTSAT IR image shows a broad band of moderate convection which extends to the north and east of the low level circulation center (Fig. 3.3 (b)). This band of convection resembles more the frontal structure of a midlatitude system than a tropical system.
On 20 September 06 UTC the strongest warm frontogenesis during the entire lifecycle of Sinlaku occurs to the northeast of the decaying system. This highest value matches the above mentioned strongest warm air advection at this time. On average the warm frontogenesis reaches values of about 1.1 $K\ (h \cdot 100km)^{-1}$ (Fig. 3.7 (d)). As figure 3.7 (d) shows, warm frontogenesis increased rapidly 30 hours before the assigned time of ET on the 21 September 00 UTC. In cases examined by Harr and Elsberry (2000) the warm frontogenesis increased 12 hours before the assigned ET time. Considering the satellite images during this time period a loss in axisymmetry can be seen, which indicates the warm frontogenesis. As a consequence, taking the frontogenesis as reference for the designation of ET this has occurred between 19 September, 18 UTC and 20 September, 06 UTC. However, the circulation around Sinlaku appears to restrengthen, perhaps due to lower frictional force as Sinlaku had moved away from Japan, so that the circulation was over water. The arching of the baroclinic zone has weakened but is still present. Finally, on 20 September, 12 UTC, the analysis shows that the remnant circulation center of Sinlaku is centered on the baroclinic zone and it seems as if the storm redeveloped a warm core structure with innercore temperatures about 305 K. The distance between the midlatitude low extension and the TC has decreased to 2°. On 21 September 00 UTC Sinlaku is south of a baroclinic zone which shows a temperature gradient of 5 $K\ (200km)^{-1}$. Although Sinlaku still has a quite strong circulation it does not develop a baroclinic wave which might strengthen afterwards. Instead, convective bursts occur on the eastern side of the remnant circulation center (strongest on 20 September, 20 UTC) and move away from the remnant circulation center during their lifecycle. A reason for this separation might be the strong steering flow at upper levels (30 $m\ s^{-1}$ in 200 hPa) in contrast to a weak steering flow below 600 hPa (about 5 $m\ s^{-1}$).

3.4 Vertical motion and moisture

Another important temporal evolution can be seen comparing the lower troposphere vertical motion around Sinlaku at different times. On 18 September 18 UTC the ascent is concentrated to the east of the TC (Fig. 3.8 (a)). Upward motion of more than 2 $Pa\ s^{-1}$ can be seen in a moist southerly flow. The remarkably strong southerly flow to the east of the typhoon originates from the tropics and is most probably linked to the monsoon flow from the South China Sea (Sanabia, 2010). The baroclinic zone at this time is about 5° north of Sinlaku so that the storm is still in a tropical environment. Descent and ascent over Japan is most probably induced by orography. During the following twelve hours Sinlaku's environment changes slightly (Fig. 3.8 (b)). The center of the

storm is still collocated with warm and moist air indicating that the warm core structure still exists. A weak baroclinic zone develops to the east of the cyclone center (south of Japan). This weak baroclinic zone along 34.5°N is collocated with a zonally orientated dipole of vertical motion. Upward motion of 2 $Pa\ s^{-1}$ exists primarily in the warm region and downward motion of 0.5 $Pa\ s^{-1}$ in the cold region. This structure indicates upward motion along the isentropes of this weak baroclinic zone. Moreover, the vertical motion pattern is potentially influenced by Japan's orography. Because of a rather weak temperature gradient and the small meridional extension the region described is not the primary midlatitude baroclinic zone. Instead, it can be assumed that this baroclinic zone is induced by a land-sea temperature gradient. Six hours later again, on 19 September 12 UTC, an interaction between Sinlaku and the baroclinic zone can be seen for the first time. At this time the TC is very close to the coast of Japan (3.8 (c)). The equivalent potential temperature has decreased relative to previous time, especially in the cyclone center. To the west of the cyclone between 33° N and 35° N the equivalent potential temperature is comparatively high with values of more than 350 K. Along 35° N a strong temperature gradient indicates the location of the baroclinic zone. To the south of the baroclinic zone a broad region of upward motion extends from 133° E to 142° E. The western part is collocated with Japan's southern coastline. As a consequence it can be assumed that orography induces vertical motion due to enforced ascent. The eastern part of the vertical motion is collocated with the baroclinic zone. This suggests an ascent of the moist-warm southerly flow along the northward tilted baroclinic zone. During the following hours the ascent along the baroclinic zone becomes more evident.
On 20 September 00 UTC (Fig. 3.8 (e)) Sinlaku's circulation center is not collocated any longer with a warm and moist area. Instead, warm moist air to the south and cold dry air to the north lead to the development of a temperature gradient to the north of the circulation center. The consequence of this is an increasing wind shear and an asymmetry in convection and vertical motion. In comparison to the vertical motion pattern 24 hours before it is not collocated with the cyclone center any longer but extends eastward to 150°E. The zonally orientated dipole pattern in vertical motion is stronger than before. Upward motion exceeds values of 4 $Pa\ s^{-1}$ and downward motion 2 $Pa\ s^{-1}$.

As the dipole pattern is nearly parallel to the isentropes of the baroclinic zone it can be assumed the vertical motion pattern is the result of the interaction between Sinlaku and the baroclinic zone. Furthermore, the dipole pattern indicates a secondary circulation along the baroclinic zone with upward motion to the south of it and downward motion to the north. Noticeable is the upward motion along 140°E extending to the south of the baroclinic zone. This ascent is collocated with a warm moist southerly flow. This suggests that the moist southerly flow enhances instability and therefore favors the conditions for upward motion, respectively convection. To the northeast of the cyclone center dry air begins wrapping around the cyclone center to the south. The developing dry intrusion is the precursor of that, seen six hours later to the south of the circulation center. The development of the dry slot coincides with the dry trajectories which suddenly turned southward (Fig. 3.4 (a)). As the dry intrusion is very close to the cyclone it can be assumed that the wind field of the cyclone induced its development.

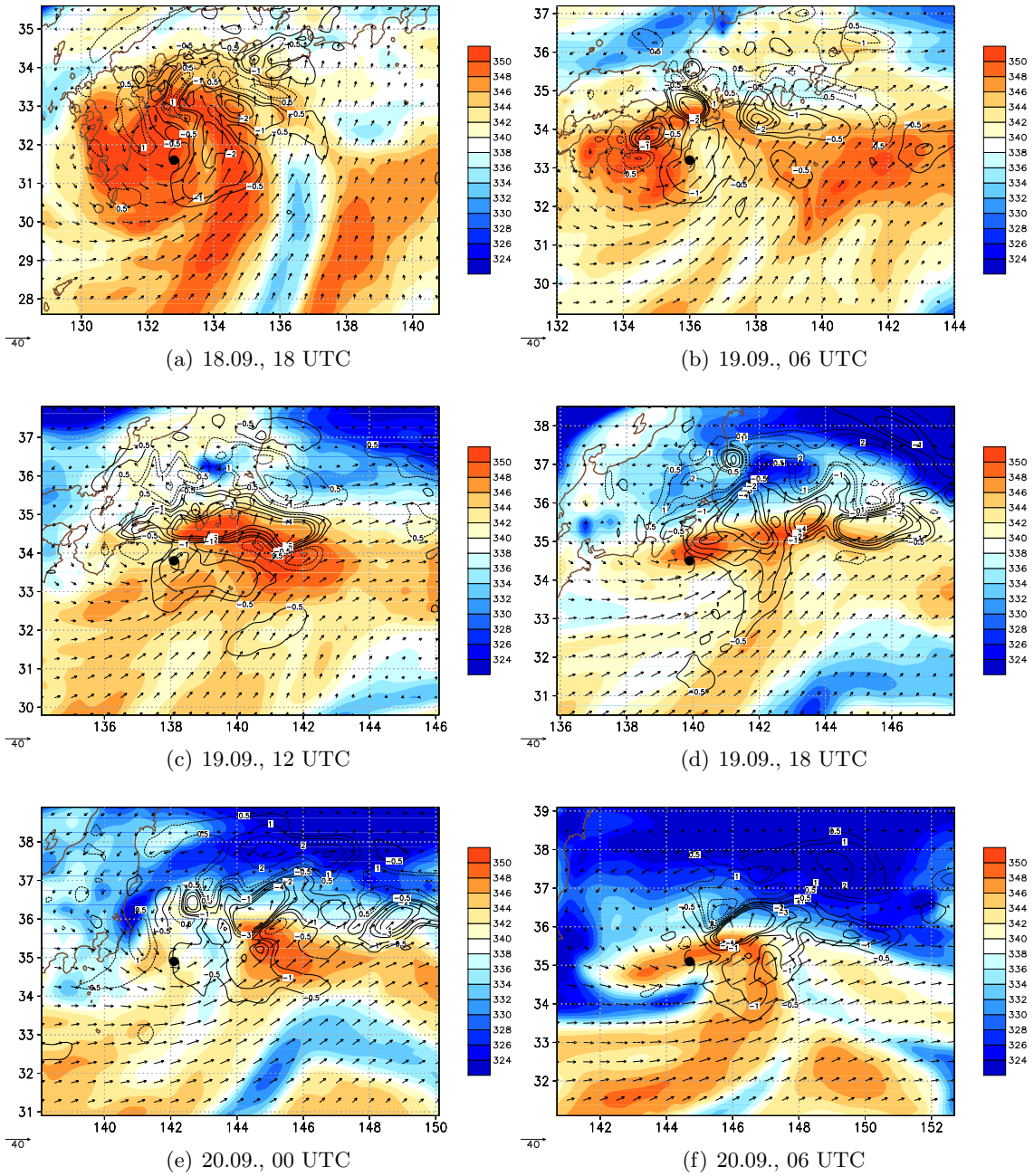

(a) 18.09., 18 UTC (b) 19.09., 06 UTC

(c) 19.09., 12 UTC (d) 19.09., 18 UTC

(e) 20.09., 00 UTC (f) 20.09., 06 UTC

Figure 3.8: Equivalent potential temperature (shaded) at 700 hPa from 18th September, 18 UTC to 20th September, 06 UTC. Omega $[Pa\ s^{-1}]$ in black contours. Ascent is labeled negative (solid contours), descent is labeled positive (dashed contours). Vectors are horizontal wind $[m\ s^{-1}]$ at 700 hPa. Black cyclone symbol marks Sinlaku's best track position.

Six hours later on 20 September 06 UTC (the time when the deep convection had developed and the research flights were accomplished), the dry air is located to the south of the cyclone (Fig. 3.8 (f)). The circulation center of Sinlaku is located directly at the baroclinic zone. The ascending region is still zonally orientated along the baroclinic zone. The upward motion reaches a maximum of more than 4 $Pa\ s^{-1}$ about 1° E to the cyclone center. This maximum of vertical motion suggests that the ECMWF represents the deep convection seen in the satellite image at this time at least partially. The maximum of vertical motion

is collocated again with an area of high equivalent potential temperature. This indicates once again the low level instability as a consequence of the southwesterly flow advecting moist and warm air. Downward motion to the north of the baroclinic zone strengthens once again the idea of a secondary circulation in this region. A detailed view of the structure at that time will be performed later in this study with the help of observational data from dropsondes, satellites and ELDORA.

4. Principles of Radar meteorology and ELDORA

4.1 Radar meteorology

The basic principle of a weather radar is the back scattering of electromagnetic radiation at atmospheric scattering objects. The characteristics of the backscattered radiation (i. e. amplitude, frequency and polarization) give information about various characteristics of the scattering objects (number density, velocity and aggregate state). From this information one can obtain insights into the precipitation-rate and type of precipitation. The weather radar primarily consists of an antenna that transmits radiation with wavelengths from 1 cm to 10 cm. On its way through the atmosphere the transmitted signal is scattered at and attenuated by raindrops, hail and other precipitation objects. These objects reflect the radiation in all directions. As a consequence, only a small part is reflected back towards the radar where a receiver decodes this signal. The intensity of the back scattered signal (radar reflectivity) tells us something about the size and the form of the precipitation. The location of the object can be determined from the signals runtime and the orientation of the antenna itself. An important aspect of Doppler Radar Systems is the opportunity to measure the radial velocity of the scattering objects. This quantity can be derived from the frequency shift (phase) between the transmitted and the received signal.

The unit of the received signal, the radar reflectivity, is given in dBZ and the reflectivity is proportional to the energy which is scattered back by all the scattering objects in the scanned volume. The magnitude of the radar reflectivity is determined by the distance between radar and scatter object r, the wavelength λ and the transmitted energy. The relation between the transmitted power P_t and the received power P_r is given by the radar equation (Sauvageot, 1992):

$$P_r = \frac{P_t G^2 \lambda^2 L^2 c\tau\eta}{128\pi^3 r^2} \int_\Omega f^4(\Theta, \Phi) d\Omega \tag{4.1}$$

L is the attenuation, c the light velocity, τ the pulse length, η the reflectivity, G the antenna gain (degree of efficiency), Θ the azimuthal angle, Φ the elevation angle and Ω the solid angle. Assuming the Rayleigh approximation for small particles the reflectivity itself is given by

$$\eta = \frac{\pi^5}{\lambda^4}|K^2| \int_0^\infty D^6 n(D) dD = \frac{\pi^5}{\lambda^4}|K^2|Z \tag{4.2}$$

introducing the radar reflectivity factor $Z = \int_0^\infty D^6 n(D) dD$ and the number density distribution $n(D)$. The unit of Z is $mm^6 m^{-3}$, respectively $Z(dBZ) = 10log[Z(mm^6 m^{-3})]$. Typical values are $30dBZ$ for moderate rain and $60dBZ$ for hail. In equation 4.2 D is the diameter of the scatter objects and K the dielectricity factor which depends on the dielectric coefficient.

4.2 The Electra Doppler Radar ELDORA

ELDORA is an airborne, dual beam meteorological research radar that was developed conjointly at the National Center for Atmospheric research (NCAR) in Boulder and the Centre de Recherche en Physique de l'Environnement Terrestre et Planetaire (CRPE) in Paris (Hildebrand et al., 1994). ELDORA was designed to measure the air motion and rainfall characteristics of very large storms which are too large or too remote to be adequately observed by ground-based radars (Hildebrand et al., 1994). Additionally, in comparison to a ground-based radar, observations can be made with this airborne radar from an optimal vantage point because of the ability to fly the radar quickly to the storm. This ability minimizes the deleterious effects of attenuation as the data can now be taken at a close range to the system. From equation 4.1 the received power is proportional to the second power of the distance between radar and scatter object r. Therefore it is desirable to minimize this distance. During T-PARC 2008, ELDORA was mounted on

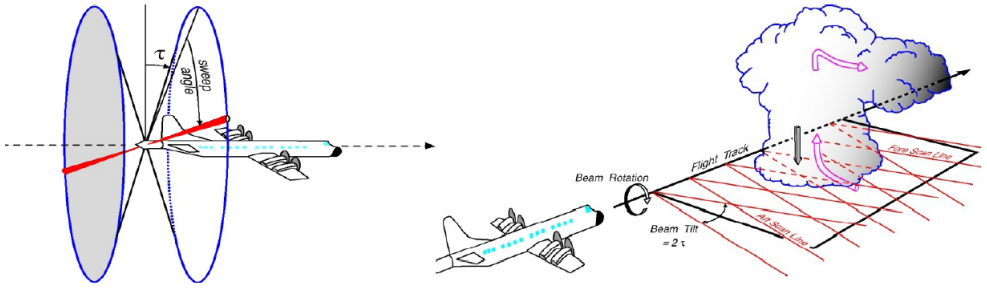

Figure 4.1: Scan technique of the airborne Electra Doppler Radar ELDORA (from Hildebrand et al., 1994).

board the Naval Research Lab (NRL) P3. The two Doppler antennas extend back from the tail of the aircraft and rotate about the longitudinal axis of the aircraft. One antenna points 15° to 19° forward of a plane normal to the flight pa the aircraft and one points aft

with the same angle. When translating through space the radar traces two conical helices through the atmosphere (see Fig. 4.1). This scan pattern facilitates the collection of dual fore- and aft-pointing Doppler velocity while the NRL-P3 flies in a straight line past or through storms. The results of a flight are two separate looks within about $50 - 100\ km$ at a resolution of 300 m. These two looks contain two wind vectors at each observation point. The wind vectors can later be used to derivate a three dimensional wind field.
As the research flight speed of the NRL-P3 is approximately 130 $m\ s^{-1}$ the scientific requirement for samples of $300 - 500\ m$ resolution dictates an antenna rotation rate of 16-26 RPM (96-156° s^{-1}). Furthermore the resolution dictates one integration period being completed every degree of rotation. As a result, the integration periods are in the order of $6 - 10\ ms$. The observed structures have a time to independence of $3 - 7\ ms$. Therefore, only one to three independent samples can be taken in one integration period. Because of a desired velocity accuracy of 1 $m\ s^{-1}$ about 10 independent samples are to be made. As a consequence, a complex waveform is chosen: this so called stepped chirp waveform consists of a pulse of energy, within which are "chips" (sub-pulses) which are coded. In ELDORA these "chips" can be distinguished by discrete shifts in the transmit frequency. They can then be decoded by the receiver and processed individually. The rate of the chips can be adapted to the weather conditions of each mission. In the case of clear air observations in the planetary boundary layer, for example, longer pulses and constant pulse repetition times (PRT) are chosen to achieve a higher sensitivity. In convective, turbulent storms the pulses are a lot shorter and the PRTs are selected to be in a ratio of 4 to 5. Due to the limited antenna aperture size of an airborne Doppler radar (in this case about 1.4 m) and the use of a wavelength $\geq 3\ cm$ and $\leq 5\ cm$ the ELDORA antenna provides beam width $\Phi \approx 1.27\lambda/D$ of 1.8° and 2.8°. In this equation D is the diameter of the antenna and λ the transmitted wavelength. The limited range of wavelength is a compromise between the best possible angular resolution, which is better at lower wavelengths, and atmospheric attenuation which is larger at higher wavelengths. In conclusion, an X-band transmitter (wavelength $\geq 3.2\ cm$ (9.3 GHz)) is used with a peak power of 50 kW. The ELDORA output variables include radar reflectivity, mean radial velocity, spectral width and normalized coherent power (NCP).
Due to a problem with one receiver of the ELDORA system during T-PARC 2008, the radar rotation was slowed down to 78° per second instead of 144° per second. Hence, the integration period increased to 18 ms, but features of 2 km and greater were still well resolved.

4.3 Quality control of ELDORA raw-data

As the Doppler velocity contains meteorological signals and aircraft motion the latter needs to be removed from the Doppler velocities in a first step. In this case the data were already corrected by the Earth Observing Laboratory (EOL) with the Testud-Hildebrand-Lee methodology (Testud et al.,1995). This methodology makes the assumption that the ground echo return should be flat and have no residual velocity. As described in Testud et al. (1995), solving a system of equations computes the correction to the inertial

navigation system (INS) parameters. Recently several tests have been made on real-time dissemination of wind fields determined from airborne Doppler radar data and on the corresponding automatic quality control (Gamache et al., 2008; Wolff et al., 2009).
Wolff et al. for example developed a technique which removes a lot of the undesirable echoes automatically by assigning a probability of weather to the data. The quality control of radar data is necessary to remove non-weather echoes such as second trip echoes, sidelobes, rings, low signal to noise returns, speckles and ground clutter. Second trip echoes occur when a pulse reflected from a distant scattering object arrives at the radar after the radar has emitted the next pulse. The result of the second trip echoes are wrong locations of the scattering objects. Ground clutter is caused either by rough seas or by low-level inversions. These inversions refract the low elevation beams toward ground, so that the ground surface reflects the signal and therefore pretends having precipitation. Sidelobes are caused by the antenna configuration it self. In addition to the main lobe the transmitted pulse consists several side lobes, which surround the main lobe. These sidelobes can detect strong scattering objects close to the radar or even the earth's surface. As a consequence scattering objects are detected which are not in the direction of the main lobe, so that the positioning of scattering objects is wrong. In particular in stratiform precipitation areas rings can be detected. These rings are caused by a bright band which is typical for stratiform precipitation. The bright band results from higher reflectivity in the melting layer of stratiform clouds as melting snow flakes occur as large raindrops to the radar. As the beams at different elevation angles cut the bright band in a different distance to the radar, rings of higher reflectivity occur for each elevation angle. Cutting through the radar data at constant height multiple rings can be seen, each for one elevation.

In this study, a method was chosen which operates on using different thresholds typo. To obtain a first quick look at the data and work on them the software SOLOII was used. At first the normalized coherent power field was used to remove noise. NCP is defined as the ratio of the power calculated at leg one to the total received power. That means that the lower the NCP value the higher the probability that a given radar return is noise and vice versa. Using NCP thresholds is very efficient at removing noise. In this case all data with a NCP threshold below 0.3 were deleted. With this threshold most of the clear air speckles and a large part of second trip echoes can be removed. It should be mentioned that this threshold may also cause some "good" data removed misleadingly. Furthermore all data in a ring with a radius of 0.0 to 0.5 km and a radius of 70.0 to 75.0 km around the airplane were removed to avoid "bad" data due to turbulence near the airplane or strong attenuation.
In a second step the spectral width, which is a measure of the velocity dispersion within one pulse volume, was used to define non-weather data. The spectral width is determined by wind shear, turbulence and antenna rotation. All data with a spectral width bigger than 4.0 **and** a reflectivity below 5.0 were removed. A large amount of "bad data" except for sidelobes were deleted with this method.

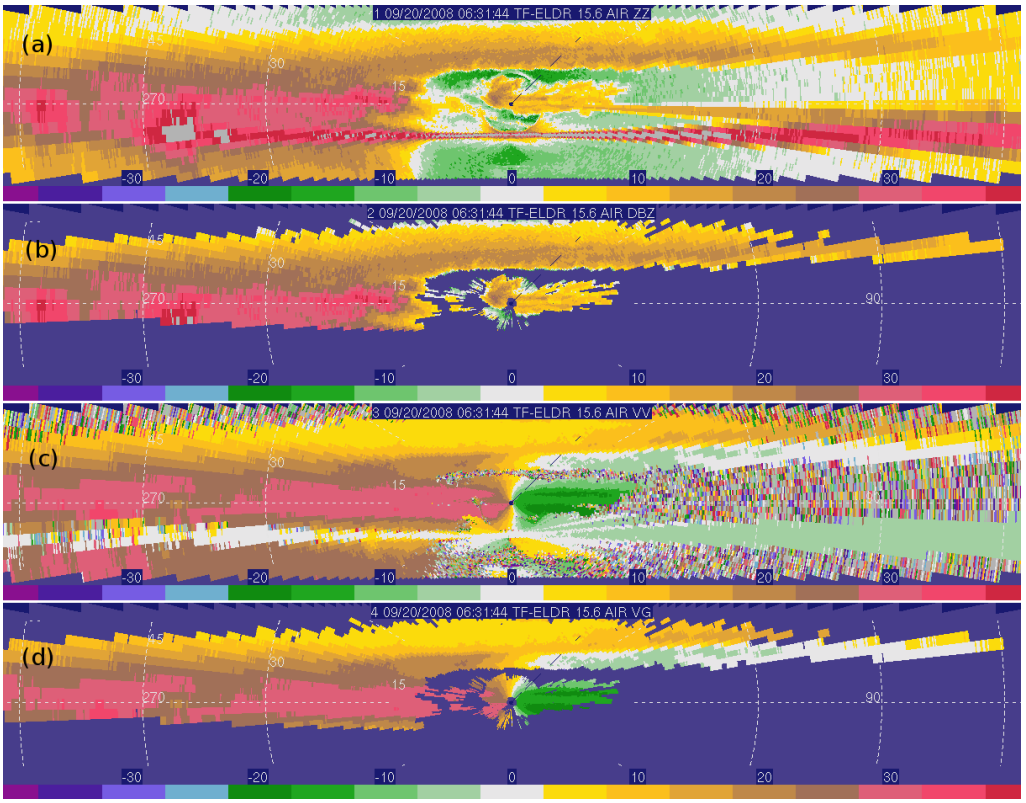

Figure 4.2: Raw reflectivity (a) and raw radial velocity (c) and from the ELDORA front radar at 20.09.2008, 06:31:44 UTC. Reflectivity (b) and radial velocity (d) after final quality control.

In a third step the dataset was "despeckled". Speckles are isolated gates outside the main echo. In this case a speckle consisted of seven measured gates (about 1 km). Accordingly, isolated data shorter than seven gates were deleted. Finally, the surface was removed by a routine included in SOLOII. In the case of a flat surface this routine determines the gates that intersect the ground by using the altitude of the aircraft, the effective beamwidth, the ray number and simple trigonometric functions.

Indeed, there are still some effects that make it difficult to find the ground location. As the propagation of the beam is a function of the atmospheric conditions, the long-range beams in particular are often refracted by the stratification of the atmosphere. This causes a ground contamination before the first calculated gate. Contamination is also caused by the already mentioned "chips". It is not possible to discriminate between the different frequencies which causes ground contamination slightly higher than the surface (Bell, 2011, personal communication). Another aspect is the manipulation of the radial velocity due to the motion of the surface as it appears in tropical cyclones over ocean. These data could not be identified and removed automatically. As a result, the dataset (850 files) was edited manually in a final quality control.

A comparison between the data before and after the quality control can be seen in figure 4.2. This comparison shows the efficient removal of ground clutter. Furthermore, a lot of speckles which can be nicely seen in (Fig. 4.2(c)) have been removed by the automatic quality control. Close to the radar and near the ground weak sidelobes can be identified

in (Fig. 4.2(c)). By editing the data manually these erroneous data were removed as well (Fig. 4.2(d)). Another notable feature is a beam with higher reflectivity to the right of the radar (Fig. 4.2(a)). This beam is caused by ground clutter due to a stable stratification and thus refraction of the radar beam towards the ground. The quality control removed this non-weather echo automatically.

5. The SAMURAI analysis technique

The **S**pline **A**nalysis at **M**esoscale **U**tilizing **R**adar and **A**ircraft **I**nstrumentation (SAMURAI) has recently been developed by Michael Bell at the National Center for Atmospheric Research (NCAR) in Boulder (Colorado) and the Naval Postgraduate School (NPS) in Monterey (California). At first this data assimilation system was applied to aircraft measurements of a TC in order to deduce the most probable antis symmetric TC state for momentum and energy budget calculations (Bell, 2010). The overall-goal was to develop a software program that can use aircraft data, satellite winds and model data as a background field to calculate the most probable state of the atmosphere by minimizing a cost function. Until now a 3D-VAR assimilation has been implemented so that the SAMURAI software can be extended into asymmetric cylindrical and Cartesian coordinates in order to initialize numerical models for example. In addition to the VAR technique, a weak mass continuity constraint is used. This is an important contrast to radar analysis tools developed previously, which only used a strong mass continuity constraint that satisfied the mass continuity equation exactly, e.g. Mohr et al., 1986. A radar analysis tool using only a weak mass continuity constraint was first presented by Gamache, 1997. Since the 3D-VAR data assimilation is a very important component of this software tool the theoretical background is described below. The variational (VAR) technique is derived from Bayesian first principles to determine the maximum likelihood estimate of the atmospheric structure and will be described in the following section. The derivation of the maximum likelihood estimate follows closely Vandenberghe (1999), Kalnay (2003) and Bell (2010).

5.1 Derivation of maximum likelihood estimate

As for data assimilation for numerical weather prediction itself, the derivation of a three dimensional state of the atmosphere from aircraft instrumentation is an initial-value problem, for which there are more unknown quantities than observations. As a result in the case of a variational approach an under-determined system of equations has to be solved. To improve the probability of getting the true state of the atmosphere

prior information (i.e. forecast or analysis of any numerical weather prediction system) is needed as a background/first guess representing the best available estimate just before the analysis time. In order to combine the n observations $s_1, s_2, s_3, ..., s_n$ and the prior information $b_1, b_2, b_3, ..., b_n$ optimally to get the true state s, statistical information about the errors in the observations and the background is needed. One can assume that the errors of the measurements are uncorrelated, normally distributed with standard deviations $\sigma_1, \sigma_2, \sigma_3, ..., \sigma_n$. The errors of the background have the same properties with the standard deviations $\mu_1, \mu_2, \mu_3, ..., \mu_n$. With this assumption the likelihood of the true state s, given the observation s_1 with the standard deviation σ_1, is:

$$p_{\sigma_1}(s_1|s) = \frac{1}{\sqrt{2\pi}\sigma_1} \exp\left(-\frac{(s_1 - s)^2}{2\sigma_1^2}\right) \tag{5.1}$$

and for the prior information b_1 with the standard deviation μ_1

$$p_{b_1,\mu_1}(s) = \frac{1}{\sqrt{2\pi}\mu_1} \exp\left(-\frac{(b_1 - s)^2}{2\mu_1^2}\right) \tag{5.2}$$

The Bayes' theorem for the a posteriori probability of state s given observation s_1 and the a priori information b_1 is

$$p_{\sigma_1}(s|s_1) = \frac{p_{\sigma_1}(s_1|s)p_{b_1,\mu_1}(s)}{p_{\sigma_1}(s_1)} = \frac{\frac{1}{\sqrt{2\pi}\sigma_1} \exp\left(-\frac{(s_1-s)^2}{2\sigma_1^2}\right) \frac{1}{\sqrt{2\mu_1}\sigma_1} \exp\left(-\frac{(b_1-s)^2}{2\mu_1^2}\right)}{p_{\sigma_1}(s_1)} \tag{5.3}$$

where the denominator is

$$p_{\sigma_1}(s_1) = \int_s \frac{1}{\sqrt{2\pi}\sigma_1} \exp\left(-\frac{(s_1 - s)^2}{2\sigma_1^2}\right) ds \tag{5.4}$$

By maximizing the numerator of 5.3 one can obtain the estimate of the truth.

As the three equations above are only for one dimensional problems a generalization for vectors of observations and background fields is needed. The standard formulation of variational methods was first derived in by Lorenc (1986) and is based on the minimization of a cost function. A similar approach was used in the SAMURAI analysis tool. The generalization mentioned above has to contain a field of desired and needed variables $\mathbf{x}_a$, a background field $\mathbf{x}_b$ and a set of observations $\mathbf{y}_o$. The most probable state (analysis) of the atmosphere is than described by the vector $\mathbf{x}_t$ which is discretized at model points. Vector $\mathbf{x}_t$ is given by $\mathbf{x}_t = \mathbf{x}_b + \mathbf{W}[\mathbf{y_0} - H(\mathbf{x}_b)] - \epsilon_a = \mathbf{W}\mathbf{d} - \epsilon_a$ where $\mathbf{d}$ is the observational increment, ϵ_a the error of the analysis, and H is the forward observational operator which maps from the background field to the observational field. For some variables which

are derived from indirect measurements H can be nonlinear. W is the optimal weight matrix which will be determined from statistical interpolation. The optimal weight matrix itself is given by the background error covariance matrix in the observation space (see below) multiplied by the inverse of the sum of the background and the observation error covariances. It is defined as

$$\mathbf{W} = \mathbf{B}\mathbf{H}^T(\mathbf{H}\mathbf{B}\mathbf{H}^T + \mathbf{R})^{-1} \tag{5.5}$$

and minimizes the analysis error covariance.
As in the one dimensional problem the statistical assumptions that the background and the observation are again unbiased and the probability distribution is Gaussian about the background field are made. Furthermore, it is a reasonable assumption that the observations and background errors are uncorrelated. The background error and the analysis error are defined as vectors

$$\epsilon_b(x,y) = \mathbf{x}_b(x,y) - \mathbf{x}_t(x,y) \tag{5.6}$$
$$\epsilon_a(x,y) = \mathbf{x}_a(x,y) - \mathbf{x}_t(x,y) \tag{5.7}$$

and the observational errors as

$$\epsilon_o = \mathbf{y}_o(\mathbf{r}_i) - H[\mathbf{x}_t(\mathbf{r}_i)] \tag{5.8}$$

where $\mathbf{y}_o(\mathbf{r}_i)$ are the observations available at irregular spaced points $\mathbf{r}_i$. As a result the covariance matrices for the analysis, background and observations are:

$$\mathbf{P}_a = \mathbf{A} = \epsilon_a\epsilon_a^T \tag{5.9}$$
$$\mathbf{P}_b = \mathbf{B} = \epsilon_b\epsilon_b^T \tag{5.10}$$
$$\mathbf{P}_o = \mathbf{R} = \epsilon_o\epsilon_o^T \tag{5.11}$$

As the determinant of the covariance matrix for the background error is equivalent to the standard deviation in the one dimensional approach, equation 5.2 can be written as

$$p_{\mathbf{B}}(\mathbf{x}) = \frac{1}{(2\pi)^{n/2}|\mathbf{B}|^{1/2}} \exp\left[-\frac{1}{2}(\mathbf{x}_b - \mathbf{x}_t)^T\mathbf{B}^{-1}(\mathbf{x}_b - \mathbf{x}_t)\right]. \tag{5.12}$$

In equation 5.12 n is the product of the number of points times the number of variables. Similarly, the probability density of the observation vector 5.1 can be written now as

$$p_{\mathbf{R}}(\mathbf{y}_0|\mathbf{x}) = \frac{1}{(2\pi)^{p/2}|\mathbf{R}|^{1/2}} \exp\left[-\frac{1}{2}(\mathbf{y}_0 - H(\mathbf{x}_t))^T\mathbf{R}^{-1}(\mathbf{y}_0 - H(\mathbf{x}_t))\right] \tag{5.13}$$

where p is the number of observations. The posterior probability of the true state can then be derived by applying Bayes' Rule. Substituting 5.12 and 5.13 into Bayes' rule

$$p(\mathbf{x}_t|\mathbf{y}_0) = \frac{p_{\mathbf{R}}(\mathbf{y}_0|\mathbf{x})p_{\mathbf{B}}(\mathbf{x})}{p(\mathbf{y}_0)} \tag{5.14}$$

yields

$$\begin{aligned} p(\mathbf{x}_t|\mathbf{y}_0) \quad &= \tfrac{1}{p(\mathbf{y}_0)} \cdot \tfrac{1}{(2\pi)^{n/2}|\mathbf{B}|^{1/2}} \exp\left[-\tfrac{1}{2}(\mathbf{x}_t - \mathbf{x}_b)^T\mathbf{B}^{-1}(\mathbf{x}_t - \mathbf{x}_b)\right] \\ &\cdot \tfrac{1}{(2\pi)^{p/2}|\mathbf{R}|^{1/2}} \exp\left[(-\tfrac{1}{2}(\mathbf{y}_0 - H(\mathbf{x}_t))^T\mathbf{R}^{-1}(\mathbf{y}_0 - H(\mathbf{x}_t))\right] \end{aligned} \tag{5.15}$$

Dropping the constants:

$$\begin{aligned} p(\mathbf{x}_t|\mathbf{y}_0) &\propto \frac{1}{p(\mathbf{y}_0)} \cdot \exp\left[-\frac{1}{2}(\mathbf{x}_t - \mathbf{x}_b)^T\mathbf{B}^{-1}(\mathbf{x}_t - \mathbf{x}_b)\right. \\ &\quad \left.-\frac{1}{2}(\mathbf{y}_0 - H(\mathbf{x}_t))^T\mathbf{R}^{-1}(\mathbf{y}_0 - H(\mathbf{x}_t))\right] \\ &\propto \frac{1}{p(\mathbf{y}_0)} \cdot \exp\left[-\mathbf{J}\right] \end{aligned} \tag{5.16}$$

In this expression the vector $\mathbf{y}_0$ is measured and known. Finally we take the natural logarithm of both sides of 5.16 and get

$$ln(p(\mathbf{x}_t|\mathbf{y}_0)) = ln(\frac{1}{p(\mathbf{y}_0)}) \cdot \left[-\frac{1}{2}(\mathbf{x}_t - \mathbf{x}_b)^T\mathbf{B}^{-1}(\mathbf{x}_t - \mathbf{x}_b) - \frac{1}{2}(\mathbf{y}_0 - H(\mathbf{x}_t))^T\mathbf{R}^{-1}(\mathbf{y}_0 - H(\mathbf{x}_t))\right] \tag{5.17}$$

As equation 5.17 shows, the maximum of the a posteriori probability is attained when the variable term on the right hand side of this equation is at a minimum. Defining this term as the cost function $J(\mathbf{x})$ the maximum a posteriori probability is achieved when

$$\begin{aligned} min\{J(\mathbf{x})\} &= min\{J_b(\mathbf{x}) + J_o(\mathbf{x})\} \\ &= min\left\{-\frac{1}{2}(\mathbf{x}_t - \mathbf{x}_b)^T\mathbf{B}^{-1}(\mathbf{x}_t - \mathbf{x}_b)\right. \\ &\left.-\frac{1}{2}(\mathbf{y}_0 - H(\mathbf{x}_t))^T\mathbf{R}^{-1}(\mathbf{y}_0 - H(\mathbf{x}_t))\right\} \end{aligned} \tag{5.18}$$

Actually in equation 5.18 one term is still missing. A lot of grid-point based applications have an additional term in the cost function for the mass continuity. This term can simply be included by adding a third cost function $J_c(\mathbf{x})$ to equation 5.18. In the SAMURAI technique this third cost function is avoided by using cubic B-splines. The use of cubic B-splines (also known as the Galerkin approach) distinguishes the SAMURAI analysis technique from other variational approaches. These cubic B-splines are described separately at the end of this section.
The minimum of $J(\mathbf{x})$ is attained when

$$\nabla J(\mathbf{x}_t) = 0 \tag{5.19}$$

Assuming that the analysis is a close approximation to the truth and therefore to the observations one can obtain an exact solution for the underdetermined system. For this solution H needs to be linearized and the second term of equation 5.18 can be written as

$$\mathbf{y}_0 - H(\mathbf{x}_t) = \mathbf{y}_0 - H[\mathbf{x}_b + (\mathbf{x}_t - \mathbf{x}_b)] = \{\mathbf{y}_0 - H(\mathbf{x}_b)\} - \mathbf{H}(\mathbf{x}_t - \mathbf{x}_b) \tag{5.20}$$

$\mathbf{H}$ is in this equation the tangent linear approximation of the non linear observation operator H. The $\mathbf{H}$ matrix maps and transforms the vectors in model space into their corresponding values in observation space. $\mathbf{H}$ is a $p \times n$ matrix with the elements $h_{i,j} = \partial H_i/\partial x_j$. Combining equation 5.20 and the equation for $J(\mathbf{x})$ leads to

$$\begin{aligned} J(\mathbf{x}) &= \frac{1}{2}(\mathbf{x}_t - \mathbf{x}_b)^T\mathbf{B}^{-1}(\mathbf{x}_t - \mathbf{x}_b) \\ &+ \frac{1}{2}[\{\mathbf{y}_0 - H(\mathbf{x}_b)\} - \mathbf{H}(\mathbf{x}_t - \mathbf{x}_b)]^T\mathbf{R}^{-1}[\{\mathbf{y}_0 - H(\mathbf{x}_b)\} - \mathbf{H}(\mathbf{x}_t - \mathbf{x}_b)] \\ &= \frac{1}{2}(\mathbf{x}_t - \mathbf{x}_b)^T\mathbf{B}^{-1}(\mathbf{x}_t - \mathbf{x}_b) + \frac{1}{2}(\mathbf{x}_t - \mathbf{x}_b)^T\mathbf{H}^T\mathbf{R}^{-1}\mathbf{H}(\mathbf{x}_t - \mathbf{x}_b) \\ &- \frac{1}{2}\{\mathbf{y}_0 - H(\mathbf{x}_b)\}^T\mathbf{R}^{-1}\mathbf{H}(\mathbf{x}_t - \mathbf{x}_b) - \frac{1}{2}(\mathbf{x}_t - \mathbf{x}_b)^T\mathbf{H}^T\mathbf{R}^{-1}\{\mathbf{y}_0 - H(\mathbf{x}_b)\} \\ &+ \frac{1}{2}\{\mathbf{y}_0 - H(\mathbf{x}_b)\}^T\mathbf{R}^{-1}\{\mathbf{y}_0 - H(\mathbf{x}_b)\} \end{aligned} \tag{5.21}$$

This cost function is a quadratic function of the increment $(\mathbf{x}_t - \mathbf{x}_b)$ of the form $F(\mathbf{x}_t - \mathbf{x}_b) = 1/2(\mathbf{x}_t - \mathbf{x}_b)^T \mathbf{A}(\mathbf{x}_t - \mathbf{x}_b) + \mathbf{d}^T(\mathbf{x}_t - \mathbf{x}_b) + c$. $\mathbf{A}$ is a symmetric matrix, $\mathbf{d}$ is a vector and c a scalar. The gradient of this scalar function can be written as $\nabla F(\mathbf{x}_t - \mathbf{x}_b) = \mathbf{A}(\mathbf{x}_t - \mathbf{x}_b) + \mathbf{d}$ using the following properties: $\nabla(\mathbf{d}^T(\mathbf{x}_t - \mathbf{x}_b)) = \nabla((\mathbf{x}_t - \mathbf{x}_b)^T \mathbf{d}) = \mathbf{d}$ and $\nabla((\mathbf{x}_t - \mathbf{x}_b)^T \mathbf{A}(\mathbf{x}_t - \mathbf{x}_b)) = 2\mathbf{A}(\mathbf{x}_t - \mathbf{x}_b)$ With these properties the gradient of the cost function is

$$\nabla J(\mathbf{x}) = \mathbf{B}^{-1}(\mathbf{x}_t - \mathbf{x}_b) + \mathbf{H}^T\mathbf{R}^{-1}\mathbf{H}(\mathbf{x}_t - \mathbf{x}_b) - \mathbf{H}^T\mathbf{R}^{-1}\{\mathbf{y}_0 - H(\mathbf{x}_b)\} \tag{5.22}$$

In a last step $\nabla(J(\mathbf{x}_t))$ is set to zero to make sure that J is a minimum and to obtain an equation for $\mathbf{x}_t$

$$(\mathbf{B}^{-1} + \mathbf{H}^T\mathbf{R}^{-1}\mathbf{H})(\mathbf{x}_t - \mathbf{x}_b) = \mathbf{H}^T\mathbf{R}^{-1}\{\mathbf{y}_0 - H(\mathbf{x}_b)\} \tag{5.23}$$

$\mathbf{H}^T$ is in this case the transpose of $\mathbf{H}$ and transforms vectors in observation space to vectors in model space. The operator $\mathbf{H}^T$ is especially important for indirect measurements such as radar or satellite observations. These types of observations must not only be mapped from the observational field to the analysis field: as they are indirect measurements meteorological data (temperature, humidity, wind) are calculated for example from non-linear integral measurements. Finally, the result for the variational (3D-Var) analysis problem is

$$\mathbf{x}_t = \mathbf{x}_b + (\mathbf{B}^{-1} + \mathbf{H}^T\mathbf{R}^{-1}\mathbf{H})^{-1}\mathbf{H}^T\mathbf{R}^{-1}\{\mathbf{y}_0 - H(\mathbf{x}_b)\} \tag{5.24}$$

The disadvantage of this solution is that the background error covariance matrix $\mathbf{B}$ needs to be inverted. As this matrix is an $N \times N$ matrix, where $N = i \times j \times k \times n$ is the dimensional space of the analysis (in the case of this study $N \approx 1152000$) given by the product of the dimensions of the spatial vectors and the number of variables, its inversion requires a lot of computational storage. The inversion can be avoided by creating an incremental form of this equation. The assumption is in this case that the maximum likelihood can be obtained by an incremental update to the initial background estimate which means that the final solution is expected to be not very far from the starting point. In each iteration the solution is defined by its deviation to the background state:

$$\delta\mathbf{x} = \mathbf{x}_t - \mathbf{x}_b \tag{5.25}$$

Merging the equation of the cost function $J(x)$ and 5.25 leads to the quadratic function

$$\begin{aligned} J &= -\frac{1}{2}(\mathbf{x}_t - \mathbf{x}_b)^T\mathbf{B}^{-1}(\mathbf{x}_t - \mathbf{x}_b) + \frac{1}{2}(H(\mathbf{x}_t) - \mathbf{y}_0)^T\mathbf{R}^{-1}(H(\mathbf{x}_t) - \mathbf{y}_0) && (5.26)\\ &= \frac{1}{2}\delta\mathbf{x}^T\mathbf{B}^{-1}\delta\mathbf{x} + \frac{1}{2}(\mathbf{H}\delta\mathbf{x} - \mathbf{d})^T\mathbf{R}^{-1}(\mathbf{H}\delta\mathbf{x} - \mathbf{d}) && (5.27)\\ &= J_{inc} && (5.28)\end{aligned}$$

with the already mentioned innovation vector. To avoid finally the inversion of the background error covariance matrix $\mathbf{B}$ this matrix can be decomposed into

$$\mathbf{B} = \sqrt{\mathbf{B}}\sqrt{\mathbf{B}^T} \tag{5.29}$$

respectively $\mathbf{B}^{-1}$ to

$$\mathbf{B}^{-1} = \sqrt{\mathbf{B}^{-1}}\sqrt{\mathbf{B}^{-1^T}} \tag{5.30}$$

With these decompositions the incremental cost function in 5.26 becomes

$$J_{inc} = \frac{1}{2}v^Tv + \frac{1}{2}(\mathbf{H}\sqrt{\mathbf{B}}v - \mathbf{d})^T\mathbf{R}^{-1}(\mathbf{H}\sqrt{\mathbf{B}}v - \mathbf{d}) \tag{5.31}$$

where $\mathbf{v} = \sqrt{\mathbf{B}^{-1}}\delta\mathbf{x}$ is the so called control variable. Calculating the gradient of 5.31 leads to

$$\begin{aligned} \nabla_v J_{inc} &= \mathbf{v} + \sqrt{\mathbf{B}}^T\mathbf{H}^T\mathbf{R}^{-1}(\mathbf{H}\sqrt{\mathbf{B}}\mathbf{v} - \mathbf{d}) && (5.32)\\ &= (\mathbf{I} + \sqrt{\mathbf{B}}^T\mathbf{H}^T\mathbf{R}^{-1}\mathbf{H}\sqrt{\mathbf{B}})\mathbf{v} - \sqrt{\mathbf{B}}^T\mathbf{H}^T\mathbf{R}^{-1}\mathbf{H}\mathbf{d} && (5.33)\end{aligned}$$

with the identity matrix $\mathbf{I}$. This form avoids now the inversion of $\mathbf{B}$ and reduces computational costs a lot.
Until yet no description of the background error covariance matrix or the control variable has been given. The transform from the control variable to an analysis increment can be written as an operator sequence $\sqrt{\mathbf{B}}\mathbf{v} = \mathbf{SDF}\mathbf{v}$. $\mathbf{S}$ is a spline transform that changes from randomly distributed values (observations) to a nodal representation (analysis). A detailed description of cubic B-splines can be found in Ooyama (2002). The following derivation is taken from Bell et al. (2012). The spline transform is defined as $\mathbf{S} = (\mathbf{P} + \mathbf{Q})^{-1}$ where $\mathbf{P}$ is determined by the method of least squares and $\mathbf{Q}$ is a third derivative constraint. They are defined as (in this case only one dimensional)

$$\begin{aligned}
\mathbf{P} &= [p_{mm'}]^T, \quad p_{mm'} = \int_D \phi_m(\mathbf{x})\phi_{m'}(x)dx \\
\mathbf{Q} &= [q_{mm'}]^T, \quad q_{mm'} = \int_D \epsilon_q(x)\phi_m'''(\mathbf{x})\phi_{m'}'''(x)dx \\
\phi_m(x) &= \Phi\left(\frac{x - x_m}{\Delta x}\right)
\end{aligned}$$

x is an arbitrary point of observation, Δx the size of subintervals, x_m denotes each equidistant node and ϵ_q is the non-negative weighting function of the third derivative constraint. The strength of this weighting function is selectable in the configuration. Φ is the cubic B-spline given by:

$$\Phi(\xi) = \begin{cases} \frac{1}{6}(1 - |\xi|)^3 - \frac{2}{3}(1 - |\xi|)^3 & \text{if } 1 \geq |\xi| \geq 0, \\ \frac{1}{6}(2 - |\xi|)^3 & \text{if } 2 \geq |\xi| \geq 1, \\ 0 & \text{if } |\xi| \geq 2. \end{cases} \tag{5.34}$$

Finally, a general form of the analysis can be derived at any arbitrary point by

$$u(x) = \phi^T \mathbf{v} + \tilde{\Phi}^T \tilde{\mathbf{v}} \tag{5.35}$$

where the boundary conditions are given by the last term in equation 5.35. The second and third term of the operator sequence defined above is on the one hand the standard deviation of the background errors **D** and on the other hand a recursive filter **F**. The standard deviation of the background errors strongly influences the constraint in data-poor regions. As a consequence, the selection of the standard deviation of the background errors had to be done very carefully in this study because of a non-uniform spatial coverage of observational data (see below). The recursive filter determines the distance of the influence of the information provided by an observation. For example a large value spreads the information of an observation but removes potentially important details from the analysis. The configurations chosen for this study are described in the following section.

5.2 SAMURAI configuration

For the analysis of the ELDORA data, satellite data (Atmospheric Motion Vectors) (Velden (1996)) and dropsonde data in SAMURAI a domain of 400 $km \times 400$ km with a horizontal resolution of 5 $km \times 5$ km is chosen. The vertical resolution is set to vertical increments of 0.5 km up to a height of 15 km. The analysis is performed in a reference frame moving with the TC, so that a time/position correction to all included data is accomplished assuming a linear storm motion calculated from the best track data. On 20 September 06

UTC the translation speed of Sinlaku was $u \approx 10.5\ m\ s^{-1}$ and $v \approx 0.6\ m\ s^{-1}$. The reference time for all observations is set to 06:00 UTC for this correction. All observational data are appropriately corrected and quality controlled by EOL. As a background field the operational analysis of the European Centre for Medium-Range Weather Forecasts (ECMWF) at a grid of $0.25° \times 0.25°$ is used. The 06 UTC analysis is taken to minimize the time span between observational time (05:00 UTC to 08:00 UTC on that day) and the ECMWF analysis time. The radius of influence of the background data is set to 30 km. Each background point is Gaussian distributed to this radius of influence. The following errors for the ECMWF analysis compared to the measurements are assumed: the horizontal wind and vertical wind error is set to 5 $m\ s^{-1}$, the temperature error to $5K$ and the specific humidity error to 5 $g\ kg^{-1}$. Especially the chosen vertical wind error improves the analyzed vertical wind field a lot and smooths the transition between regions with high and low observational density. Certainly this small vertical wind error (relatively to the true vertical motion) reduces the maximum vertical wind speed a lot, but the resulting vertical motion is still closer to the truth than the ECMWF. This hydrostatic model reduces the vertical motion to several 10 $cm\ s^{-1}$. Furthermore, the vertical motion is reduced by the relative coarse resolution of the ECMWF. Due to the coarse resolution, the ECMWF does not capture the convective nature of systems. Moreover, a lack of observational data causes a wrong structure in the first guess of the ECMWF analysis.

To reduce the influence of "bad" radar data and reduce the number of observations at each data point five radar strides are averaged and also Gaussian distributed to a radius of influence of 5 km. The reduction and averaging of five radar strides reduces the horizontal radar resolution to about 1500 m. As the chosen horizontal resolution is 5 km the average does not reduce the quality of the analysis. Any other observations (dropsonde data, satellite winds) are also Gaussian distributed to a 40 $km \times 40\ km$ radius of influence. About 3.29 million observations are incorporated in the analysis composites. As the bar chart in figure 5.1 (a) shows, 3.1 million Doppler radar observations are included and about 100,000 dropsonde measurements. The data distribution of all included data including background data is shown in figure 5.1 (b). The coordinates seen in this image and in all of the images in the following sections are given in km relative to the storm center taken from the best track on 20 September 06 UTC. For example, a coordinate of 100 km N and 100 km E denotes a location 100 km north and 100 km east to the best track positions. This designation coincides with the x- and y-axis labelings.

On 20 September 06 UTC, the best track position of Sinlaku was 35.1°N and 144.7°E. Almost all radar observations were taken east of the storm center (Fig. 5.1 (b)) in a time period between 0627-0700 UTC (Fig. 5.2 (b)). Although the flight itself was longer, the chosen time period could not be extended due to some problems with the aft-pointing antenna after strong turbulence (M. Bell, 2011, personal communication). Several dropsondes were released to the north and east of the remnant cyclone center. These are the dropsondes released by the C-130J. Several other dropsondes were released from the NRL P-3 along the flight track to the south and east of the cyclone center. On this day the NRL-P3 took off at Kadena at 02:35 UTC. The purpose of this mission was to investigate the development of the warm front during the ET of Typhoon Sinlaku. Given fuel con-

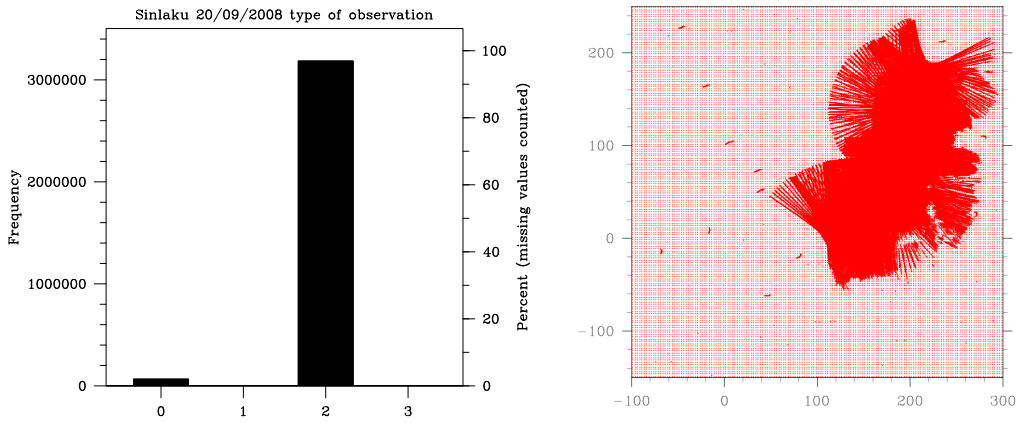

(a) (b)

Figure 5.1: Number of observations for each instrument (0=dropsonde, 1=flight level, 2=Doppler radar, 3=Atmospheric Motion Vectors) (a) and spatial distribution of all observations on 20 September included in SAMURAI analysis (b).

straints, the crew on board of the NRL-P3 decided to take advantage of the tailwind and go first to the warm sector of the decaying typhoon and fly then anticlockwise around the remnants of the typhoon. As a consequence, the NRL-P3 approached the convection from the south east, kept the convection to the left and went around the deep convection (see Fig. 5.2). On its flightpath along the eastern side of the system seven dropsondes were released at intervals of six minutes.

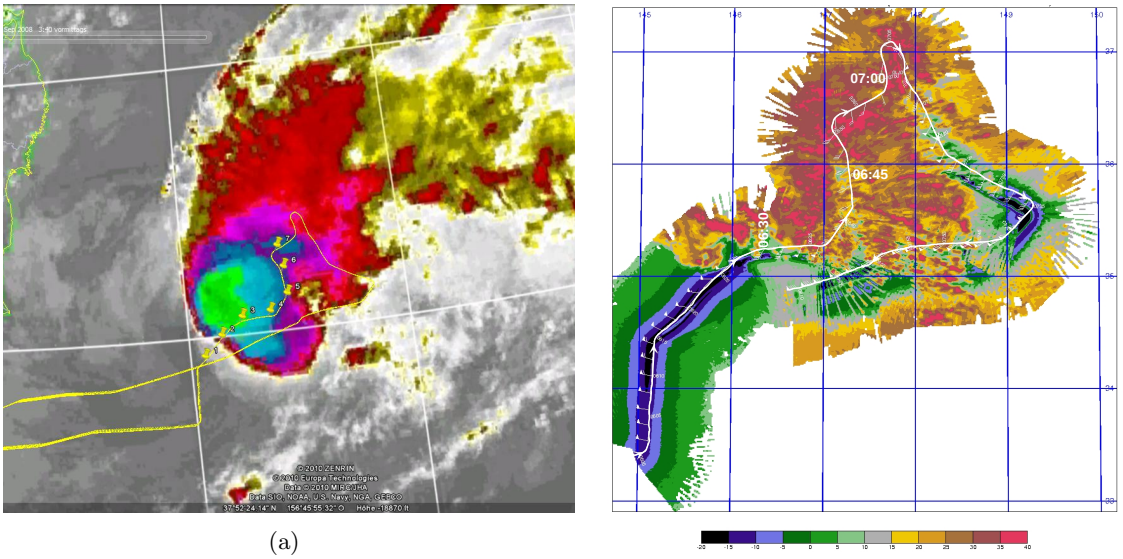

(a) (b)

Figure 5.2: (a): MTSAT IR image on 20 September at 06:30 UTC and flight track of NRL-P3. Marker denote positions of seven released dropsondes. (b): dBZ-composite from NRL-P3 research flight on 20 September with NRL-P3 flight track. Timestamps are given in UTC.

Due to extremely strong turbulences northeast of the deep convection the crew decided to leave this heavy precipitation region (M. Bell, 2011, personal communication). Flying to the south east instead to the west-northwest the NRL-P3 left the deep convection and

went back into the warm sector. A warm front could be identified along 36°N during the flight by the anticlockwise windshift and temperature measurements of the dropsondes. Due to fuel constraints a second passage through the warm front was not possible. During the flight a total of 20 dropsondes were released. The modified flight path prevented a flight around the deep convective system so that radar images are only available from the eastern part of the convection. However, this flight was almost certainly the first research flight ever to investigate the frontogenesis of a transitioning typhoon.

6. Structural characteristics of Typhoon Sinlaku

The large-scale structure during the ET of Sinlaku has been described in previous chapters using the ECMWF analysis and satellite imagery. In this chapter, the small-scale structure of Sinlaku is evaluated with the SAMURAI analysis based on observational data. All observational data of the NRL-P3 (ELDORA data, dropsondes), the C-130 (dropsondes) and satellite winds were assimilated with SAMURAI using the configurations described in section 5.2. The result of this assimilation is a detailed and very realistic image of Sinlaku's dynamical and thermodynamical structure during its interaction with the baroclinic zone. As several structural features were identified in SAMURAI, respectively in the observations, first a short overview will be given to mention them. These features are:

- deep convective region close to the circulation center
- stratiform precipitation region northeast to the circulation center
- warm and cold frontal structures
- remnants of a dry intrusion to the south/southwest of the circulation center

An overview of the features based on temperature, horizontal wind and reflectivity is given in figure 6.1. Furthermore, the figure gives an impression of the distribution of aircraft observational data. The reflectivity derived from the SAMURAI analysis shows maximum reflectivities of 39 dBZ at 1.5 km height at various locations (Fig. 6.1). These moderate values indicate strong precipitation but no hail as one could guess from the cloud top altitude and the circular spreading of the cloud tops seen in the satellite imagery. Between 80 km E to 200 km E and 20 km N to 80 km N an east-west elongated region is labeled as the deep convective region. ELDORA scanned this region as the NRL-P3 approached it from the south and circled around anticlockwise (see flighttrack in Fig. 6.1). Consequently, the dropsondes of the NRL-P3 measured the thermodynamic and dynamic structure to the south and east of the deep convection.

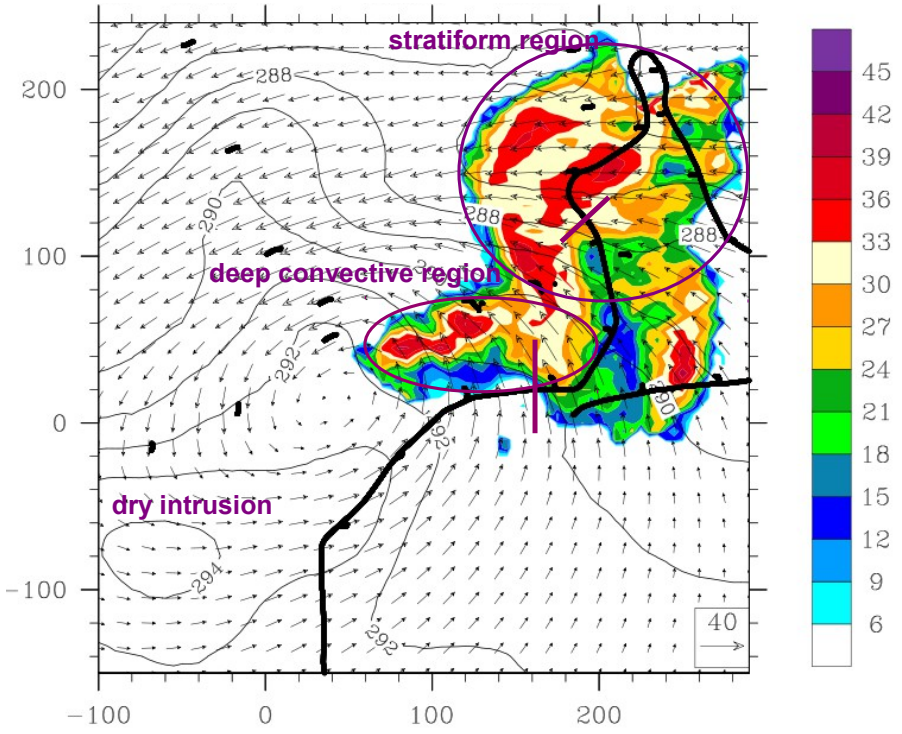

Figure 6.1: Overview of main features described in this study on 20 September. Reflectivity [dBZ] (shaded) and temperature [K] (contours) at 1.5 km derived from SAMURAI analysis. Black line denotes flight track of P-3 and black dots show locations of dropsondes released by the P-3 and C130. Thick magenta lines show positions of cross sections through raw radar data in figure 6.2 and figure 6.3.

The deep convective region is determined by a southerly flow at 1.5 km height (Fig. 6.1). On its flightpath in northerly directions the NRL-P3 reached a region which will be referred to as the stratiform region. This region is located north of 100 km N and east of 100 km E (Fig. 6.1). Passing through the stratiform region the NRL-P3 released several dropsondes. The C-130 released further dropsondes in this region. The reflectivity in the stratiform region exhibits values up to 39 dBZ at 1.5 km height. In contrast to the deep convective region an easterly flow determines the wind field in the stratiform precipitation region at 1.5 km height. As a consequence, a remarkable wind shift from southerly to easterly winds exists between the deep convective region and the stratiform precipitation region.

This windshift along 80 km N is collocated with a region of an enhanced temperature gradient at 1.5 km. The temperature gradient of 3 K $(60\ km)^{-1}$ with warm air to the south and cold air to the north was investigated by NRL-P3 and C-130 dropsondes. The reasons for labeling this region as a warm frontal region are given below.

The C-130 approached Sinlaku's circulation center from westerly directions and investigated the structure to the north of the TC during its flight. Seven dropsondes (black dots to the west and north of the circulation center in Fig. 6.1) measured a temperature difference of 5 K between 20 km S and 180 km N with northerly winds in the southern part and easterly winds in the northern part. The temperature gradient reaches its maximum

strength directly to the west of Sinlaku's circulation center along 0 km N. Furthermore, the wind shifts in this region from northerly to westerly. Both, the temperature gradient and the wind shift, indicate a cold frontal region.
Finally, a region south of 40 km S and west of 40 km E is labeled as a dry intrusion (Fig. 6.1). This region is determined by westerly winds at 1.5 km height and a region of comparable high temperatures. The dry intrusion was partially investigated by the NRL-P3 with two dropsondes. The reasons for labeling this region as a dry intrusion are given later in this section.
On the base of observational raw data the reasons for labeling the features as a deep convective region, stratiform region, warm frontal region, cold frontal region and dry intrusion are given in the following.

Deep convective region:
Vertical cross sections through the raw data in this area show radar echoes which appear as "cells" (Fig. 6.2). These are typical for young convective precipitation (Houze, 1997). The locations of the cross sections are given in Fig. 6.1. Additionally, the radar raw data do not show a bright band in the reflectivity which would be a typical indication for stratiform precipitation. The absence of a bright band indicates strong turbulence which prevents the development of this radar echo. Moreover, a cirrus shield in the radar raw data extending 60 km to the south suggests the existence of deep convection. Satellite images show, furthermore, that the cloud top temperatures reach lowest values in the described region of about 195 K. Because of these mentioned characteristics this region will be referred to as the deep convective region (Fig. 6.1).

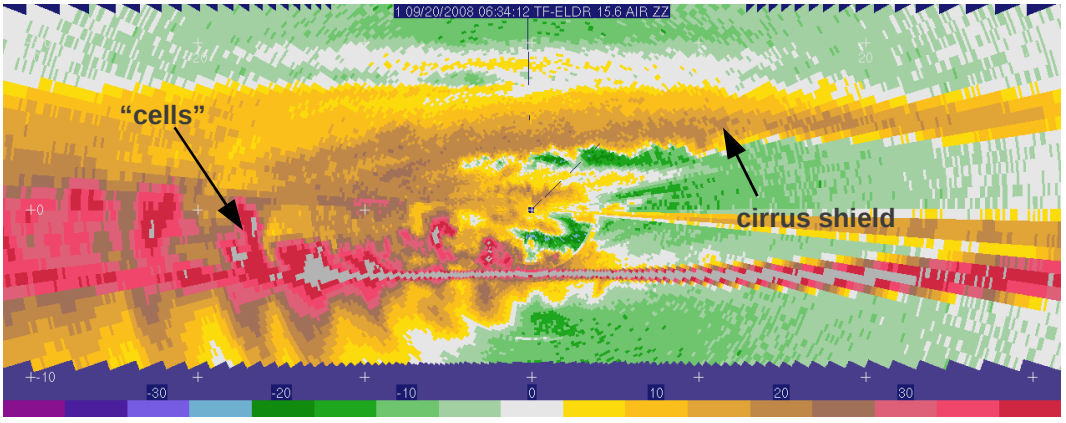

Figure 6.2: Raw reflectivity [dBZ] (not quality controlled) from the ELDORA front radar at 20.09.2008, 06:34:12 UTC.

Stratiform region:
A completely different precipitation region, the stratiform region, exists to the northeast of the deep convective region. The precipitation in this area is a lot more homogeneous and somewhat shallower. The cloud tops reach heights of about 10 km (in deep convective region 15 km). A cirrus shield cannot be seen as well (Fig. 6.3). The radar raw data show another important feature which is characteristic of stratiform precipitation. A bright band (melting layer) exists at a height of 4.3 km and below that fall streaks are seen (Fig. 6.3).

As described in Houze (1997) this bright band and the fall streaks below are a typical structure in stratiform precipitation. The relevance of the bright band for the analysis of the reflectivity is that the bright band leads to a significant attenuation. As a consequence, the reflectivities above the bright band may be underestimated considerably. Remarkable is the westward drift of the rain within the fall streaks. The westward drift exceeds 15 km, which indicates a strong easterly flow. The satellite imagery shows shallower convection in this region with cloud top temperatures greater than 215 K (Fig. 5.2 (a)). Circular spreading at the top, indicating strong vertical motion, is not seen. The analysis later in this study confirms these two classifications of convective and stratiform precipitation.

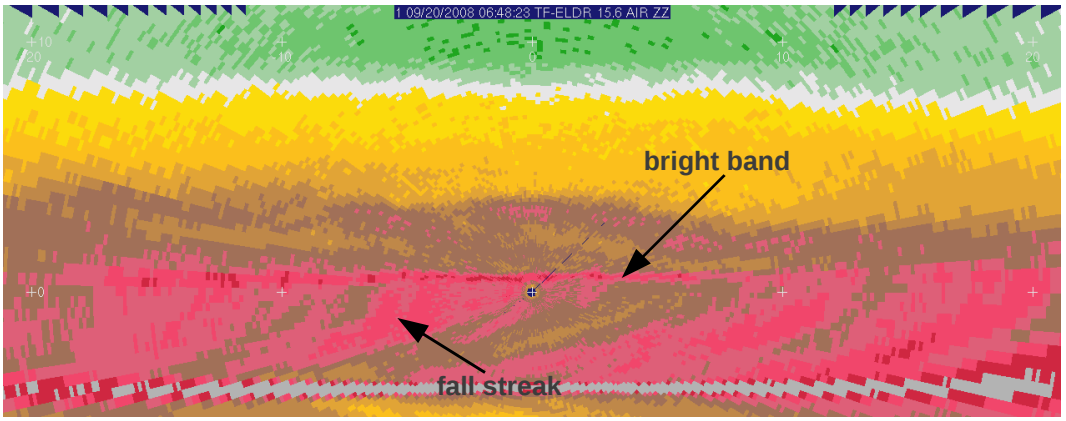

Figure 6.3: Raw reflectivity [dBZ] (not quality controlled) from the ELDORA front radar at 20.09.2008, 06:48:23 UTC. Colorbar the same as in figure 6.2.

Warm frontal zone:

As mentioned in section 5.2, the crew of the P-3 noticed a warm frontal structure east of the circulation center during the flight on 20 September. Dropsonde measurements of this flight show a temperature gradient from south to north and a simultaneous windshift from southwesterly to easterly directions at low levels (Fig. 6.4 (b, d)). The two presented dropsonde measurements exhibit a surface temperature difference of about 5 K. The vertical windshift from easterly winds at low levels to southerly winds above indicates strong warm air advection as another typical signature of a warm front. Furthermore, the dropsonde observations show an increase of the vertical layer with easterly winds moving northward (Fig. 6.4 (c, d)). This indicates a northward tilt of the frontal zone. Finally, the SAMURAI analysis shows the temperature gradient and the wind shift very obviously (Fig. 6.1). A detailed description of the warm frontal region will be presented later in this study.

Cold frontal zone & dry intrusion:

The cold frontal region was at least investigated partially by the C-130 on that day. Dropsondes were released along the frontal zone and especially to the north of it. The temperature measurements show a gradient of about $-3\ K$ from south to north. A strong windshift along the cold frontal zone cannot be seen in the observational data as the measurements were taken only slightly north of the frontal zone. However, the combination of P-3 dropsondes and C-130 dropsondes in the SAMURAI analysis shows a strong windshift from northerly to westerly winds. This windshift is almost collocated with the maxi-

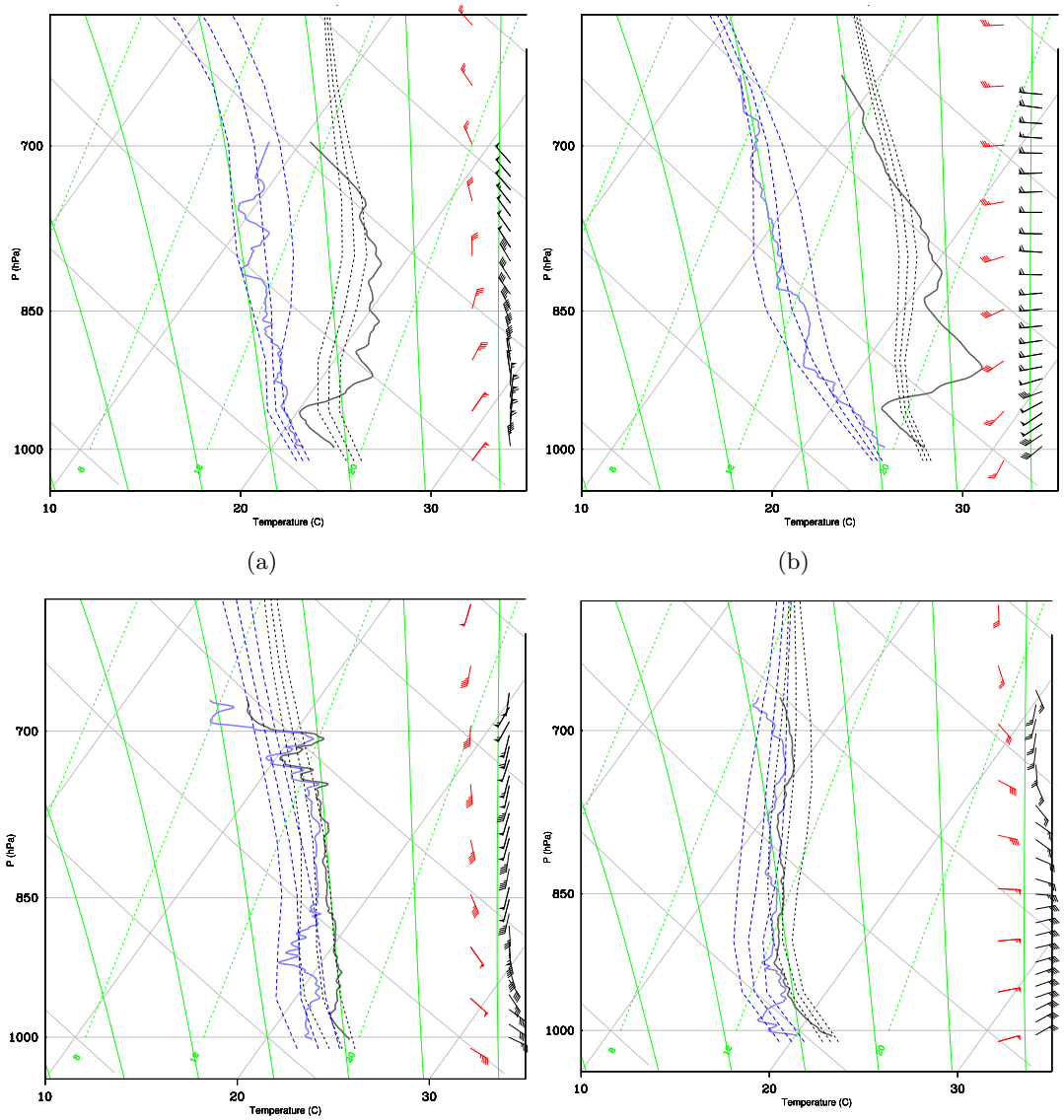

Figure 6.4: Measurements of dropsondes released from C-130 on 20 September at 05:20 UTC at 70 km E and 20 km S (a), and from the P-3 at 06:16 UTC at 20 km E and 60 km S (b), at 06:34 UTC at 180 km E and 20 km N (c), and at 06:52 UTC at 180 km E and 150 km N (d) in comparison to SAMURAI analysis. Thick dashed lines show SAMURAI analysis (blue=dewpoint, black=temperature), thin dashed lines are the standard deviation of the SAMURAI analysis in a box of 25 × 25 kilometer around the dropsonde location; solid lines are radiosonde measurements (blue=dewpoint, black=temperature). Red windbarbs from SAMURAI analysis, black windbarbs from radiosonde measurements.

mum temperature gradient along 0 km N to the west of the circulation center (Fig. 6.1). Additionally, a vertical wind shift in the dropsonde measurements from northerly to northwesterly winds indicates cold air advection (Fig. 6.4 (a)). As a result this region to the southwest of Sinlaku is labeled as the cold frontal region. The weak, respectively non existent convection in the cold frontal region with respect to the satellite imagery (Fig. 5.2 (a)) can potentially be explained by the fourth mentioned feature, the dry intrusion.

Satellite images show a region of dry air masses wrapping around the circulation center before the deep convective development. Satellite images on 20 September, 06:30 UTC, show remnants of this dry intrusion, respectively dry air masses to the west and southwest of the convection (not shown). Dropsonde measurements of both, the C-130 and the P-3, show dry air above 900 hPa (Fig. 6.4 (a, b)). The reason for interpreting the dropsonde measurements as a dry intrusion is a dry layer with a temperature to dew point temperature difference of 10 K and an almost dry adiabatic stratification above 900 hPa (Fig. 6.4 (b)), respectively above 750 hPa (Fig. 6.4 (a)). Additionally, a strong inversion of 5 K at about 900 hPa indicates descending air masses above this height. The trajectory calculations in section 3.1 showed this descent as well. In the SAMURAI analysis the dry intrusion can be detected as a region with locally highest temperatures to the southwest of the circulation center (Fig. 6.1). A detailed description of this feature is accomplished later on.

6.1 Deep Convection

The deep convection began to develop to the northeast of the circulation center at 02:30 UTC (see 3.1). As described in section 5.2, the observations were taken 2.5 to 5 hours later. The SAMURAI analysis shows that the southern part of the deep convection is located between 80 km E and 180 km E and between 20 km N and 100 km N according to the reflectivity (Fig. 6.1). The reflectivity reaches values of more than 9 dBZ (light precipitation) up to a height of 14.5 km in this region (Fig. 6.5 (f)). A cirrus shield broadens about 50 km to the south of the deep convection. As already mentioned in section 3.1, the extension of this cirrus shield reflects the strength of the vertical motion in this system. Cross sections from west to east (Fig. 6.5 (e)) show several convective cells reaching heights of about 6 km. This structure coincides with the radar raw data which showed convective cells also. Along 200 km E a gap in the reflectivity indicates the eastern border of the deep convection. Here the reflectivity does not exceed 15 dBZ throughout the troposphere. This gap coincides with the satellite imagery which showed a clear boundary between the regions with highest cloud top temperatures (deep convection) and the regions with lower cloud top temperatures (stratiform clouds) (Fig. 5.2 (a)). As a consequence, the region to the west of this gap corresponds to the region in the satellite imagery with cloud top temperatures lower than 215 K, i. e. to the deep convection. The region to the east of this gap corresponds accordingly to the stratiform region. Vertical cross sections show an elevation of the reflectivity from the ground in westerly directions (Fig. 6.5 (e)). This elevation is a result of attenuation and the removal of good data in the lowest elevation angle above ground during the quality control.
A second gap in the reflectivity can be identified in figure 6.5 (f) along 100 km N. To the south of this gap the reflectivity reaches 21 dBZ up to a height of 10 km. To the north of it, the reflectivity shows this value only below 6 km. As a consequence, two different types of convective activity exist to the north and to the south of the gap. Therefore, the region to the south of the gap corresponds to the deep convection and the region north of the gap to the stratiform precipitation region. Further to the east the gap between those two regions vanishes. The meaning of this gap will be elucidated later in this study.

The horizontal divergence exhibits maximum values of $-5 \cdot 10^{-4} s^{-1}$ in the deep convective region below 1.5 km height (Fig. 6.5 (a)). Its maximum is located at 100 km N and 120 km E. As figure 6.5 (a) shows the main convergence is located to the north of the measured reflectivity of the deep convection. Although the locations of maximum convergence and reflectivity do not coincide, this location of maximum convergence is consistent with the satellite imagery, that shows the lowest cloud top temperatures above this convergent region (Fig. 5.2 (a)). The lowest cloud top temperatures would be expected to occur in a region of strong vertical motion and therefore in a region of strong low level convergence. Due to the limited operating distance of ELDORA and the operational restriction of the NRL-P3 the reflectivity in this convergence region was not scanned. The location of strongest convergence is thus a result of the combination of radar data, background data and dropsonde data. From the examination of the satellite images it can be assumed that deep convection and strong precipitation and thus high reflectivity existed. As a consequence, the location of the strong low level convergence fits quite well with the location of the deep convective region. The convergence is associated with the confluence of a strong southerly and a strong easterly flow in this region (Fig. 6.5 (a)). The southerly flow exists primarily in the southern part of the deep convection and the easterly flow primarily in the northern part of the deep convection. The windshift within the deep convection and a noticeable temperature gradient indicate a warm frontal region (see section 6.3). Above 2 km height a divergence zone can be identified to the south of the system (Fig. 6.5 (b)). This divergent flow increases with height and causes maximum divergence with values of $2 \cdot 10^{-4} s^{-1}$ between 4 km and 8 km (Fig. 6.5 (c)). The reason for this divergent pattern is a diffluent flow along the border of the deep convection due to higher wind speeds in the convection than in the environment. Furthermore, the wind direction shifts from westerly winds south of the system to southerly winds in the convection. This windshift causes a weak diffluent zone especially to the southeast of the deep convection. The southerly flow determines the wind field up to 10 km in the deep convective region (Fig. 6.5 (e)). Above this height a primarily southwesterly flow passes through the cirrus shield. Northwesterly winds exist along the southern border of the cirrus shield. Vertical cross sections from south to north through the deep convection show vertical motion from the surface up to 15 km (Fig. 6.5 (f)).

Two branches of upward motion can be distinguished. The first one ascends from the southerly flow at low levels and leaves the analyzed domain between 7 km and 11 km height at 250 km N. This branch will be described in the context of the warm front and stratiform precipitation. The second branch consists of nearly upright ascent between 0 km and 150 km N. This branch exists throughout the complete troposphere up to the cirrus shield. An important side-note: the order of magnitude of vertical motion in the cirrus shield should not be interpreted quantitatively but rather qualitatively. The reasons are for example a non-uniform spatial distribution of observational data or smoothing by the background. However, the upright vertical motion in the cirrus shield is located between 50 km S and 50 km N (Fig. 6.5 (f)). The already mentioned northerly wind component along the southern border of the cirrus shield can be detected in the vertical cross sections above 11 km as well. This northerly component potentially leads on the one hand to the broad

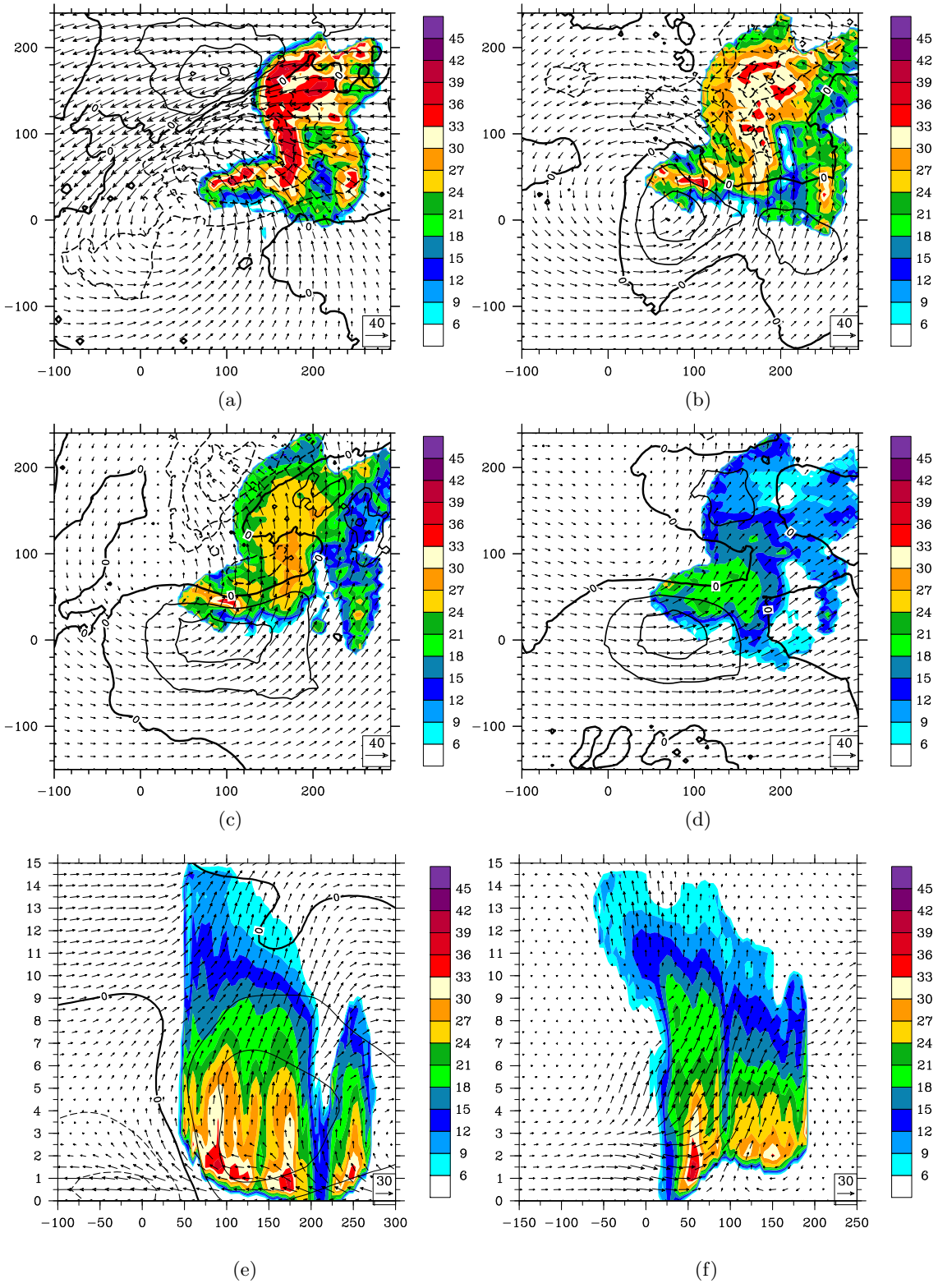

Figure 6.5: Reflectivity [dBZ] (shaded) and divergence $[10^{-5}s^{-1}]$ (contours with interval of $8 \cdot 10^{-5}s^{-1}$) at 1 km (a), 3 km (b), 5 km (c) and 8 km (d). Vectors are horizontal wind. Reflectivity (shaded), wind component perpendicular to cross section $[m\ s^{-1}]$ (contours with interval of 10 $m\ s^{-1}$) and wind vectors parallel to cross section from west to east along 50 km N (c). Reflectivity (shaded) and wind vectors parallel to cross section (v and w) $[m\ s^{-1}]$ from south to north along 125 km E (d).

cirrus shield extending southwards and suggests on the other hand an outflow out of the system. This conclusion is confirmed by a diffluent pattern collocated with the reflectivity in the cirrus shield (not shown). The flow direction in the cirrus shield strongly resembles an overturning updraft which has been proposed for convective systems for example by Moncrieff (1992). Notable is, furthermore, descent below the cirrus shield between 7 km and 10 km height.

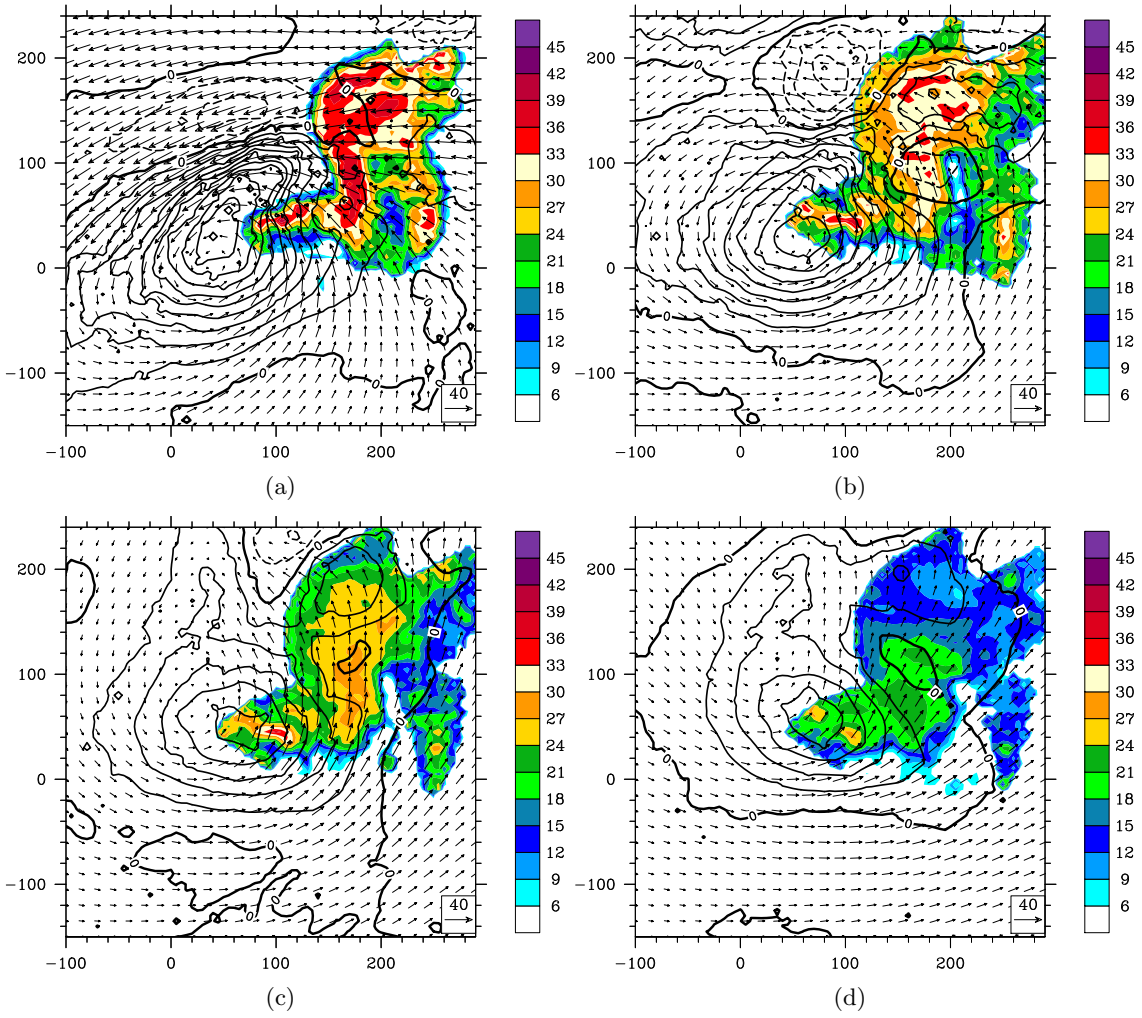

Figure 6.6: Reflectivity [dBZ] (shaded) and vorticity $[10^{-5}s^{-1}]$ (contours with interval of $8 \cdot 10^{-5}s^{-1}$) at 1 km (a), 3 km (b), 5 km (c) and 7 km (d).

The highest vorticity values exist to the west of the deep convection very close to Sinlaku's circulation center (Fig. 6.6 (a)). At 1 km height, for example, the highest vorticity values (about $10^{-3}s^{-1}$) occur at about 40 km E and 30 km N. A region with vorticity values exhibiting a similar order of magnitude extends into the convergent/deep convective region to the northeast of the circulation center as well. At 1.0 km height in the region of the low level convergence and, therefore, in the region of the deep convection the vorticity reaches values of about $8 \cdot 10^{-4}s^{-1}$ (Fig. 6.6 (a)). This is approximately the same magnitude as in Sinlaku's circulation center itself. Up to a height of 4 km the maximum vorticity is close to the circulation center. A remarkable change can be detected in the levels above. The circulation center shifts between 3 km (Fig. 6.6 (b)) and 5 km height (Fig. 6.6 (c)) about

60 km to the north and 20 km to the west. The vorticity maximum instead shifts 10 km northward. As a result the vorticity maximum is not close to the circulation center, but located in the southern part of the deep convection. At 7 km height the vorticity maximum of $4 \cdot 10^{-4} s^{-1}$ is collocated with highest reflectivity values at about 80 km E and 50 km N (Fig. 6.6 (d)). Thus, the vorticity maximum shifts slightly east-northeastwards with height. This tilt coincides with the almost westerly shear. However, it is comparatively upright with respect to the strong shear which is about 25 $m\ s^{-1}$ between 0 km and 10 km. A closed circulation center cannot be seen above 7 km but the wind field suggests that the remnant circulation center exists about 100 km north of the vorticity maximum. The various locations of the vorticity maximum and the circulation center might play an important role in Sinlaku's development later on.

Another important aspect for the development of the deep convection is the source of energy from the boundary layer and the stratification of the troposphere. A suitable variable to describe this is the moist static energy defined as

$$s_e = c_p T + gz + L_v r \tag{6.1}$$

where g is the gravitational acceleration, L_v the latent heat of vaporization, c_p the specific heat at constant pressure, T the absolute temperature, z the height above $z_0 = 0$ and r the water vapour mixing ratio. As the moist static energy is almost equivalent to the equivalent potential temperature, the isolines of moist static energy will be referred to as "moist isentropes" in the following.

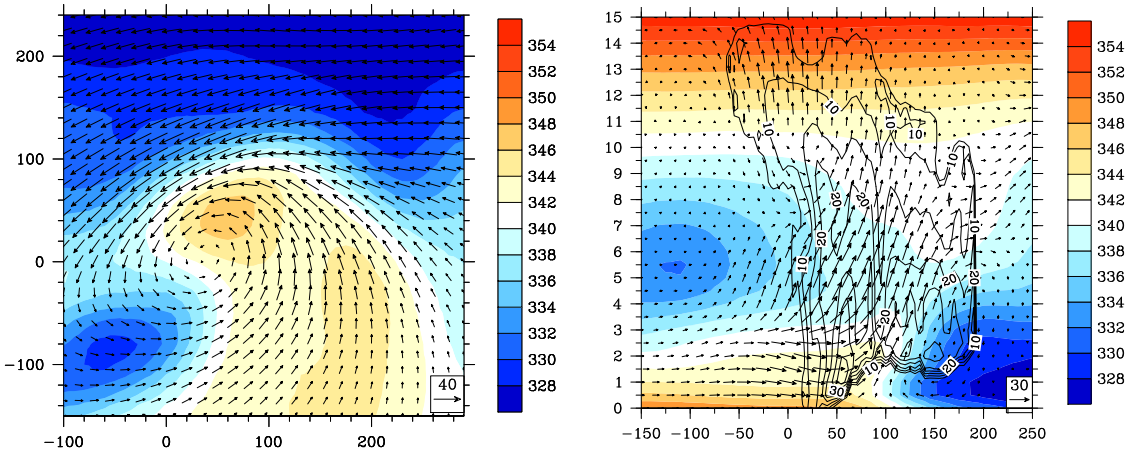

(a) (b)

Figure 6.7: Moist static energy $[kJ\ kg^{-1}]$ (shaded) at 1 km (a). Vectors are horizontal wind. Moist static energy $[kJ\ kg^{-1}]$ (shaded), reflectivity [dBZ] (contours) and wind vectors in cross section from south to north along 125 km E (b). The high values of moist static energy are disregarded at the lowest level due to the uncertainty of observational data.

The southerly flow to the southeast of the circulation center is collocated with a region of high moist static energy below 2 km (Fig. 6.7 (a)). As a consequence, this southerly flow advects warm moist air towards the deep convective system. The trajectory calculations in section 3.1 showed that this moist air originates from the subtropics and is advected northward along the western border of the subtropical anticyclone. The warm moist air above 0.5 km, especially in the planetary boundary layer, leads to surface-based instability. Additionally, the surface-based instability is enhanced to the south of the deep convection by a cold layer in the midtroposphere with a minimum of moist static energy at about 5 km (Fig. 6.7 (b)). This results in a potential instability as the moist static energy decreases with height. Dropsondes released by the NRL-P3 to the south of the deep convection (at 120 km E and 10 km N) document impressively the moist southerly to southeasterly flow below 900 hPa (Fig. 6.4 (a, b)). In this layer the southerly flow reaches values of 36 $m\ s^{-1}$. The temperature to dew point temperature difference is about 2 K which indicates comparatively high moisture. Above, a rather dry layer with southwesterly to westerly winds shows the dry intrusion (detailed description in section 6.4).
The potential instability in the deep convective region itself is reduced significantly between 50 km N and 100 km N (e. g. Fig. 6.7 (b)) as the moist static energy is nearly constant with height. The reason for this is vertical advection of moist static energy by the deep convection itself. Thus vertical motion in the deep convection reduces instability and transports moist static energy to higher levels, and thus neutralizes the unstable stratification. One assumption is that the potential instability in the deep convective region reached highest values before the convective development, respectively the potential instability of the environment shows the stratification of the atmosphere as it existed before the convective development.

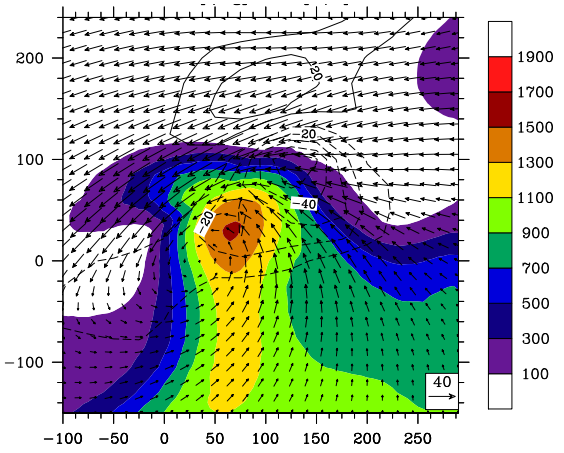

Figure 6.8: Most unstable CAPE [$J\ kg^{-1}$] derived from SAMURAI (shaded) and divergence [$10^{-5}s^{-1}$] at surface (contours).

To investigate the potential for convective activity the convective available potential energy (CAPE) was calculated from the SAMURAI output. The most unstable CAPE shows a local maximum of values up to 1600 $J\ kg^{-1}$ on the northeastern side of the typhoon where the deep convection developed (Fig. 6.8). Additionally it is collocated with a convergent region which could have forced ascent and triggered the convection. Assuming pure parcel

theory this value predicts a maximum vertical motion of $w_{max} = \sqrt{2CAPE} \approx 56\ m\ s^{-1}$. The derived vertical wind field does not show this vertical motion at all. One technical reason for this will be discussed later in this study.

6.2 Stratiform precipitation region

The stratiform precipitation region observed with ELDORA is located mainly between 100 km to 250 km N and 140 km to 300 km E of the best track circulation center (Fig. 6.1). In fact, the stratiform precipitation region was a lot larger, but not scanned completely during this research flight. In contrast to the deep convective region this part is characterized by a nearly uniform precipitation region with reflectivity values up to 42 dBZ (Fig. 6.9 (b)). Above a level of 4.5 km the reflectivity is lower than 33 dBZ. In contrast, the deep convective precipitation region has a reflectivity of about 39 dBZ at this level. A uniform reflectivity between 0 km and 200 km N indicates a stratiform precipitation region (Fig. 6.9 (b)). Higher reflectivities than 33 dBZ exist but these are mainly concentrated at lower levels. At a height of 11 km the reflectivity in the stratiform region vanishes completely. This fact suggests that a cirrus shield is not necessarily present in this part of the system and indicates a lower convective activity. Remnants of the cirrus shield broaden southwards to the south of the stratiform precipitation region (south of 0 km N) between 7 km and 12 km (Fig. 6.9 (b)). This shows, that deep convection and stratiform precipitation are still coexistent but not distinguishable by a gap in the reflectivity in this region (see Fig. 6.9 (a) as a comparison). A bright band (as it existed in the raw data, Fig. 6.3) cannot be seen in the SAMURAI analysis as it is not resolved with a vertical resolution of 0.5 km. This is more than the vertical extension of the bright band. Fallstreaks cannot be seen either due to the coarse horizontal resolution of 5 km.

The derived wind field shows a strong east-northeasterly flow below 1 km in the stratiform precipitation region with wind speeds up to 36 $m\ s^{-1}$ (Fig. 6.9 (c, d); 6.1). This flow has the structure of a low level jet and resembles a cold conveyor belt of a midlatitude low pressure system (in Fig. 6.9 (c, d) north of 100 km N). The flow is almost parallel to the isentropes along the baroclinic zone and seems to be isolated from the free troposphere due to a stable stratification in this region (Fig. 6.9 (c, d)). This fact potentially strengthens the flow due to lower momentum exchange with the free troposphere. With height the winds shift first in the southern part of the stratiform precipitation region to southerly winds with values about 24 $m\ s^{-1}$. These southerly winds ascend along the northward tilted moist isentropes in the region of the baroclinic zone and therefore represent the second branch of vertical motion described in the previous section. The strong clockwise windshift from northeasterly to southerly winds with height indicates a warm frontal region as the shift is associated with strong warm air advection from the south. The location of the low-level windshift from northerly to southerly winds at 100 km N (Fig. 6.9 (c)) is strongly correlated to the tilt of the moist isentropes along the baroclinic zone: in the lower troposphere northerly winds are collocated with cold and dry air (in Fig. 6.9 (c) north of 100 km N), southerly winds are collocated with moist-warm air (in Fig. 6.9 (c) south of 100 km N). In the mid-troposphere between 4 km and 9 km southerly winds determine

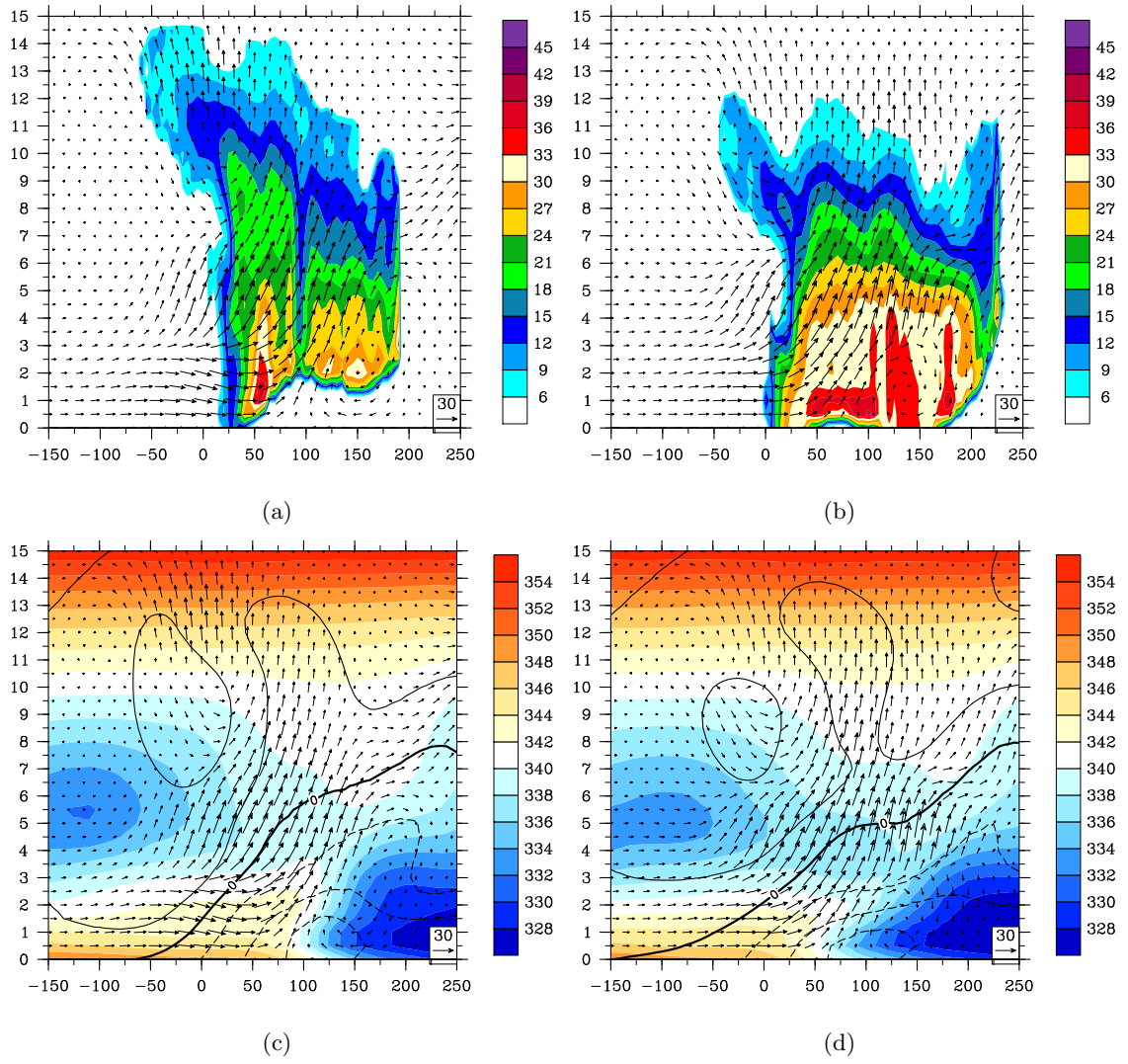

Figure 6.9: Reflectivity [dBZ] (shaded) along 125 km E (a) and 175 km E (b). Wind vectors are parallel to cross section (v and w) [$m\ s^{-1}$]. w is multiplied by ten. In (a): south of 100 km N deep convection, north of 100 km N stratiform precipitation. Moist static energy [$kJ\ kg^{-1}$] (shaded) along 125 km E (c) and 175 km E (d). Wind vectors are the same as in (a) and (b). Contours denote wind component perpendicular to cross section [$m\ s^{-1}$] (contours with interval of 10 $m\ s^{-1}$). Dashed contours denote component into the cross section.

the wind field in the complete analyzed stratiform precipitation region. Above a height of 10 km then a moderate westerly flow overflows the stratiform precipitation region.

Strong vertical motion begins to the south of the baroclinic zone (north of 50 km N) below 3 km and in the region of deep convection (Fig. 6.9 (a, c)). The southerly flow seems to ascend parallel to the planes of constant moist static energy. In the lowest 3 km the vertical upward motion reaches values of about 1.5 $m\ s^{-1}$. Above 3 km height upward motion already starts at 50 km S and accordingly to the south of the deep convection. Between 3.5 km and 6.0 km height a local maximum of vertical motion can be identified (Fig. 6.9 (c, d)). In the northern part of the stratiform precipitation region (north of 150 km N) strong ascent is separated from descent below at about 3.5 km height. An explanation for this upward motion is that air lifted along the moist isentropes (forced ascent) reaches the

level of free convection at this height and then ascends rapidly. However, this explanation cannot be proved by any dropsonde measurement due to an operating altitude of the NRL-P3 of about 3 km. Descent exists directly below this strong ascent with a magnitude of 1 $m\ s^{-1}$. The height at which the shift from ascent to descent occurs is almost collocated with the height of the bright band. This collocation is a typical signature of stratiform precipitation: strong vertical motion exists above the bright band, which leads to the growth of big raindrops/ice particles. After having reached a certain mass the particles drop out. This has been detected in the radar reflectivity as fall streaks below the bright band (Fig. 6.3). The big rain drops are able to induce downdrafts which can be detected in the vertical motion. Between 150 km N and 200 km N downdrafts of 1.0 $m\ s^{-1}$ exist (Fig. 6.9 (b)). Indeed, it is hard to prove that big rain drops induced downdrafts. Another, but completely different reason for descent might be, that the downward motion is the result of frontogenesis associated with the development of a thermal direct circulation. This thermal direct circulation can be identified between 75 km N and 175 km N up to 3 km height (Fig. 6.9 (b, d)). Its descending branch is collocated with the region of descent being potentially induced by big rain drops. Thus, the descent north of 150 km N in the stratiform precipitation region is either caused by big rain drops or by a thermal direct circulation or is the result of a combination of these processes. Positive vertical motion in the easterly flow can be excluded north of 150 km N due to a stable stratification along the warm frontal region. In the vertical cross section along 175 km E (Fig. 6.9 (b)) an overturning updraft in the cirrus shield still indicates an outflow region out of the system above 10 km height.

The divergence in the stratiform precipitation region at low levels differs completely from that in the deep convective region. At 1.0 km height for example a region of divergence extends from 10 km W to 220 km E north of 100 km N (Fig. 6.5 (a)). In contrast, strong convergence determines the deep convection at this height (see previous section, Fig. 6.5 (a)). The divergence partially exceeds values of $3 \cdot 10^{-4} s^{-1}$. The already mentioned downdrafts in combination with a thermal direct circulation cause the divergence in the stratiform precipitation region. Above 1.5 km height then, convergence determines the dynamics in the stratiform precipitation region as well. This convergence is again the result of the confluence of a southerly flow and low level easterly flow to the north (Fig. 6.5 (b)). As the warm frontal zone is tilted northward with height the windshift and as a consequence the confluent, respectively convergent region moves northward going up with height, too. At a level of 7.5 km the convergence in the stratiform region vanishes nearly completely (not shown). Instead above 8 km a divergent pattern exists in the northern part of the stratiform precipitation in a southwesterly flow (Fig. 6.5 (d)). This divergence in the northern part of the system indicates a flow out of the system in northeasterly directions. This outflow suggests an interaction between the midlatitude flow (jet) and the system. This interaction of a moist southerly flow and the midlatitude jet is again an important feature as it typical for warm conveyor belts in midlatitude cylones and for a TC in the transformation stage of ET.

An important difference between the stratiform region and the deep convection has been detected in the vorticity. Whereas strong vorticity occurs close to the deep convection at

lower levels (Fig. 6.6 (a)), almost no significant vorticity structure is seen in the stratiform region due to a mostly uniform wind field. Above a height of 5 km a mentionable vortical structure can be identified in the northern part of the stratiform region at 200 km N and 180 km E (Fig. 6.6 (c, d)). This vortical structure reaches its maximum intensity of $2 \cdot 10^{-4} s^{-1}$ at 6 km. It vanishes above 10 km and it represents the main vorticity structure beside the vorticity collocated with the deep convection. The vorticity structure will be interpreted later in this study in combination with the PV (see section 6.6).

In the last two sections main dynamic and thermodynamic structures have been presented occurring during Sinlaku's interaction with the baroclinic zone and the development of a convective system. The findings of the last sections are combined to create a coherent image of the complete system in the following.
The reflectivity in the deep convective region shows several intense, vertically extending, convective cells and a broad cirrus shield. The wind field in the deep convection is determined by a southerly flow up to a height of about 11 km and westerly wind above. Below 2 - 3 km the southerly flow is characterized by high values of moist static energy. Above, a layer with lower values of moist static energy between 3 - 10 km leads to potential instability. This southerly, potentially unstable flow enters the updraft in the deep convective region and ascends along the moist isentropes close to the baroclinic zone. The wind field in the cirrus shield of the deep convection is determined by an overturning updraft. The stratiform precipitation region is characterized by comparatively homogeneous reflectivity and shallower convection. Furthermore, the stratiform precipitation region can be partially separated from the deep convective region by a gap in the reflectivity and the existence of a bright band. The gap shows the existence of two completely different precipitation regions. The lowest levels of the stratiform precipitation region are determined by a strong, cold and dry east-northeasterly flow. The stratiform precipitation region is stably stratified due to the ascent of the warm moist southerly flow above this low level cold and dry easterly flow. Downward motion exists in this dry layer induced by melting and evaporation of precipitation particles, respectively downdrafts induced by heavy precipitation. As this cold region is collocated with the stratiform precipitation region **and** is close to the midlatitude baroclinic zone, it is hard to assess, whether the cold pool is a result of the stratiform precipitation, or just a part of the baroclinic zone. However, the combination of all those features leads to the conclusion that the described convection (deep convective region & stratiform region) are part of a mesoscale convective system; more precisely a mesocale convective complex. This conclusion is encouraged by the comparison of the derived image and conceptual models of mesoscale convective systems in recent studies. One of these images was introduced by Bryan and Fritsch (2000) who investigated mesoscale convective systems in the midlatitudes. They analyzed observational data (radar data, sounding data) and ran numerical models to simulate observed cases. In their study they observed similar structures with a moist southerly flow at low levels and a cold descending flow in the stratiform precipitation region. Furthermore, midtropospheric layers of lower moist static energy led to a destabilization and enhanced the convective activity. Another feature described by Bryan and Fritsch is the overturning updraft in the region of the

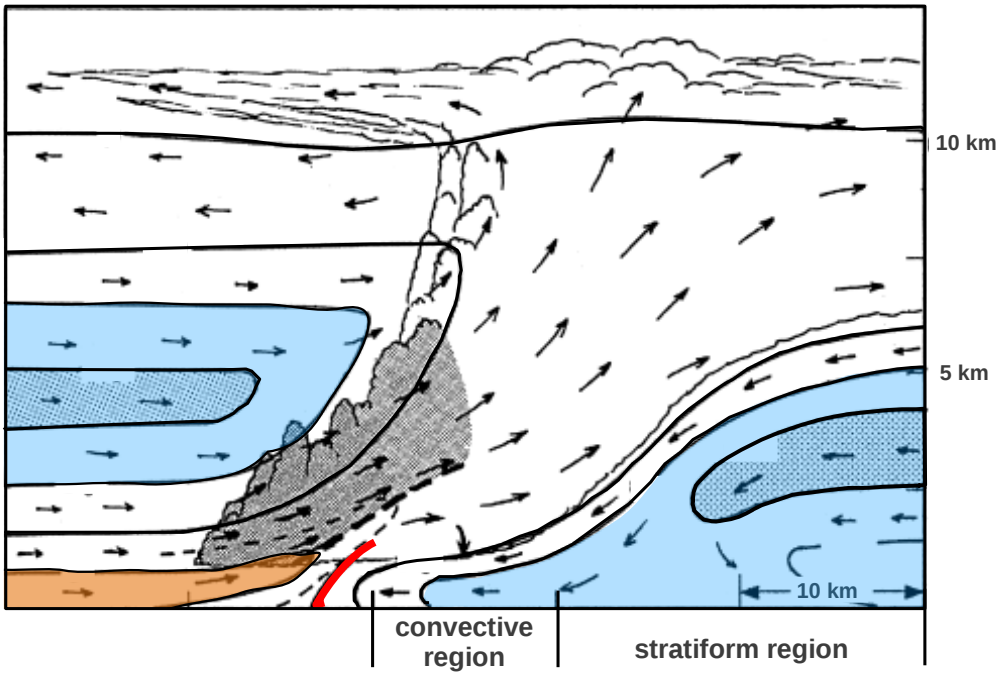

Figure 6.10: Idealized cross section through mesoscale convective system. Flow vectors are system relative, scalloped lines indicate cloud boundaries, solid lines are Θ_e contours every 4 K, solid red line indicates warm frontal zone, light blue shading highlights middle level layer of low Θ_e air, light red shading highlights low level layer of high Θ_e air. Adapted from Bryan and Fritsch (2000).

cirrus shield. The main difference between the observed mesoscale convective system in this study and the one in Bryan and Fritsch is the dimension of the observed systems. The mesoscale convective system that developed during the ET of Sinlaku is about ten times larger than the one described by Bryan and Fritsch's conceptual model. This fact is not surprising as Bryan and Fritsch's conceptual model was derived for squall line systems and not for mesoscale convective complexes with a lot larger diameter. The conclusion from the SAMURAI analysis (concerning to the MCC) coincides with the conclusion derived from satellite imagery in section 3.1. An idealized cross section through the convective system is given in figure 6.10. A comparison to the derived wind field in the SAMURAI analysis (Fig. 6.9 (a)) shows exactly the flow directions and thermodynamic structure of the conceptual model.

Bryan and Fritsch (2000) examined mesoscale convective systems along cold fronts of midlatitude low pressure systems. In the described case in this study, the mesoscale convective system developed to the east of a tropical cyclone during ET. As far as we know, these structures have been investigated on the base of observations for the first time. The most important question that one can pose, concerns the influence of the cyclone on the convective development and vice versa.

6.3 Warm frontal zone

By 20 September 06 UTC the initial development of a frontal wave is seen in both ECMWF (Fig. 3.7 (c)) and SAMURAI (Fig. 6.1). The structure of the temperature field is indicative of an interaction between a cyclonic wind field (the typhoon) and a zonally orientated temperature gradient (Keyser et al., 1988). The arching of the baroclinic zone is on the one hand a typical feature of midlatitude weather systems and indicates on the other hand a proceeding warm and cold frontogenesis. In this section the warm frontal zone is analyzed and in the following section the cold frontal region (to the west of the TC, Fig. 6.1).

Figure 6.1 shows a warm frontal region to the northeast of Sinlaku. The temperature gradient reaches maximum values of about 4 K $(70\ km)^{-1}$ along 100 km E at 0.5 km height. At 1.5 km the temperature gradient is slightly weaker but still a lot stronger than it would be in the case of a TC in the tropics (not shown). The region of the maximized temperature gradient is at 0.5 km height almost collocated with the deep convective system (not shown). Furthermore, the strongest temperature gradient is collocated with a convergent zone, which results from the confluence of a southerly and easterly flow (Fig. 6.1). Maximum ascent coincides with the convergent zone. The convergent zone shifts slightly northward with height, almost parallel to the isentropes (Fig. 6.11 (e)). As mentioned before, the convergence indicates that the frontogenesis is still proceeding. The temperature gradient weakens in easterly direction to 4 K $(170\ km)^{-1}$ at the end of the analyzed domain. Across the still developing warm front, the wind shifts from southeasterly to east-northeasterly winds. Vertical cross sections through the warm frontal region show several warm front typical structures. The isolines of moist static energy are northward sloped along the warm front. At 100 km E, between 100 km N and 150 km N, the moist isentropes show a steep northerly slope of about 7% in the low to mid troposphere (Fig. 6.11 (a, c, e)). This slope is about seven times as steep as the typical slope of a midlatitude warm front (Ahrens, 2012). North of 150 km N the moist isentropes have a shallower slope and are horizontally orientated at some locations. In the region of ascent along the moist isentropes, the stratification of the troposphere is almost neutrally but still conditionally unstable. Therefore it can be assumed that low level convergence forced ascent and, as a consequence, triggered strong vertical motion along the steeply sloped moist isentropes. The strong ascent along the sloping moist isentropes is part of a remarkable secondary circulation which can be identified near the warm front with upward motion to the south of the baroclinic zone (Fig. 6.11 (a, c, e)). This secondary circulation is centered at 150 km N and reaches a maximum height of about 6 km.

There is no ascent in the cold and dry air to the north of the warm front (north of 150 km N). The reason for this is a stable stratification due to the warm southerly flow above this cold air layer. This stands in contrast to the deep convective region and the region south of the baroclinic zone where the stratification was potentially unstable or at least neutrally stratified. Instead, descent with a magnitude of up to 0.5 $m\ s^{-1}$ occurs in the cold layer north of 150 km N (Fig. 6.11 (a)). This descent to the north of the warm front is part of the descending branch of the secondary circulation along the warm front. The descending branch of the secondary circulation is weaker than the ascending branch. This

suggests that the ascending branch is amplified by the convection and not only the result of frontogenesis in this region. This influence of diabatic processes additionally to adiabatic processes (frontogenesis) on ascent in frontal zones has been observed in several other studies also (Thorpe and Emanuel, 1995; Lagouvardos et al., 1993). In the descending region of the cold layer a divergent flow can be identified (Fig. 6.11 (e)). This divergent pattern coincides with downward motion and the flow out of this area into regions south of the baroclinic zone. For the case that the cold flow reaches the deep convection it presumably diminishes the convective activity due to a stabilization of the stratification. Another opportunity could be that the cold flow enhances the rear flank inflow into the convective system. This would lead to enhanced convergence and as a consequence would maintain the deep convection.
Vertical cross sections along 175 km E show completely different patterns in the vertical motion and in the structure of moist static energy. (Fig. 6.11 (b, d, f)). The main difference is a shallower tilt of the moist isentropes. The northward slope has decreased to 3.5%. In contrast to the stratification close to the deep convection along 100 km E, the stratification along 175 km E exhibits a strong conditional instability as the moist static energy decreases significantly with height. A minimum of moist static energy exists between 3 - 5 km height between 25 km N and 125 km N. At this height the upward motion originating from the boundary layer reaches maximum values up to 3 $m\ s^{-1}$ (Fig. 6.11 (b)) and is therefore stronger than the vertical motion along 100 km E (Fig. 6.11 (a)). The convergent pattern is similar to that along 100 km E with maximum convergence of about $-2 \cdot 10^{-4} s^{-1}$ at low levels to the south of the baroclinic zone. The combination of the described features along 175 km E leads to the following conclusion: In a conditionally instable environment low level convergence forces ascent above the level of free convection and therefore triggers strong vertical motion in the mid-troposphere. In contrast to the situation along 100 km E the latent heat release of the convection has not dissipated the conditional instability yet. Therefore the parcels originating from the boundary layer experience a greater buoyancy which results in a stronger vertical motion than along 100 km E.

The ascent described so far originates from the boundary layer. A region of ascent that does not originate from the boundary layer exists north of 125 km N above 3 km height (Fig. 6.11 (b)). This vertical motion possibly leads to the development of the stratiform precipitation. The upward motion shows striking maximum values up to 4 $m\ s^{-1}$ at 5 km. In the stratiform region of mesoscale convective systems only upward motion of tens of centimeters per second have been observed in previous studies (Biggerstaff and Houze, 1991). Below this region of elevated upward motion descent up to 1 $m\ s^{-1}$ occurs (Fig. 6.11 (b)). This downward motion is collocated with high reflectivity (Fig. 6.11 (d)) so that it is induced potentially by heavy precipitation, respectively big rain drops. Furthermore, the descent in the stratiform precipitation region is presumably amplified by cooling of midtropospheric air by melting and evaporation of precipitation particles.
Finally, at 200 km E the slope of the warm frontal region is reduced to 2.5% (not shown). The shallow slope of the moist isentropes is accompanied by a lower convergence. Anyway, the vertical motion has not decreased significantly. The secondary circulation along the warm front can still be seen but is a lot shallower than before. In contrast to the secondary

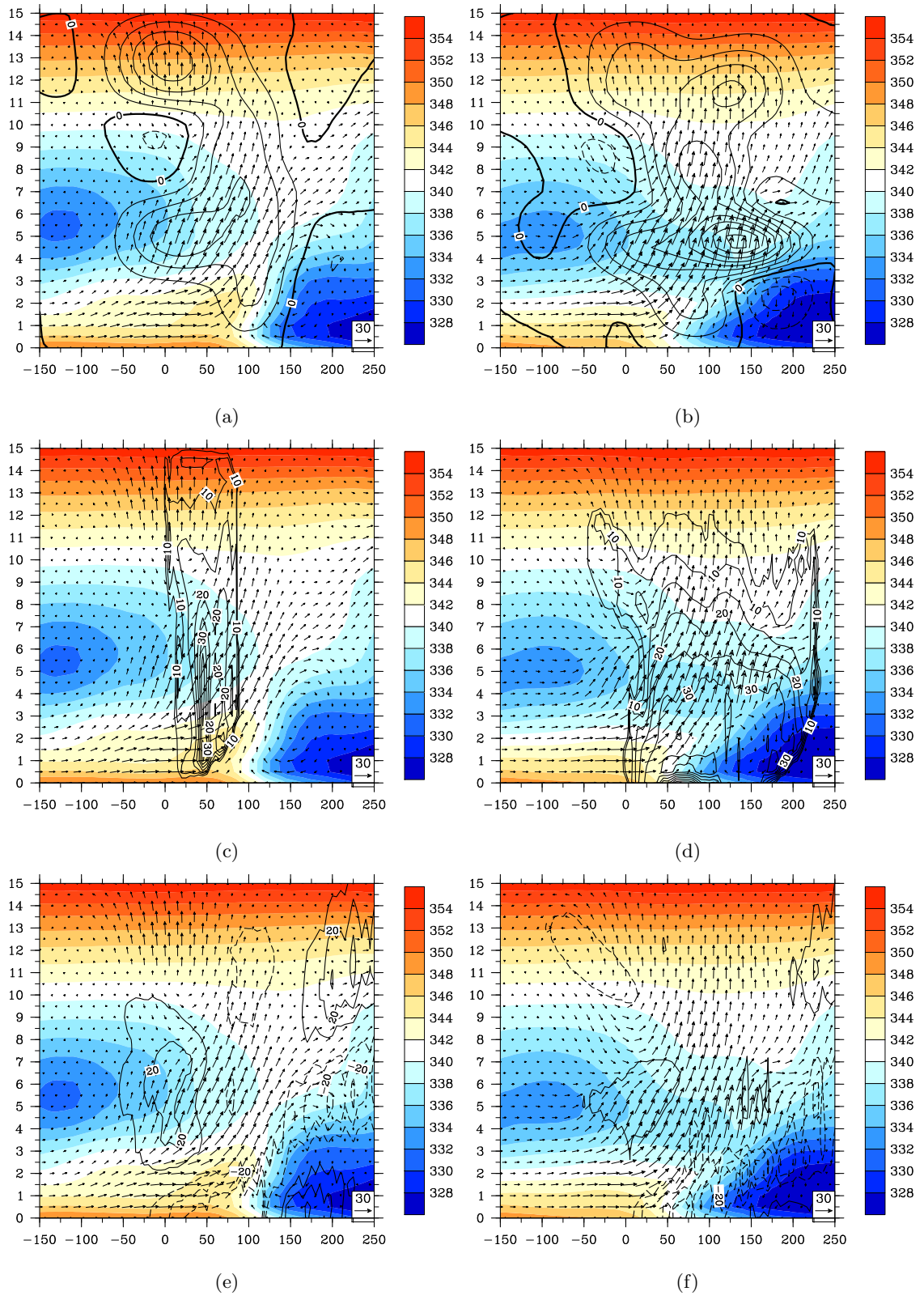

Figure 6.11: Moist static energy $[kJ\ kg^{-1}]$ (shaded), vertical wind speed $[m\ s^{-1}]$ (contours with interval of 0.5 $m\ s^{-1}$)) (a, b), reflectivity (contours) (c, d) and divergence (contours with interval of $10^{-4}s^{-1}$) (e, f) (a), (c) and (e) along 100 km E, (b), (d) and (f) along 175 km E. Wind vectors are parallel to cross section (v and w) $[m\ s^{-1}]$. w is multiplied by ten.

circulation along 100 km E the top of the circulation is now located between 3 - 4 km height. This suggests that the height of the secondary circulation depends on the tilt of the moist isentropes.

In the warm frontal region two different branches of ascent can be identified. They are derived from streamlines assuming a steady state in the analyzed domain (Fig. 6.12). One branch ascends northward nearly perpendicular to the isentropes of the warm frontal zone up to 600 hPa. This branch is located in the east of the analyzed domain and represents the environmental flow around Sinlaku. The second branch, which is closer to Sinlaku's circulation, wraps around the cyclone center and ascends on its way (up to 600 hPa as well). The air masses ascending along this branch originate from the moist boundary layer and are responsible for the almost upright vertical motion within the deep convection. In the region of deep convection latent heat is released. The air masses passing this area and wrapping around the cyclone advect warm moist air into upper levels to the north of the circulation center. Therefore, the stratification is stabilized/neutralized to the north of the cyclone. The maximum of moist static energy to the north of the cyclone is located between 2 km and 5 km (not shown). A description of the stabilization due to the deep convection can be found in section 6.1.

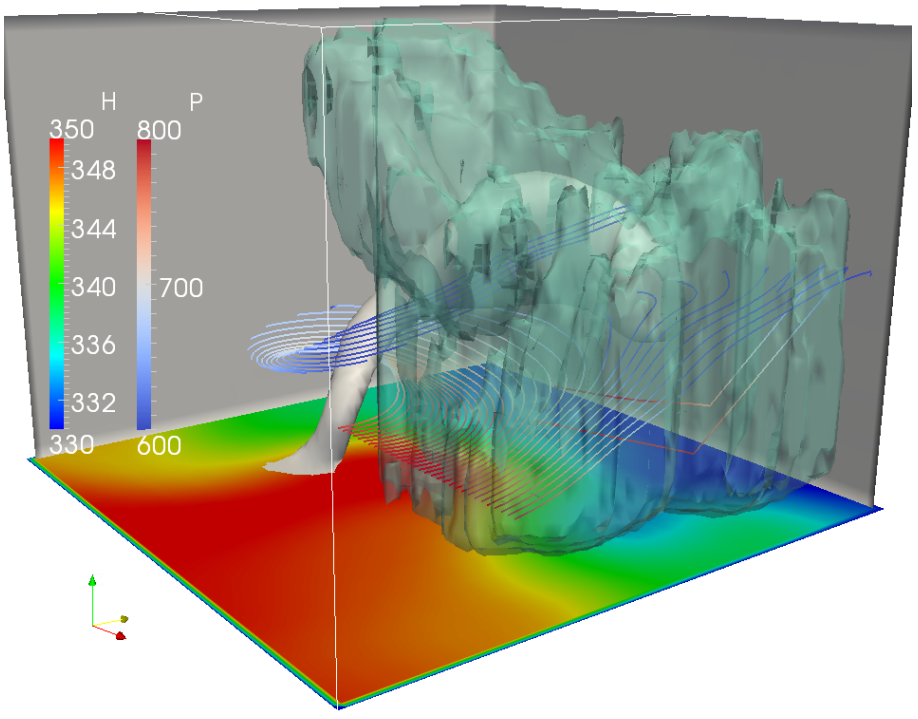

Figure 6.12: 3D view of SAMURAI analysis from southeast. Contour of horizontal wind speed (grey 5 $m\ s^{-1}$) indicating the typhoon, contour of reflectivity (dark green 5 dBZ) indicating the convective region, moist static energy (H) shaded, streamlines started at 800 hPa to the east of Sinlaku coloured by pressure (P).

6.4 Cold frontal zone/dry intrusion

The cold frontal zone is located to the west of the circulation center between 60 km S and 20 km N (Fig. 6.1). It is characterized by a temperature gradient of 3 K $(100\ km)^{-1}$ at 0.5 km height (Fig. 6.13 (a)) and a gradient in specific humidity of 3 $g\ kg^{-1}$ $(60\ km)^{-1}$ (Fig. 6.13 (b)). The windshift along the cold front is stronger than along the developing warm front. Winds shift from a strong northeasterly flow north of the cold front to a relatively weak westerly flow to the south of it. The wind shift causes a maximum of relative vorticity collocated with the cold frontal zone up to a height of 1.5 km (Fig. 6.6 (a)). Weak convergent structures indicate weak vertical motion along the frontal zone. However, the vertical motion does not exceed 0.5 $m\ s^{-1}$ (not shown).

The dropsonde measurements show a strong inversion in the region of the cold frontal zone of 5 K (Fig. 6.4 (a)). This inversion results in a strong convective inhibition, which suppresses convective activity in this region. The strong inhibition and the described inversion below dry air are the remnants of a dry intrusion which wrapped around the cyclone before the convective development. The convective inhibition calculated from the SAMURAI analysis reaches maximum values of about 260 $J\ kg^{-1}$ in the region of the cold front (not shown). Although low level convergence exists in a conditionally unstable environment and can trigger convection due to enforced ascent, the satellite images do not show any deep convection. The absence of convection along the cold front is an important contrast to cold fronts of the midlatitude weather systems which are accompanied by convection along the fronts and precipitation.
Another indication of the dry intrusion is the temperature field at 1.5 km height (Fig. 6.13 (a)). To the southwest of the circulation center and south of the cold frontal zone the temperature reaches a local maximum of 294 K. This local temperature maximum extends northeastward and is collocated with the derived circulation center at this height. Low values of specific humidity of 3 $g\ kg^{-1}$ indicate in the same region that this temperature maximum is not the warm core of the decaying typhoon. In the case of a warm cored typhoon the specific humidity would be a lot higher.
A remarkable feature is induced by the warm air of the dry intrusion as the result of dry adiabatic descent: to the east of the low level circulation center at 2.5 km height a north-south orientated temperature gradient of 3 K $(100\ km)^{-1}$ exists (Fig. 6.13 (e)). As a result, one gets the impression that the dry intrusion leads to the development of a midtropospheric “warm front” in the region of the cyclone. Furthermore, to the north of the cyclone a similar, but now west-east orientated temperature gradient exists. This west-east orientated temperature gradient is the upper part of the low level warm front described in section 6.3. Finally, at a height of 5 km the dry intrusion broadens a lot and is not distinguishable from the surrounding environment any longer (not shown). As a consequence of the low flight level of the two aircrafts, the confidence in temperature and humidity is not as strong as at lower levels. The temperature and the humidity are strongly influenced by the background field.
In summary, the collocation of a local maximum of temperature and a local minimum in specific humidity at low levels indicates that the observed structure is a (remnant of a) dry

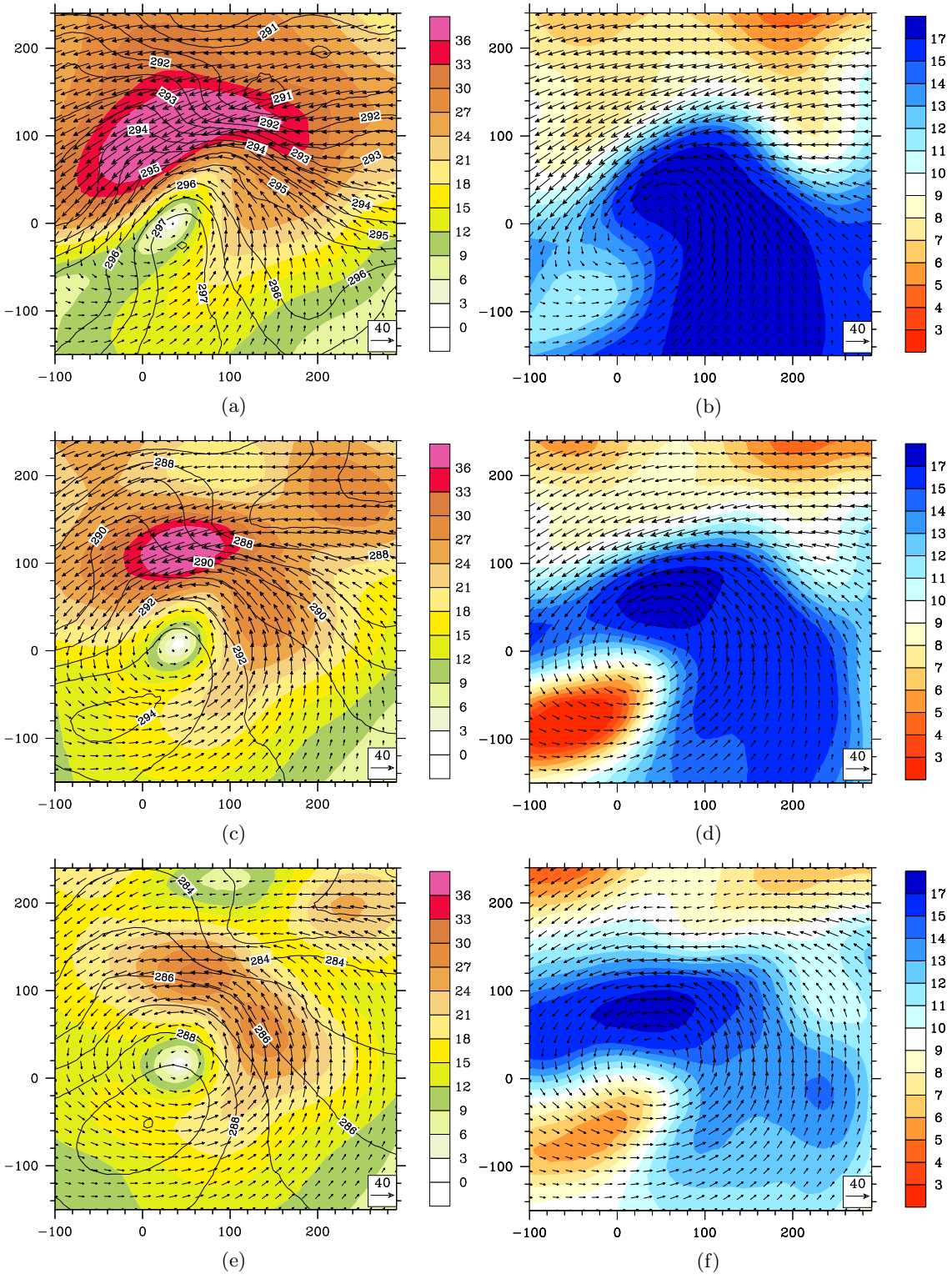

Figure 6.13: Wind speed [$m\ s^{-1}$] (shaded), temperature [K] (contours) and wind vectors (a, c, e). Specific humidity [$g\ kg^{-1}$] (shaded) and wind vectors (b, d, f). (a, b) at 0.5 km height, (c, d) at 1.5 km height, (e, f) at 2.5 km height.

intrusion. The anomalous high temperatures in about 1.5 km result in a strong inversion, a strong convective inhibition and consequently in a weak convective activity along the cold front and below the dry intrusion. In particular, the weak convective activity along the developing cold front is an important contrast to the cold front of a midlatitude low.

Especially in the case of conditional instability (as it exists in this case) cold fronts of midlatitude weather systems trigger deep convection as a result of low level convergence. Furthermore, the horizontal extension of the cold front (about 100 km) is very small in comparison to a front of a midlatitude weather system.

6.5 Circulation center

Previous sections showed the main structural features that developed during Sinlaku's ET. This section shortly describes the structure of the remnant typhoon.

At low levels Sinlaku's circulation center, with respect to the minimum of wind speed, is located at 25 km E and 0 km N. Cross section from south to north and from west to east will be used to describe the cyclones structure close to its center. The vertical shear calculated from the ECMWF exhibits values of 25 $m\ s^{-1}$ on 20 September 06 UTC (Fig. 3.6). It increased by about 10 $m\ s^{-1}$ from 19 September to 20 September. Therefore the shear possibly had an important impact on the cyclone's structural changes. The impact of the almost westerly shear on the cyclone can be seen nicely in the vorticity structure.

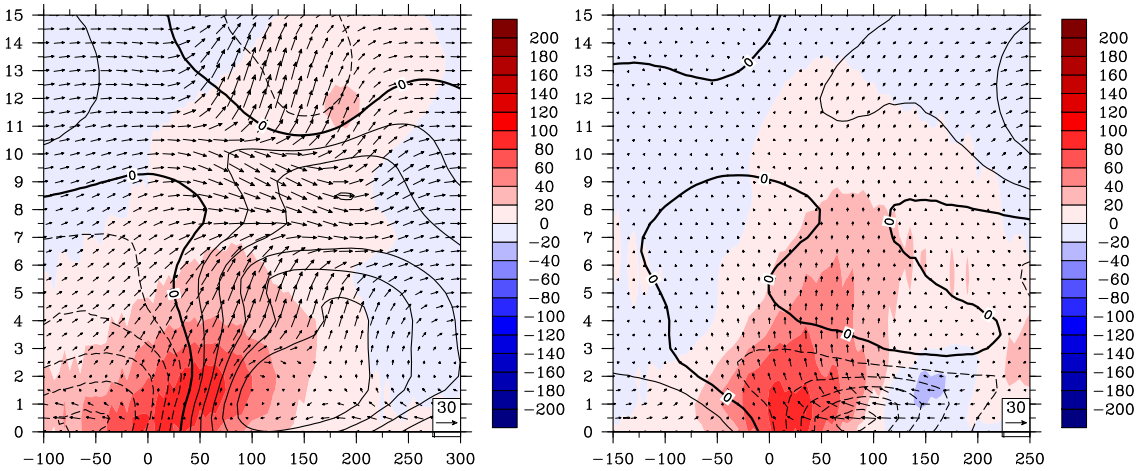

Figure 6.14: (a): cross section from west to east along 0 km N. Relative vorticity (shaded) $[10^{-5}s^{-1}]$, wind perpendicular to section (contours with interval of 4 $m\ s^{-1}$). Dashed contours denote component into cross section. Wind vectors are parallel to cross section (u and w) $[m\ s^{-1}]$. w is multiplied by ten. (b): same as in (a) except from south to north along 25 km E. Wind vectors are parallel to cross section (v and w) $[m\ s^{-1}]$.

A remnant of the TC's vorticity tower can be seen in figure 6.14 (a). Its maximum of $10^{-3}s^{-1}$ is located at low levels between 0 km and 50 km E. Values of $4 \cdot 10^{-4}s^{-1}$ can be detected up to 6.5 km along 75 km E. This shift of the vorticity maximum from low levels to 6.5 km represents an eastward tilt of Sinlaku's remnant vorticity tower. A northward tilt can be derived from south-north cross sections along 25 km E (Fig. 6.14 (b)). Whilst the vorticity maximum is located at low levels between 0 km and 25 km N, it is located along 75 km N at about 9 km. As a consequence the remnant vorticity tower of Typhoon Sinlaku is tilted to the downshear left, i. e. in northeasterly directions. This downshear left tilt coincides with the results of several numerical studies. Comparing the minimum

of the wind speed with the maximum of low level vorticity (Fig. 6.14 (b)) a displacement between those features can be detected. Furthermore, the wind speed shows a strong asymmetry below 3 km. A strong northeasterly low level jet exceeds 30 $m\ s^{-1}$ at some locations to the north of the low level vorticity maximum, whereas westerly winds to the south of the center are a lot weaker and only exceed 15 $m\ s^{-1}$. The vorticity maximum itself is collocated with a region of easterly winds at low levels. Above 3 km the region of highest vorticity is located in a region of westerly winds. Therefore, the remnant vorticity tower is exposed to a strong westerly shear with easterly winds below 3 km and westerly winds above. This westerly shear potentially accelerates the TC's decay. The asymmetry of the horizontal wind in west-east direction is somewhat weaker (Fig. 6.14 (a)). The asymmetry is mainly the result of a strong southerly flow to the east of the TC's center and a comparable weak northerly flow to the west below 6 km.

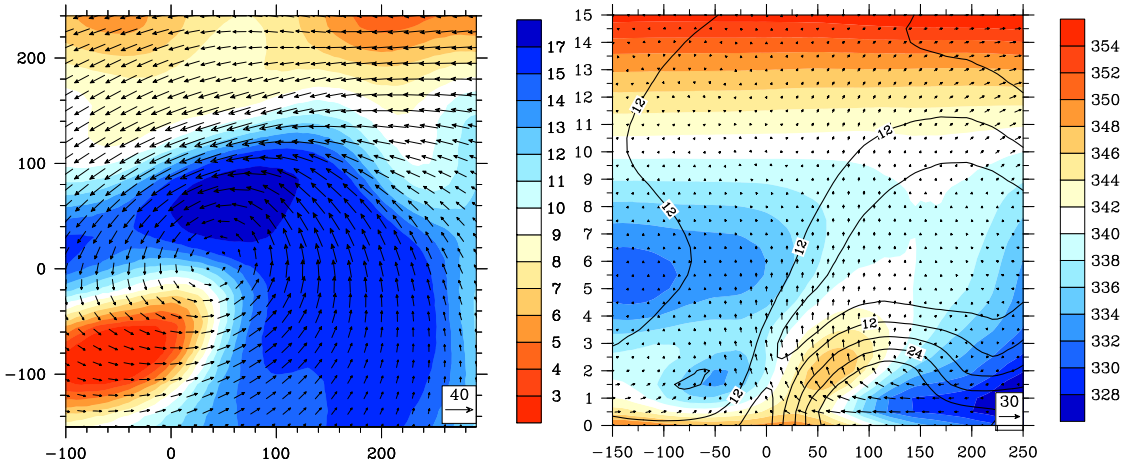

(a) (b)

Figure 6.15: (a): Specific humidity [$g\ kg^{-1}$] (shaded) and wind vectors [$m\ s^{-1}$] at 1.5 km height. (b): Vertical cross section from south to north along 25 km E, shaded is moist static energy [$kJ\ kg^{-1}$], contours with interval of 6 $m\ s^{-1}$ denote horizontal wind speed, wind vectors are parallel to cross section (v and w) [$m\ s^{-1}$]. w is multiplied by ten.

Horizontal cross sections show that Sinlaku's circulation center is centered on a strong gradient of moist static energy (Fig. 6.7 (a)), which results particularly from a moisture gradient (Fig. 6.15 (a)). This strong moisture gradient is induced by the dry intrusion to the southwest of the cyclone and warm moist air to the northeast. The specific humidity exhibits a remarkable gradient of 14 $g\ kg^{-1}$ $(150\ km)^{-1}$ at 1.5 km height. Vertical cross sections from south to north show that the circulation center (taking the minimum of wind speed) and the moist static energy gradient are collocated up to 4 km height (Fig. 6.15 (b)). The warm and moist air is located to the north of the circulation center. As streamlines showed under the assumption of stationarity in section 6.3, this warm moist air originates from the boundary layer and is advected upward and to the north of the TC's circulation center. This upward transport of moist static energy leads to a neutralization and therefore reduces the convective activity to the north of the cyclone which leads most probably to the observed asymmetric cloud structure. A comparison with figure 6.14 (b) shows the

collocation of maximum moist static energy and maximum vorticity to the north of the cyclone. This collocation suggests that the advection of warm moist air produced vorticity with respect to the solenoid term in the vorticity equation. Moist and warm air can be found at low levels to the south of the circulation center (Fig. 6.15 (b)). Above 1 km and between 100 km S and 0 km a part of the dry intrusion is represented by comparable low values of moist static energy. Low level warm moist air and dry air above results in a conditional unstable environment. However, as described in the previous section, warm air in the region of the dry intrusion leads to a strong inversion and therefore reduces the convective activity.

6.6 Potential vorticity structure

The PV combines the dynamic and thermodynamic characteristics of the system of interest and simplifies the interpretation of observed structures. As the SAMURAI output is in height coordinates the PV is approximated by $PV = \rho^{-1}(\zeta + f)\frac{\partial \Theta}{\partial z}$ using the hydrostatic approximation. The Coriolis parameter f is assumed to be constant and the vertical component of the relative vorticity to be dominant. Following main PV features are evaluated in the following:

- positive low-level PV anomaly associated with Sinlaku's circulation center
- positive mid-level PV anomaly due to diabatic processes
- positive PV anomaly in ascending region along baroclinic zone
- positive PV anomaly in mid- and upper-levels due to advection of high PV from low levels

Low-level PV anomaly associated with Sinlaku's circulation center:
The low-level PV (below 1 km) is characterized by a strong positive PV anomaly with values exceeding 6 PVU[1], associated with the circulation center of ex-Sinlaku (Fig. 6.16 (a)). The vorticity (Fig. 6.6 (a)) showed a region of higher values collocated with the developing cold front to the west of the circulation center. The PV shows a similar structure associated with a strong windshift along the cold front from northeasterly to westerly winds (section 6.4). This windshift causes an important asymmetry in Sinlaku's wind field. As the cold front's vertical extent is limited to the lower troposphere the asymmetry vanishes at 2 km height. This coincides with the PV structure at 2 km. At this height the PV decreases significantly along the cold front and it is not linked anymore to the windshift along the cold front (Fig. 6.16 (b)). The reason for the low vertical extend of the cold front is the dry intrusion above. As described in the previous section the dry intrusion causes a strong inversion and consequently a strong convective inhibition. This convective inhibition leads to a decrease of convective activity and as a consequence to reduced latent heat release. As latent heat release is responsible for the production of PV, it does not increase as well. Consequently the windshift is reduced and the TC's

[1] $1\ PVU = 1 \cdot 10^{-6} Km^2 s^{-1} kg^{-1}$

symmetry maintained. Therefore one can conclude that the cyclone's circulation is deformed in the lower troposphere (planetary boundary layer) by the developing cold front. The dry intrusion reduces the vertical extent of the cold front, so that the deformation due to the windshift vanishes above the planetary boundary layer (in this case 1.5 km to 2 km). This again results in a quite symmetric circulation above this height. A small part of the PV extends northeastward into the deep convective region (Fig. 6.16 (a)). The center of the PV shifts east-northeastwards with height towards the center of the deep convection. The PV weakens up to 3 km height, where it reaches about 4 PVU (Fig. 6.16 (b)).

Mid-level PV anomaly due to diabatic processes:
Above 3 km the PV restrengthens in the deep convective region resulting in a second PV maximum at 6 km height of more than 6 PVU (Fig. 6.16 (c, e)). At this height the PV maximum is in the region of the highest reflectivity values and therefore associated with the deep convection. An explanation for this second maximum at mid-levels and its proximity to the deep convection is the diabatic production of PV by latent heat release in the convective region which is described by $\frac{d(PV)}{dt} = \rho^{-1}(\zeta + f)\frac{\partial \dot{\Theta}}{\partial z}$. The development of such a mid-level PV anomaly is described, for example, in Pomroy and Thorpe (2000). In Pomroy and Thorpe (2000) the mid-level PV anomaly is a result of steady condensation along the frontal zone. The proximity of the mid-level PV anomaly to the deep convection in this case suggests that it is a result of steady condensation in the deep convection. A closed circulation around Sinlaku does not exist at 6 km, so that the remnants of the storm resemble a trough (Fig. 6.16 (c)).

Therefore, the question arises whether the cyclonic circulation is a midlatitude upper level trough or the remnant of Sinlaku's circulation. The ECMWF did not show an upper level trough, but an almost zonal midlatitude flow (section 3.1). This suggests that the wind field at 6 km is a remnant of Sinlaku's circulation and not a midlatitude trough. The axis of the "trough" (Sinlaku's circulation) is collocated with the maximum of PV and accordingly with the deep convection. For this reason, latent heat release in the deep convection leads to a production of PV. The PV again strongly influences the wind field and potentially forms the cyclonic windshift along the southern border of the circulation. Moreover, the PV structure is elongated from south to north at 6 km in a southerly flow (Fig. 6.16 (c)). This constellation indicates a horizontal advection of PV from the region of maximum PV production in northerly directions. The advection and the resulting elongation of the PV anomaly potentially strengthened the formation of a wind field similar to that of a trough. The described considerations lead to the conclusion that the deep convection is responsible for the production of PV and consequently for a modification of Sinlaku's circulation.

Two weak upper level negative PV anomalies exist to the south and north of the upper level positive PV anomaly (Fig. 6.16 (e)). A reason for their horizontal displacement from the deep convection is either advection of these anomalies or the modification by diabatic processes in this region. A third PV maximum located above 12 km and collocated with the cirrus shield will be ignored in the following (Fig. 6.16 (e, f)). The data coverage is very bad at this height and the only observational data are from radar and satellite winds.

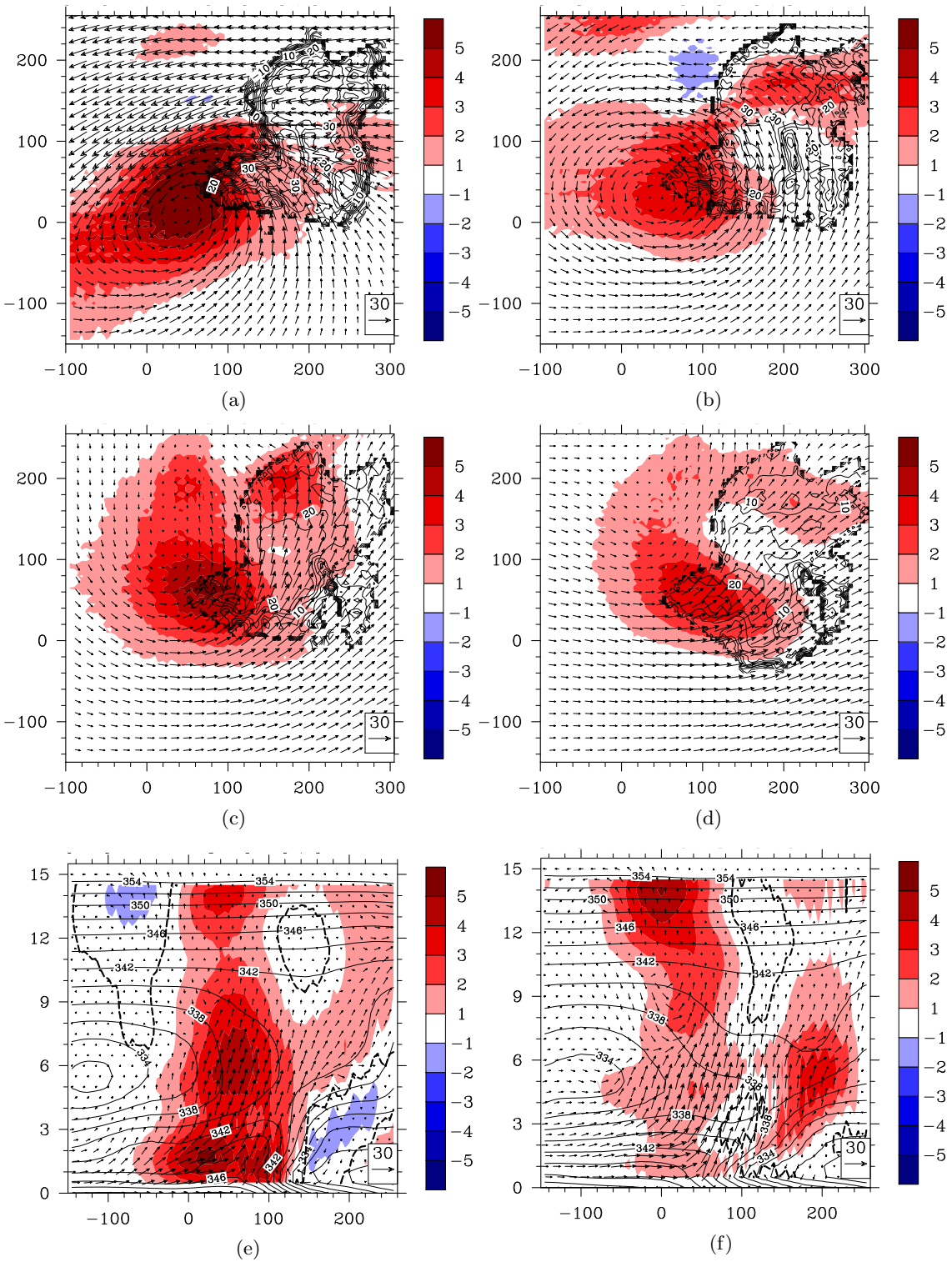

Figure 6.16: Potential vorticity [PVU] (shaded) and reflectivity [dBZ] at 1 km (a), 3 km (b), 6 km (c) and 8 km (d) height. Potential vorticity (shaded) and wind parallel to cross section (v and w) [$m\ s^{-1}$] along 100 km E (e) and 175 km E (f). Contours denote moist static energy [$kJ\ kg^{-1}$]. In (e) and (f) thick dashed line denotes 0.2 PVU.

Plots of horizontal wind speed show above 12 km a strong gradient from areas without any observational data to areas with observational data. Although the observational data are transformed with B-splines (section 5.1) this gradient is most probably a result of the spatial data coverage and did not exist in reality.

PV anomaly in ascending region along baroclinic zone:
Latent heat release has influenced the PV structure in the stratiform precipitation region as well. Vertical cross sections through the stratiform precipitation region along 175 km E exhibit PV structures elevated from the surface north of 100 km N (Fig. 6.16 (f)). The PV reaches values of 1 PVU above 1 km and 3 PVU above 3 km. The elevation of the PV from the surface seems to be strongly correlated to the tilt of the moist isentropes along the baroclinic zone. It can be assumed that in the cold and dry layer precipitation leads to a reduction of PV. In the moist-warm flow above instead, latent heat release generates PV. The consequence are regions of positive PV anomalies up to 10 km and regions of weak PV below.

PV anomaly in mid- and upper-levels due to advection of high PV from low levels:
The vertical cross sections along 100 km E (Fig. 6.16 (e)) show another remarkable feature south of the baroclinic zone (north of 110 km N). The PV structure (potential vorticity tower) of the cyclone/deep convection can be identified. Between 5 km and 15 km and north of the low level baroclinic zone (north of 150 km N) an area of positive vorticity values lower than 1 PVU is collocated with an area of upward motion. This positive upward motion is the result of ascent along the isentropes in northerly directions. This feature indicates the transport of PV towards the midlatitude jet and suggests an outflow out of the typhoon. Assuming a steady state of the system streamlines were calculated passing the mid tropospheric PV maximum (Fig. 6.17).

This calculation shows a spiraling of the streamlines around the cyclone and continuous upward motion from the low to mid troposphere. After having passed through the midtropospheric PV maximum the streamlines ascend slightly in northerly directions. The maximum height is about 400 hPa. This northerly and ascending flow indicates as well an flow out of the system. In contrast to the outflow described with the help of vertical cross sections the flow represented by the streamlines is much lower (only 6 km instead of 9 km - 15 km). As a consequence, trajectories need to be calculated to get information about the true height of the outflow. This of course is not possible as the SAMURAI analysis was only derived for a single point of time.
The analysis from the PV structure from the SAMURAI analysis gives compelling evidence for the role of diabatic processes in the structural evolution of Sinlaku during ET. To quantify this evolution by diagnosing the diabatic heating, analyzing the temporal evolution of PV and modeling the observed structure is an interesting perspective for further studies.

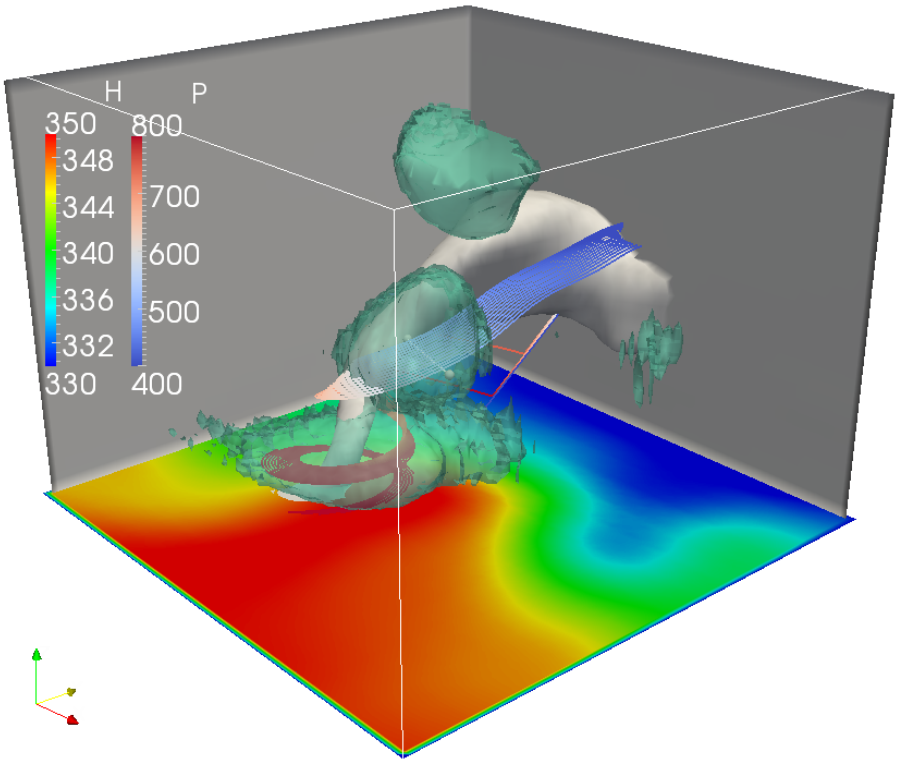

Figure 6.17: 3D view of SAMURAI analysis from southeast. Contour of horizontal wind speed (grey 5 $m\ s^{-1}$) indicating the typhoon, contour of PV (dark green 3.5 PVU) indicating the PV tower, moist static energy (H) shaded, streamlines pass the white line in the midtropospheric PV maximum to the east of "Sinlaku". Streamlines coloured by pressure (P).

6.7 Quasigeostrophic forcing

By calculating the QG-forcing (Hoskins et al., 1978) the role of synoptic-scale forcing of ascent in the frontal region and in the deep convection is evaluated. Moreover, the QG-forcing helps to investigate the origin of the thermal direct circulation seen along the developing warm front. Applying Hoskins' theory in this case, it is assumed that the pressure-based vertical coordinate, z, is identical with physical height in the troposphere and the Coriolis parameter is constant. In the SAMURAI analysis considerably more wind observations (radar, dropsondes, AMVs) than pressure observations (dropsondes) are included, so that the confidence in the wind field is a lot stronger than in the pressure field. Thus the geostrophic wind needed for the QG-forcing calculation is approximated by the total wind field. As a third simplification diabatic cooling is omitted. As equation (6) in Hoskins et al. (1978) shows, with these assumptions vertical velocity is forced by the divergence of the **Q**-vector defined as

$$\mathbf{Q} = \left[-\gamma \left(\frac{\partial \mathbf{V}}{\partial x} \cdot \nabla \Theta \right), -\gamma \left(\frac{\partial \mathbf{V}}{\partial y} \cdot \nabla \Theta \right) \right] \tag{6.2}$$

with $\gamma = \frac{R}{p_0}\left(\frac{p_0}{p}\right)^{c_v/c_p}$. In the equations above Θ is the potential temperature, $\mathbf{V}$ the horizontal wind vector, p_0 a standard value of pressure, p the pressure, R the universal gas constant, c_v the specific heat at constant volume and c_p the specific heat at constant pressure.

Divergence of the **Q**-vector leads to descent whereas convergence of the **Q**-vector leads to ascent. To simplify the interpretation of the **Q**-vector this vector can be split into components parallel (Q_s) and perpendicular (Q_n) to the isentropes. As a result Q_n, describes changes of the absolute value of temperature gradient and Q_s describes changes of the direction of the temperature gradient. Therefore the interpretation of the **Q**-vector with respect to the development of the temperature field is equivalent to the components of frontogenesis F_n and F_s.

At 1 km height there is a marked dipole of quasigeostrophic forcing nearly parallel to the baroclinic zone (Fig. 6.18(a)), with divergence of **Q** (forcing for descent) to the north and convergence of **Q** to the south. This **Q**-vector dipole pattern is typical for a frontogenetical process and indicates forcing of a thermally direct circulation across the front. The maximum of **Q**-vector convergence is located between 100 km and 140 km E, and 60 km to 100 km N and thus collocated with the deep convective region. This indicates that the QG-forcing of vertical motion led to forced ascent and triggered the deep convective development. As the **Q**-vectors are mostly perpendicular to the isentropes, the quasigeostrophic vertical motion is primarily caused by a change of the absolute value of the temperature gradient, i. e. by scalar frontogenesis. The strongest **Q** convergence in the deep convective region is the result of a change of the absolute value of the temperature gradient, respectively Q_n (Fig. 6.18(b)). This indicates that the convergence along the warm frontal zone is more important for the quasigeostrophic forcing than the deformation of the temperature field by the vorticity of the cyclone (Q_s).

The low level structure of the **Q**-vector convergence indicates furthermore an important influence on the temperature field. The Q_s pattern indicates a strengthening of the amplitude of the thermal wave (arching of the isotherms). The Q_n pattern on the other hand indicates a strengthening of the temperature gradient in this region. In the case of a midlatitude low this structure would indicate a deepening of the low in the following hours/days. However, Sinlaku did not strengthen in the following days. The quasigeostrophic positive forcing exists to heights of about 4 km and the quasigeostrophic negative forcing to heights of 5 km along 125 km E (Fig. 6.18(d)). The quasi dipole structure of **Q**-vector divergence is northward sloped, nearly parallel to the isentropes. The evaluation of the Q_n and Q_s up to 5 km shows that the quasigeostrophic vertical motion is primarily the result of Q_n convergence along the warm frontal zone.

The **Q** vector divergence does not coincide with the downward motion derived from the SAMURAI analysis. A reason for this is, that the downward motion in the SAMURAI analysis is primarily caused by evaporation and strong precipitation in the stratiform precipitation region. These effects are not represented by the divergence of the **Q** vector of course, due to the assumptions and simplifications described above.

Finally, the **Q** vector pattern indicates that Sinlaku is no longer just a tropical cyclone but a cyclone with noticeable midlatitude features. Especially the structure of Q_n and Q_s show midlatitude features which suggest a strengthening of the arching of the isentropes, respectively the thermal wave.

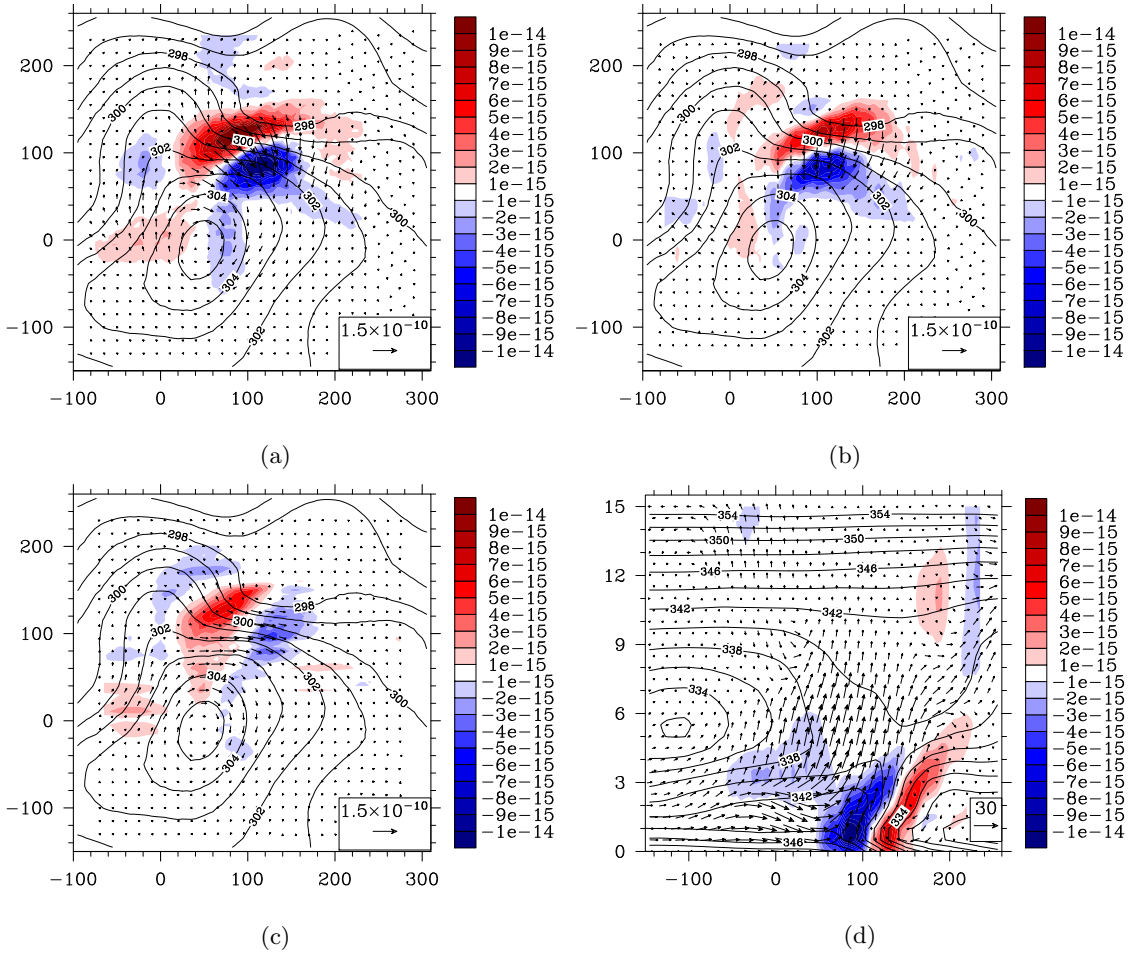

Figure 6.18: Horizontal cross sections of vectors and divergence of **Q** $[m\ (kg \cdot s)^{-1}]$ (a), Q_n (b) and Q_s (c). Contours are potential temperature [K]. Vertical cross section of divergence of **Q** along 125 km E (d). Vectors are wind in cross section (v and w) $[m\ s^{-1}]$. w is multiplied by ten. Contours are moist static energy $[kJ\ kg^{-1}]$.

The quasigeostrophic forcing in the cold frontal region shows a weak forcing for downward motion and not for upward motion (Fig. 6.18 (a)). This weak forcing indicates a weaker frontogenesis in the cold frontal region than in the warm frontal region, in agreement with the ECMWF operational analysis (section 3.1). The weak downward motion coincides additionally with downward motion represented by trajectory calculations in section 3.1. The quasigeostrophic forcing for downward motion reaches its maximum intensity at 2 km height to the north of the dry intrusion. A dipole structure of quasigeostrophic motion along the cold front cannot be seen, so that a secondary circulation does not exist in this case. In addition to the QG-forcing in the frontal region, there is a region of elevated QG-forcing between 2 km and 6 km height and between 60 km S and 60 km N (Fig. 6.18 (d)). This convergence is located below strong upward motion and above a rather horizontal

flow. Thus **Q** convergence might have triggered vertical motion as well. At 4 km height, the **Q**-convergence is located at the most eastern part of the dry intrusion in the region of an enhanced temperature gradient (not shown). This suggests that the enhanced temperature gradient, associated with the dry intrusion, forces quasigeostrophic motion in the mid-troposphere. Indeed, the forcing is almost one order of magnitude smaller than the forcing along the warm front. As the magnitude of the Q_s vector convergence is similar to the magnitude of the Q_n vector convergence both mechanisms play an important role in this case.

6.8 Discussion

The SAMURAI analysis shows deep convection and stratiform precipitation as part of a MCS during Sinlaku's ET. A warm- and cold frontal zone, and a dry intrusion have been identified. Sinlaku's environment was characterized by a warm-moist southerly flow to the east and a cold-dry easterly flow to the north. These two flows converged along the baroclinic zone which extended eastwards from the cyclone center. The convergence along the baroclinic zone led to a deformation of the temperature field and as a consequence to warm frontogenesis. Furthermore, the cyclone's circulation was conducive to the development of a frontal wave on the baroclinic zone. This strengthened the frontogenesis as well. The calculation of the **Q** vector divergence suggests that the frontogenesis forced vertical motion to the south of the baroclinic zone. The low level maximum of the **Q** vector convergence was collocated with the deep convection of the mesoscale convective system. This suggests, that the quasigeostrophic forcing had a positive influence on the convective development in a conditionally instable environment. Another possibility for the deep convective development is a strong low level convergence due to the confluence of the easterly and southerly flow. This convergence forced ascent and therefore lifted parcels in a potential instable environment above the level of free convection. This resulted in a strong positive buoyancy and enabled the deep convective development.
Questionable is still the influence of the dry intrusion on the deep convection. Satellite images showed the dry intrusion wrapping around the cyclone into the region where the deep convection developed a few hours later. The derived analysis shows remnants of the dry intrusion to the southwest of the circulation center. It can be assumed, that the dry intrusion enhanced the potential instability before the deep convective development due to the advection of cold and dry air above the warm moist boundary layer. The deep convection itself neutralized the stratification due to latent heat release in the mid-troposphere afterwards and potentially caused the dissipation of the dry intrusion in this area. The latent heat in the mid-troposphere was advected furthermore around the cyclone's center to the north of the storm. This caused a stabilization of the stratification in this region. As a consequence, the convective activity was reduced in this area, so that re-development of a symmetric convection around the cyclone center could not be expected.
The low level PV maximum was almost collocated with the cyclone's circulation center. One can assume that this maximum was a remnant structure of the cyclones PV tower. Latent heat release enhanced PV in the mid-troposphere and caused a local maximum

of PV between 5 km to 7 km height. This PV maximum caused a deformation of the wind field. Noticeable is the transport of this midtropospheric PV in northerly directions towards the midlatitude jet. The verification and influence of this outflow on the environment and the midlatitude jet could be investigated in following numerical studies.
The combination of the analyzed structure leads to the image of cyclone that shows tropical as well as extratropical structures. The tropical structures such as a potential instability, a moist boundary layer and deep convection up to 15 km height can be found to the east of the cyclone and to the south of the baroclinic zone. The extratropical structures such as a cold easterly flow, a warm front including a secondary circulation and a cold front can be found to the northeast and west. The development of the deep convection and the stratiform precipitation region is the result of an interaction between the midlatitude flow and the tropical flow. At this point of time the cyclone can neither be labeled as a tropical system nor as an extratropical system. It is rather a cyclone centered on the baroclinic zone influencing the midlatitudes and being influenced by the midlatitudes as well. As a consequence, using Klein's et al. (2000) definition of ET, Sinlaku is at this time in the transformation stage.

7. Quality control and comparison between ECMWF and SAMURAI

The overall goal of this study and measurements during T-PARC is to obtain a more realistic image of the structure of a transitioning typhoon than it is provided by numerical weather prediction systems. After having analyzed the structure in detail one can pose the question concerning the attainment of this ambitious goal. Global weather prediction systems are able to resolve the large- and mesoscale patterns of ET, but do not represent the convective small scale structures. Therefore, a quality control is accomplished to give a summary of the improvements and differences between the ECMWF analysis and the SAMURAI analysis.

A statistical comparison of the background at the measurement locations versus the observations is shown in figure 7.1 (a). To avoid the domination of the statistics by any particular measurement all variables were transformed to units having similar magnitudes. The kinematic variables have the unit $m\ s^{-1}$, water vapour content is given in $g\ kg^{-1}$, moist static energy perturbation in $kJ\ kg^{-1}$ and density in $10\ g\ m^{-3}$. A linear fit through all the observational points shows a slope of ≈ 0.65. As the slope is well below 1 the ECMWF underestimates multiple variables in this convective region. This underestimation can be seen also in the histogram of differences between the background and the observations (Fig. 7.1 (c)). For example, about 11% of the show a background to observation difference between -1 and -2, whereas only 7% show a difference between 1 and 2. In optimum the differences should exhibit a normal distribution centered on the zero line.

A significant better correlation can be realized in a statistical comparison of the SAMURAI analysis at the measurement locations and the observations. Using the same configuration, the linear fit in figure 7.1 (b) has a slope of ≈ 0.96 and a very small intercept of ≈ 0.04. Furthermore, the spread of the difference between the observations and the analysis is nearly uniform at different magnitudes. The reason for the spread from the center line are the background, smoothing parameters and observation errors. As a consequence, some quantities such as vertical motion are not as strong in the SAMURAI analysis as in the observational data. The distribution of the differences shows an approximately normal

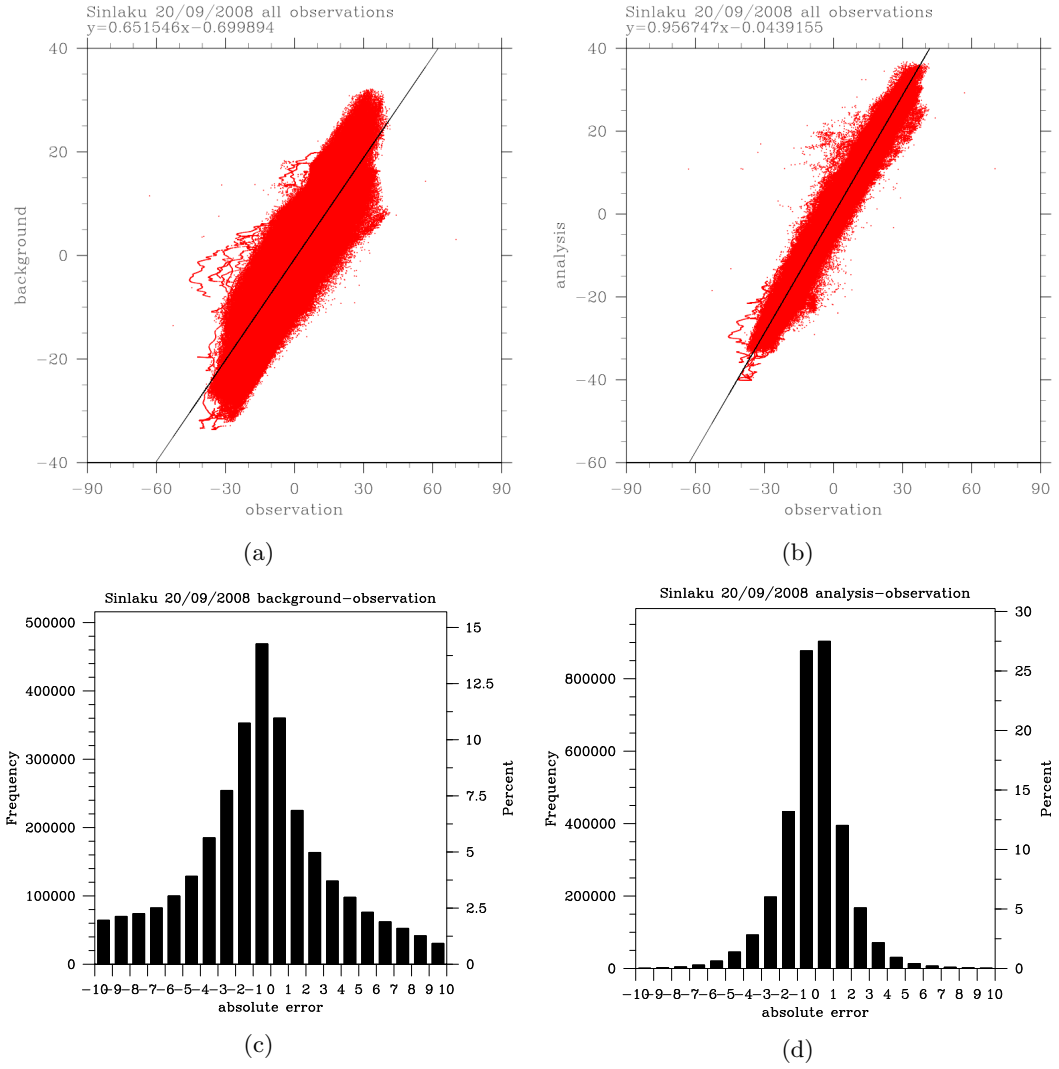

Figure 7.1: Background (ECMWF) versus observations and analysis (SAMURAI) versus observations for Typhoon Sinlaku on 20th September. (a) and (c): scatter plot of all observations; (b) and (d): histogram of differences between background and observation, respectively analysis and observation. Units of observational data are given in text.

distribution centered about zero. A slight underestimation can still be seen, but it is a lot smaller in comparison to the ECMWF. Furthermore, about 54% of the differences have an absolute error between ±1. Only 27% of the background data, i. e. ECMWF data, are located in this interval. Errors with magnitude greater than 9 vanished nearly completely. As a result, the statistics show that the SAMURAI analysis is much closer to the observations than the ECMWF analysis. Of course, this result is not surprising due to the 3D-VAR technique used in the SAMURAI analysis.

A validation of ECMWF and SAMURAI is possible in the lower troposphere using the dropsonde measurements. For a comparison, the observational data and analysis data were plotted in a skew-T diagram. To facilitate the comparison despite the different resolutions of the analyses, the ECMWF analysis was interpolated on 5 km grid as well. Afterwards the data of the nearest gridpoints to the dropsonde location were compared.

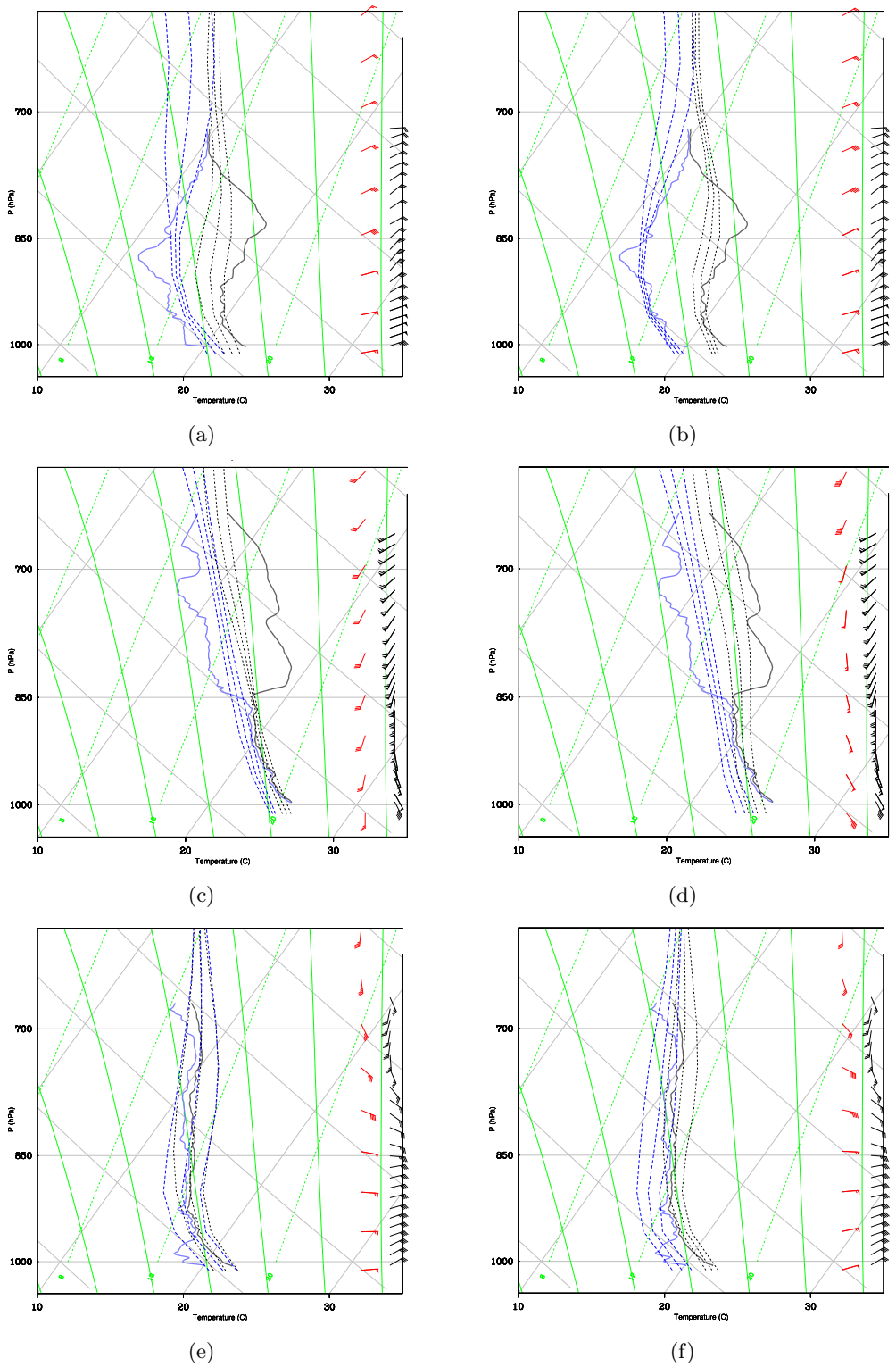

(a) (b) (c) (d) (e) (f)

Figure 7.2: Dropsonde measurements from C-130 on 20 September, 05:52 UTC in comparison to ECMWF analysis (a) and SAMURAI analysis (b). Dropsonde measurements from P-3 on 20 September, 06:28 UTC and 06:52 UTC in comparison to ECMWF analysis (c, e) and to SAMURAI analysis (d, f). Dashed lines show SAMURAI analysis (blue=dew point, black=temperature); continuous lines are dropsonde measurements (blue=dew point, black=temperature). Red wind barbs from SAMURAI analysis, black wind barbs from dropsonde measurements. Wind is given in [kt].

As the dropsonde locations do not coincide with the gridpoints, especially given the drift of the dropsonde, the standard deviation in SAMURAI/ECMWF in a box around the observation is shown also. In the following only a few comparisons are described, that show considerable differences between SAMURAI and ECMWF. In this case, the representation of the warm frontal zone is of particular interest because the differences are largest here.
A dropsonde measurement to the south of the warm front (at 120 km E and 20 km N) exhibits a strong southerly to southeasterly flow of about 70 kt ($\approx 35\ m\ s^{-1}$) below 850 hPa (Fig. 7.2 (c, d)). The ECMWF analysis does not represent this strong flow. The wind maximum in the ECMWF analysis is in this layer about 30 kt ($\approx 15\ m\ s^{-1}$). Furthermore, the background data show a rather southerly flow without any easterly component. Above 850 hPa the wind shifts slightly westwards and has a strong westerly component above 700 hPa. These features are not well represented in the ECMWF analysis. The profile of temperature and humidity are represented quite well below 850 hPa but a rather dry layer above this level is not represented at all. The wind profile and strength is better represented in the SAMURAI output. Differences of 5 kt ($\approx 3\ m\ s^{-1}$) to 15 kt ($\approx 8\ m\ s^{-1}$) still exist. The southeasterly winds below 850 hPa are represented quite well in the SAMURAI output, whereas the shift to westerly winds above 850 hPa is too weak. The temperature and humidity profile above 850 hPa are improved but important features such as the inversion at 850 hPa are not represented. A reason for this is among others a too coarse vertical resolution of the analysis.
Further to the north (at 180 km E and 150 km N) another dropsonde was released by the NRL-P3 in the warm frontal region and in the deep convection (Fig. 7.2 (e, f)). The measurements show a strong easterly flow of about 40 kt ($\approx 20\ m\ s^{-1}$) below 800 hPa. Above this height the winds shift abruptly into southerly winds. The ECMWF analysis as well as the SAMURAI output resolve this wind profile. Small differences exist in the abrupt windshift and the strength of the easterly flow. This flow is overestimated by both of the analysis techniques by 15 kt ($\approx 8\ m\ s^{-1}$). Both analysis techniques represent the moist stratification near saturation quite well. The SAMURAI output is mostly a bit too dry in comparison to the dropsonde measurement.
An overestimation of the easterly winds by the SAMURAI analysis can be found to the northwest of Sinlaku (at 20 km W and 160 km N). In this case C-130 dropsonde measurements are compared to the analysis (Fig. 7.2 (a, b)). Below 900 hPa an easterly flow with winds of 50 kt ($\approx 25\ m\ s^{-1}$) was measured. The wind speed decreases abruptly with height and has its minimum of 20 kt ($\approx 10\ m\ s^{-1}$) between 800 hPa and 700 hPa. The strength of the low level easterly flow is overestimated by 5 kt to 10 kt. Especially the SAMURAI analysis does not resolve the decreasing wind speed with height. At 750 hPa a difference of 20 kt can be identified between the observations and the SAMURAI output. A reason for this overestimation is the vertical Gaussian distribution of the observational data in the SAMURAI analysis. As a consequence, observational data on one layer have an influence on the layer above and therefore increase the wind speed. The low level temperature and humidity is represented quite well by the SAMURAI analysis. In contrast, the observed dry layer below 700 hPa is not resolved very well by the ECMWF analysis.

These comparisons show that the SAMURAI analysis on the one hand overestimates the easterly winds and on the other hand resolves the southerly winds quite well. The temperature and wind profiles are not as exact as the observations are. A reason for this is a coarse vertical resolution of 0.5 km, a smoothing of the observational data by the ECMWF background fields and the vertical Gaussian distribution which smooths vertical gradients as well. Despite the weak overestimation of the easterly flow in comparison to the dropsonde measurements the SAMURAI output is assumed to be close to the true state of the atmosphere in the following. Further comparisons between the ECMWF analysis and the SAMURAI analysis are only presented below 5 km height because both, radar and dropsonde data, are available at these levels.

A comparison of the background field (ECMWF analysis) and the SAMURAI analysis shows an underestimation in the ECMWF analysis of the southerly flow to the east of the circulation center at 1 km (Fig. 7.3 (a, b)). Whereas a broad area with winds of more than 27 $m\ s^{-1}$ exists in the SAMURAI analysis to the east of the circulation center, winds in the ECMWF do not exceed 18 $m\ s^{-1}$. Although one might argue that an underestimation of about 9 $m\ s^{-1}$ is not worth to mention, over land this difference could have an important impact on damages or not. Furthermore, important dynamical quantities such as vertical wind shear and low level convergence with easterly winds to the north are wrongly represented. The result of this underestimation is on the one hand a too weak circulation around Sinlaku and on the other hand a weaker southerly advection of moist static energy. Another mentionable feature at low levels is the windshift along the baroclinic zone. The SAMURAI analysis shows a windshift from south to east over a distance of about 100 km. In the ECMWF the windshift is stronger and the wind shifts from south to east over a distance of 40 km. This strong windshift generates a strong convergence which has nearly the same order of magnitude as the convergence in the SAMURAI analysis. The main difference with respect to the convergence is its location. As the wind shifts further to the north in the ECMWF than in the SAMURAI analysis the maximum of the convergent zone in the ECMWF is located 40 km north and about 40 km east of the maximum convergence in the SAMURAI analysis (Fig. 7.3 (a, b)). The different locations of maximum low level convergence illustrate different locations of vertical motion and consequently different locations of the convective system. The comparison between satellite images and the flight track showed that the NRL P-3 circuited the deep convection (Fig. 5.2 (a)). As a result, the low level convergence derived by the SAMURAI analysis is more probable than the convergence in the ECMWF. However, the above mentioned displacement of 40 km to the north and 40 km to the east is still quite good for a global model. The difference, with respect to the magnitude of the divergence, is greater to the north of the baroclinic zone. In the ECMWF analysis the divergence does not exceed $2 \cdot 10^{-4} s^{-1}$ at 1 km height. Instead, the SAMURAI output shows a divergence of $3 \cdot 10^{-4} s^{-1}$. The reason for this difference is a weaker downward motion north of the baroclinic zone at low levels. The downward motion in the ECMWF analysis is underestimated because it is a hydrostatic weather prediction system, has a horizontal resolution of 25 km and as a consequence does not resolve downdrafts with the magnitude of 1 $m\ s^{-1}$. These downdrafts are resolved by the SAMURAI analysis and they induced a diffluent flow at the lowest levels.

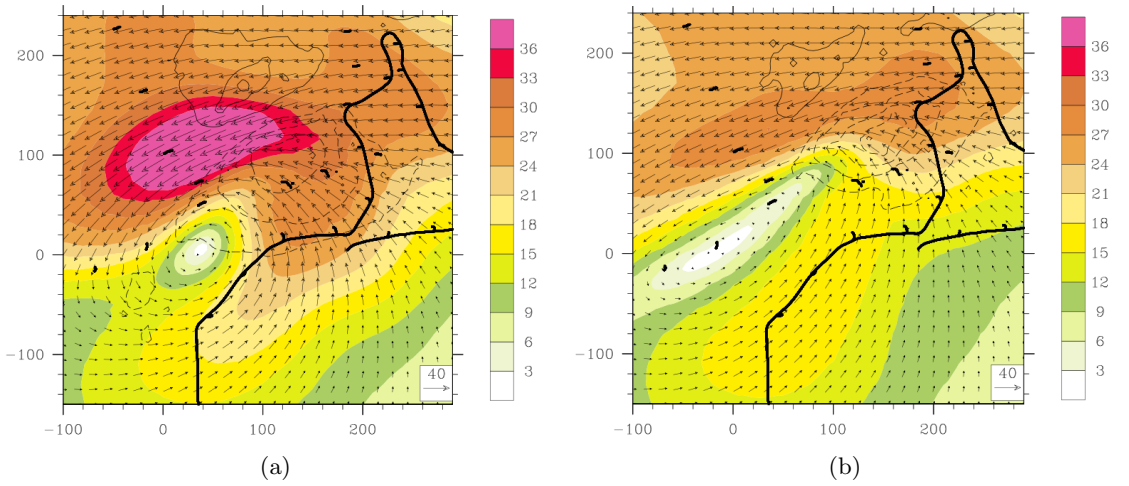

Figure 7.3: Wind speed [$m\ s^{-1}$] (shaded), divergence [$10^{-5}s^{-1}$] (contours with interval of $10^{-4}s^{-1}$, negative values are dashed), (a): output from SAMURAI, (b): output from ECMWF at 1 km, black dots denote positions of dropsondes released from the P-3 and C-130, black line represents flight track of P-3.

In the previous chapter the structure of ascent in the deep convection and at the warm frontal zone was described. Two branches of ascent were identified (Fig. 7.4 (a)). One branch ascends along the moist isentropes of the northward tilted baroclinic zone, the second branch consists of nearly upright ascent within the deep convection. A comparison between ECMWF and SAMURAI concerning the representation of those two branches shows a noticeable difference. The ECMWF only represents the branch ascending along the moist isentropes of the northward tilted baroclinic zone (Fig. 7.4 (b)). The branch of nearly upright ascent in the deep convection is not represented at all.

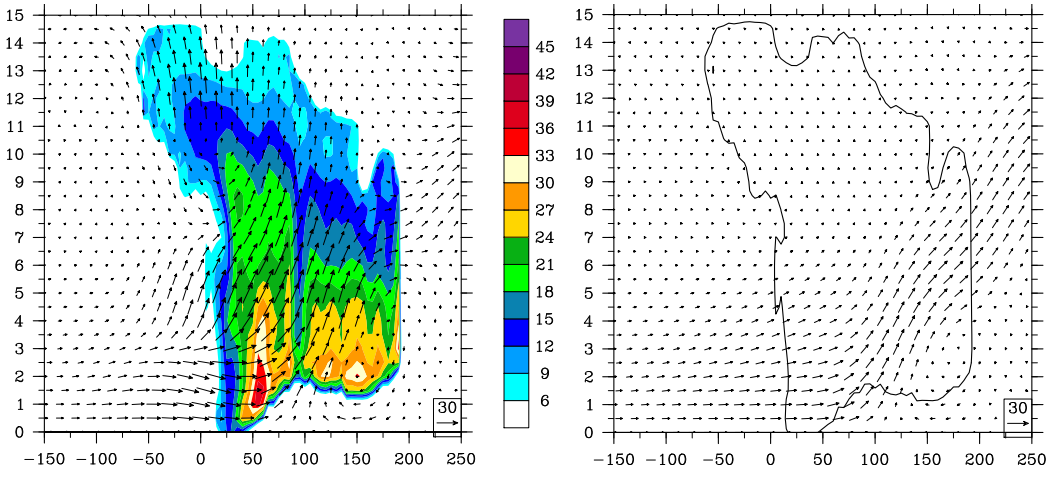

Figure 7.4: Reflectivity (shaded) [dBZ] and wind vectors [$m\ s^{-1}$] in the plane of the cross section along 125 km E. (a) output from SAMURAI, (b) output from ECMWF. Black contour in (b) is only given for orientation purpose and indicates the 5 dBZ contour from SAMURAI.

As the ascent along the baroclinic zone is a rather meso- to large-scale feature, the ECMWF is able to resolve this structure. To ensure that the convection was not present in the ECMWF analysis but at a different location, cross sections were made throughout the whole SAMURAI analysis domain. No structures like those in the SAMURAI analysis were found.

The representation of the moist static energy at low levels is of big interest, as it caused a significant destabilization and therefore favoured the conditions for a deep convective development. The moist static energy field between the ECMWF analysis and the SAMURAI analysis exhibits small differences. The moist southerly flow to the east does not differ noticeably, so that the low level conditions for an unstable environment are given accurately in the ECMWF analysis (Fig. 7.5 (a, b)). The SAMURAI analysis shows cold and dry air to the west of the circulation center between 80 km S and 0 km, whereas the ECMWF analysis shows higher values of moist static energy in this region. Therefore, the amplitude of the thermal wave is slightly greater in the ECMWF analysis than in the SAMURAI output.

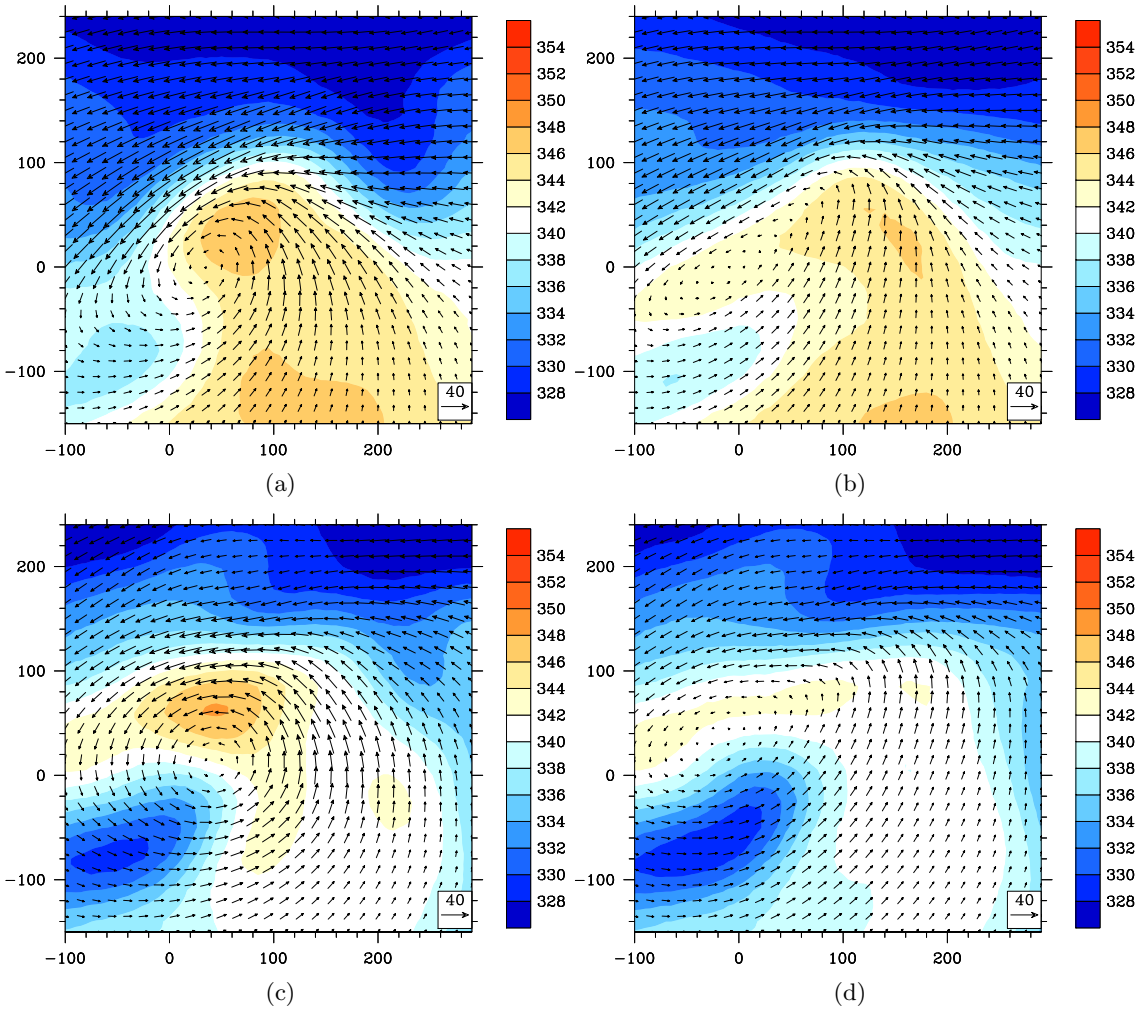

Figure 7.5: Moist static energy $[kJ\ kg^{-1}]$ (shaded), horizontal winds $[m\ s^{-1}]$, (a) and (c): output from SAMURAI at 0.5 km and 2 km, (b) and (d): output from ECMWF at 0.5 km and 2 km.

A remarkable difference in the moist static energy field exists at 2 km (Fig. 7.5 (c, d)). To the north of the circulation center, which is a lot more symmetric in the SAMURAI analysis than in the ECMWF at this height, the moist static energy exceeds 348 $kJ\ kg^{-1}$. In the ECMWF analysis the moist static energy exceeds only 342 $kJ\ kg^{-1}$ in the same region. Furthermore, the horizontal advection from the east of Sinlaku to the north of the storm is not represented as well. As a consequence, the instability north of the circulation center is greater in the ECMWF than in the SAMURAI analysis. However, it is still remarkable that the ECMWF represents this small scale structure in moist static energy. The described difference between ECMWF and SAMURAI exists up to a height of about 5 km.

Similar to section 6.6, the PV will be used to evaluate asymmetries in Sinlaku's circulation. At 1 km height Sinlaku's circulation center is elongated from southwest to northeast (Fig. 7.6 (a)) in the ECMWF. The PV maximum is not collocated with the circulation center but rather with a region of maximum windshift in the warm frontal zone, close to the deep convection. In the SAMURAI analysis the PV exceeds 5 PVU over a much larger area than in the ECMWF analysis. Noticeable is furthermore the PV maximum to the east of the cyclone center. The ECMWF analysis showed on 20 September 00 UTC a weak circulation to the east of Sinlaku (Fig. 3.7 (b)). As a consequence, the PV maximum in figure 7.6 (a) could be a remnant of this circulation.

At 3 km height Sinlaku's circulation is more symmetric than at 1 km (Fig. 7.6 (b)). This increasing symmetry with height exists in the SAMURAI analysis as well. The PV is also more symmetric except for a west-east elongated structure along the warm front. This increasing symmetry with height indicates, that asymmetry at low levels (especially in the boundary layer) is the result of low level frontogenesis which decreases with height. Particular the reasons for decreasing cold frontogenesis with height to the southwest of the cyclone have been discussed in section 6.6. The west-east elongated PV structure along the wind shift of the warm front is most probably the result of latent heat release in this region. As the ECMWF shows upward motion along the baroclinic zone (Fig. 7.6 (d)), it can be assumed, that this upward motion caused latent heat release in a convective area and therefore the production of PV. At 6 km the PV structures of the SAMURAI output and the ECMWF analysis are completely different. The SAMURAI analysis shows a maximum collocated with the deep convection. Already the structure of vertical motion in the ECMWF analysis showed, that the global model did not represent the deep convection according to the wind field. As a consequence, the ECMWF does not represent the production of latent heat release and accordingly no production of PV. Vertical cross section show the differences in PV very impressively. In the SAMURAI analysis, a PV tower extends to the upper troposphere in the region of deep convection. In the ECMWF instead, PV of more than 2 PVU already vanishes at 7 km (Fig. 7.6 (d)). This extraordinary low PV structure in the ECMWF potentially has a significant influence on the cyclone's structure. In section 6.6 it was argued, that the PV maximum in the mid-troposphere (seen in SAMURAI) leads to a significant windshift and therefore increases asymmetric structures. The ECMWF does not represent the development of these asymmetric structures at all. This wrong, respectively missing representation, might lead to wrong forecasts of

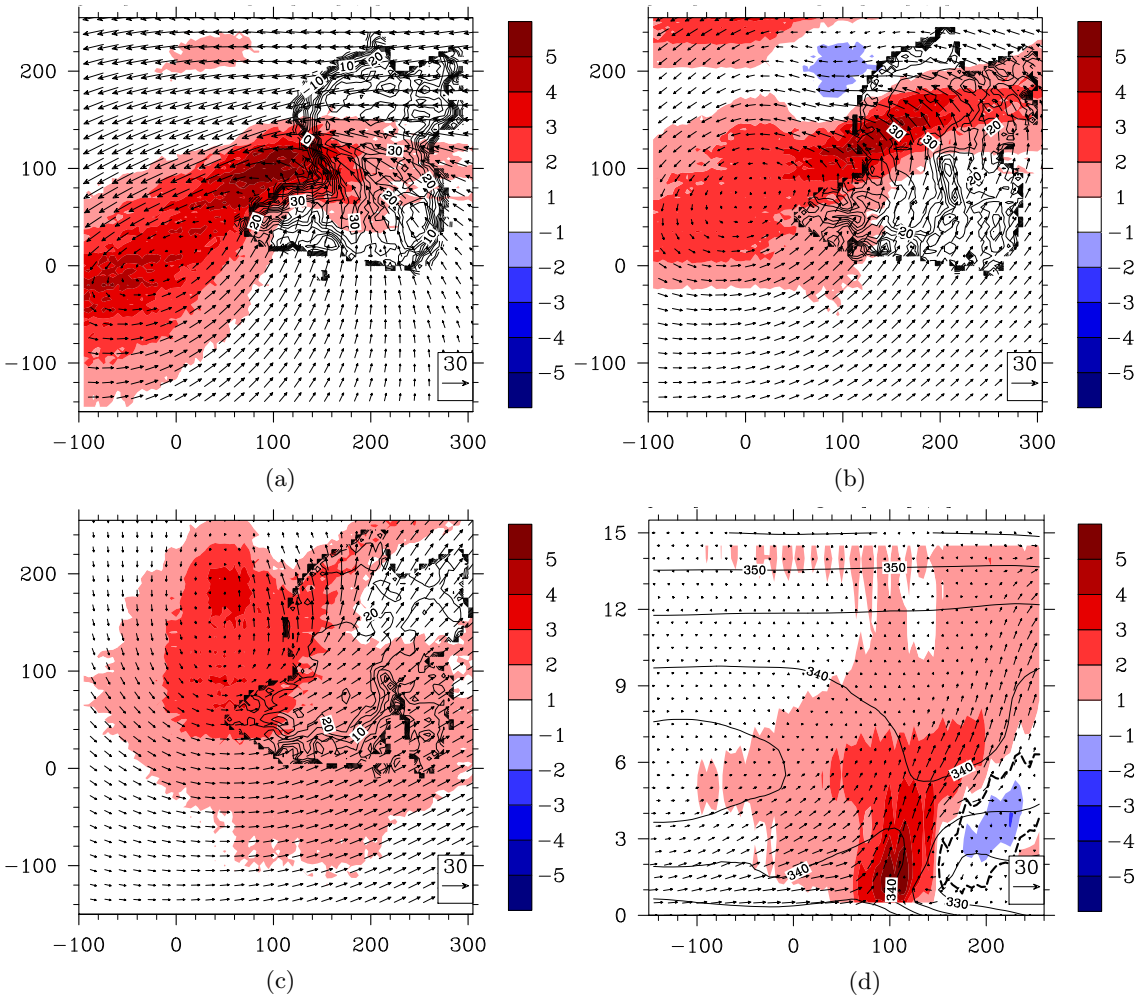

Figure 7.6: Potential vorticity [PVU] (shaded) and reflectivity [dBZ] at 1 km (a), 3 km (b) and 6 km (c) height. Potential vorticity (shaded) and wind parallel to cross section (v and w) [$m\ s^{-1}$] along 100 km E (d). Contours denote moist static energy [$kJ\ kg^{-1}$]. In (d) thick dashed line denotes 0.2 PVU. The saw-toothed structure can be attributed to the interpolation of ECMWF data on a 5 km grid.

the cyclone's development. The frontogenesis occurring during Sinlaku's ET is one of the most important aspects of this study.

Probably for the first time, observations in a transitioning typhoon have allowed the frontogenesis to be evaluated in detail. Using equation 3.2 after Keyser et al. (1988), the frontogenesis components F_n and F_s were calculated at 1 km from the SAMURAI analysis and from the background field (ECMWF) as in section 3.3. The splitting shows that the strong frontogenesis in the ECMWF and in SAMURAI results from both, F_n and F_s. The positive values of F_s indicate, that the change of direction of the temperature gradient is caused by cyclonic rotation (Fig. 7.7 (b)). A comparison with the PV structure at 1 km height (Fig. 7.6 (a)) shows that the maximum of F_s is collocated with the PV maximum at 100 km E and 100 km N. This suggests that the PV maximum not only deformed Sinlaku's circulation at low levels, but also increased the rotational component of frontogenesis. The F_n component of warm frontogenesis derived from the SAMURAI analysis is stronger over

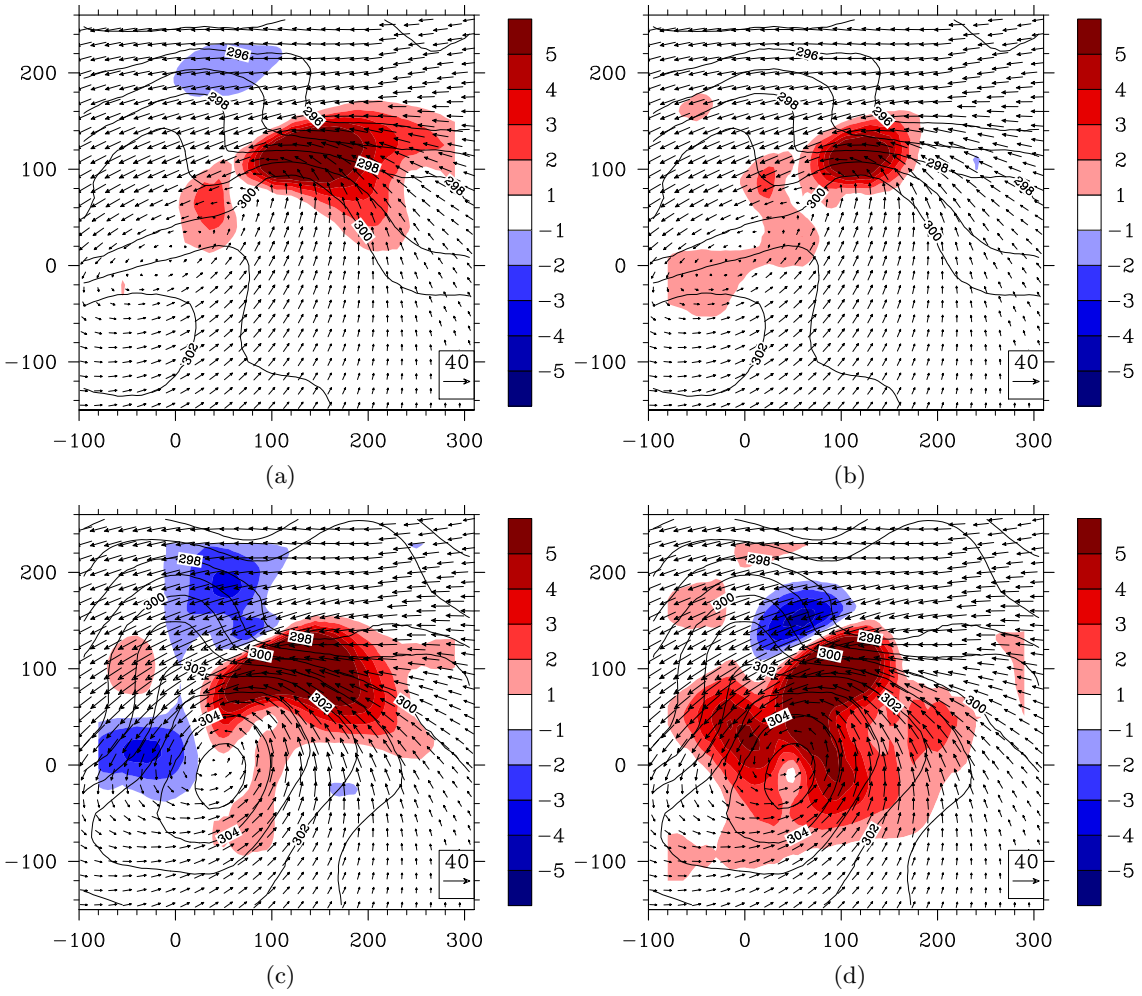

Figure 7.7: F_n shaded (a, c) and F_s shaded (b, d) from ECMWF (a, b) and SAMURAI (c, d) at 1 km. Black contours denote the potential temperature at 1 km.

a larger area than that derived from the ECMWF analysis (Fig. 7.7 (a, c)). Maximum F_n is located to the northeast of the cyclone center and is a result of convergence along the baroclinic zone. Cold frontogenesis can be detected as well, to the west and north of the cyclone. The region of cold frontogenesis to the west along 0 km N coincides with the region labeled as cold frontal zone in section 6.4. The F_s derived from the SAMURAI output shows a completely different and much stronger structure in comparison to the ECMWF. The region of positive F_s is much larger than that in the ECMWF. This suggests that the influence of the cyclone on the change of direction of the temperature gradient is stronger than represented by the ECMWF. It indicates, furthermore, an increasing amplitude of the thermal wave which coincides with the conclusions made from **Q** vector calculations. As already mentioned in section 6.6, thinking of a midlatitude system, the amplification of the thermal wave would imply a deepening of the cyclone. If the cyclone to the northeast of Sinlaku deteriorated the conditions for a development of a thermal wave, could be investigated in future studies. However, the ECMWF showed strong frontogenesis on 20 September 06 UTC, but the actual frontogenesis derived from observations was a lot stronger at this time.

A discussion of the reasons for this underestimation by the ECMWF and an evaluation of its influence on the forecasts could be accomplished in further studies. The main differences between the ECMWF analysis are evident in the dynamic variables whereas the thermodynamic structure such as the moist static energy is represented quite well. Due to a coarse horizontal resolution the ECMWF does not resolve the deep convection to the south of the baroclinic zone. As a result a mid-level PV maximum does not exist due to the absence of latent heat release. This mid-level positive PV anomaly had probably an impact on Sinlaku's development. To investigate the influence of the PV structure on the TC's development would be a challenging task for future studies. Furthermore, the impact of the underestimation of the southerly flow to the east of Sinlaku could be investigated. A too weak southerly flow reduces the advection of warm moist air and results in weaker convergence with the easterly flow to the north of the baroclinic zone. As the convergence associated with frontogenesis triggered probably the convection, an inaccurate representation could underestimate the actual convective development.

8. Conclusion

In this study the extratropical transition of Typhoon "Sinlaku" has been described on multiple scales by the use of model- and observational data. At first the ECMWF analysis was used to describe "Sinlaku's" environment during its extratropical transition. The midlatitude flow during the ET was nearly zonally orientated. As a consequence upper level quasigeostrophic forcing, induced by a midlatitude trough, was not present. Therefore, "Sinlaku" did not enter favorable conditions for an extratropical development. The calculation of frontogenesis showed signatures typical for ET such as a developing cold front in the southwestern quadrant of the typhoon and warm frontogenesis in the northeastern quadrant. The warm frontogenesis increased remarkably during the ET which coincides with the results of previous studies. According to the ECMWF analysis the warm frontogenesis reached its peak on 20 September 06 UTC. Around that time deep convection developed to the northeast of the cyclone center.
This deep convection and stratiform precipitation to the north of it were investigated by the research aircrafts C-130 and NRL P-3 as a part of the field campaign T-PARC. Using observational data from these research flights a three dimensional analysis was derived by applying the recently developed 3D-VAR data assimilation software tool SAMURAI. The analysis of the observational data showed tropical as well as extratropical features. These features have been described separately. Structural characteristics in the dynamics, thermodynamics and the reflectivity helped to label the main features as a deep convective system, a stratiform precipitation region, a warm front, a cold front and a dry intrusion. The combination and evaluation of the wind field, the moist static energy and the reflectivity helped to derive a conceptual model of the convective system that developed on that day. The comparison of the derived conceptual model with models of previous studies shows a large mesoscale convective complex. The conceptual model shows an in this case warm-moist southerly inflow below a midtropospheric layer of rather cold and dry air entering the region of deep convection. The deep convection itself developed on the warm frontal zone. It is determined by almost upright upward motion ending in a broad cirrus shield, that extends to the south of the system. North of the deep convection the

precipitation has a rather stratiform character. It is determined by vertical motion along the isentropes of a northward tilted warm front. Below this isentropic ascent, a northeasterly flow advects cold and dry air towards the deep convection. Descent determines the vertical motion in the cold and dry air. It is primarily caused by downdrafts and cooling of midtropospheric air by melting and evaporation of precipitation particles. The upward motion south of the warm front and downward motion to the north are part of a secondary circulation along the warm front.

To investigate this secondary, thermal direct circulation and its influence on the deep convection the divergence of the **Q**-vector was calculated. The calculation suggests that the divergence of the **Q**-vector favours the secondary circulation. Furthermore, divergence of the **Q**-vector leads to forced ascent in the deep convective region and triggers probably its development. Moreover, the divergence of the **Q**-vector components suggest an amplification of the thermal wave resulting from the interaction between "Sinlaku" and the baroclinic zone.

The potential vorticity maximum derived from the SAMURAI output was collocated at low levels with "Sinlaku's" remnant circulation center. With height the circulation center and the potential vorticity maximum departed from each other. In the mid troposphere the maximum of potential vorticity was collocated with the center of the deep convection and not with the circulation center. This indicates that the convection produced potential vorticity by latent heat release. The strong production of potential vorticity led to a deformation of Sinlaku's wind field and presumably accelerated the typhoon's decay. Another region where latent heat release might have increased the potential vorticity is along the warm front in the stratiform precipitation region. Maxima of potential vorticity were lifted from the surface which indicated a latent heat release in the moist southerly flow ascending along the moist isentropes of the northward tilted baroclinic zone.

The comparison between the SAMURAI analysis and the ECMWF analysis shows remarkable differences. Big differences arise in the strength of the warm-moist southerly and dry cold easterly flow. The strength of both of them is underestimated although the location is represented quite well. Strong, upright vertical motion in the deep convective region is not represented in the ECMWF analysis. The ascent along the northward tilted moist isentropes of the baroclinic zone is represented by the ECMWF as this is a meso- to large scale feature. As a result the ECMWF is able to represent meso- to large scale features of extratropical transition and not small scale, but important features such as strong convection. The absence of the deep convection leads to an underestimation of latent heat release and accordingly to very weak production of potential vorticity. The production of potential vorticity in the mid-troposphere is completely underestimated. The resulting deformation of the wind field fails.

In future studies the influence of an inaccurate representation of the system on weather prediction could be investigated. Furthermore, it would be a big challenge to run simulations with a high spatial resolution, which are able to represent the main observed structures. As the SAMURAI output is on gridpoints it could be worth a try to insert the derived thermodynamical and dynamical fields into a high resolution numerical weather prediction system. Moreover, the influence of the cyclone's circulation on the convective development

could be investigated also. Finally, several research flights have been accomplished during the ET of typhoon “Sinlaku”. To run SAMURAI analysis’ with the same configurations on each of the collected data sets and compare those would result in detailed insights into the different phases of extratropical transition.

Bibliography

Ahrens, C. D.: *Essentials of Meteorology: An Invitation to the Atmosphere.* Brooks/Cole, Cengage Learning, 229 pp., **6**, 2012.

Bader, M. J., G. S. Forbes J. D. Grant R. B. E. Lilley and A. J. Waters: *Images in Weather Forecasting: A Practical Guide for Interpreting Satellite and Radar Imagery.* Cambridge University Press, 499 pp., 1995.

Bell, M. M.: *Air-Sea enthalpy and momentum exchange at major hurricane wind speeds.* Dissertation at Naval Post Graduate School, Monterey, 147 pp., 2010.

Bell, M. M., M. T. Montgomery and K. E. Emanuel: *Air-sea enthalpy and momentum exchange at major hurricane wind speeds observed during CBLAST.* J. Atmos. Sci., submitted, 2012.

Biggerstaff, M. J. and R. A. Houze: *Kinematic and Precipitation Structure of the 10-11 June 1985 Squall Line.* Mon. Wea. Rev., **119**:3034–3065, 1991.

Bryan, G. and J. M. Fritsch: *Moist absolute instability: The sixth stability state.* Bull. Amer. Soc., **81**:1207–1230, 2000.

Davis, C., C. Snyder and A. C. Didlake Jr.: *A Vortex-Based Perspective of Eastern Pacific Tropical Cyclone Formation.* Mon. Wea. Rev., **136**:2461–2477, 2008.

Deveson, A. C. L., K. A. Browning and T. D. Hewson: *A classification of FASTEX cyclones using a height-attributable quasi-geostrophic vertical-motion diagnostic.* Q. J. R. Meteorol. Soc., **128**:93–117, 2002.

Emanuel, K.: *Tropical Cyclones.* Annu. Rev. Earth Plant. Sci., **31**:75–106, 2003.

Evans, J. L. and R. E. Hart: *Objective Indicators of the Life Cycle Evolution of Extratropical Transition for Atlantic Tropical Cyclones.* Mon. Wea. Rev., **131**:909–925, 2003.

Evans, C. and Hart, R.E.: *Analysis of the wind field evolution associated with the extratropical transition of Bonnie (1998).* Mon. Wea. Rev., **136**:2047–2065, 2008.

Foley, G. R. and B. N. Hanstrum: *The capture of tropical cyclones by cold fronts off the west coast of Australia.* Wea. Forecasting, **9**:577–592, 1994.

Frank, W. M. and E. A. Ritchie: *Effects of Environmental Flow upon Tropical Cyclone Structure.* Mon. Wea. Rev., **127**:2044–2061, 1999.

Frank, W. M. and E. A. Ritchie: *Effects of Vertical Shear on the Intensity and Structure of Numerically Simulated Hurricanes.* Mon. Wea. Rev., **129**:2249–2269, 2001.

Gamache, J. F.: *Evaluation of a fully three-dimensional variational Doppler analysis technique.* Preprints, 28th Conf. On Radar Meteorology, 9-13 Sept. 1997, Austin, AMS, 1997.

Gamache, J. F.: *Real-Time Dissemination of Hurricane Wind Fields Determined from Airborne Doppler Radar Data.* Final Report on JHT Project, 2008.

Grams, C. M.: *Quantification of the downstream impact of Extratropical Transition for Typhoon Jangmi and other case studies.* Dissertation at Karlsruhe Institute of Technology, 2011.

Harr, P. A. and R. L. Elsberry: *Extratopical Transition of Tropical Cyclones over the Western North Pacific. Part I: Evolution of Structural Characteristics during the Transition Process.* Mon. Wea. Rev., **128**:2613–2633, 2000.

Harr, P. A., R. L. Elsberry and T. F. Hogan: *Extratropical transition of tropical cyclones over the western North Pacific. Part II: The impact of midlatitude circulation characteristics.* Mon. Wea. Rev., **128**:2634–2653, 2000.

Hart, R. and J. L. Evans: *A Climatology of the Extratropical Transition of Atlantic Tropical Cyclones.* J. Climate, **14**:546–564, 2001.

Harr, P. A.: *Global Perspectives on Tropical Cyclones.* World Scientific Publishing Co. Pte. Ltd., **4**:149 pp., 2010.

Harr, P. A. and S. C. Jones: *The THORPEX PAcific Asian Regional Campaign (T-PARC) and Affiliated Programs.* THORPEX ICSC PDP Working Group, Fouth Meeting, Reading, 2011.

Hildebrand, P. H., C. A. Walther C. L. Frush J. Testud and F. Baudin: *The ELDORA/ASTRAIA Airborne Doppler Radar: Goals, Design, and First Field Tests.* Proceedings of the IEEE, **82**:762–780, 1994.

Hoskins, B. J., I. Draghici and H. C. Davies: *A new look at the ω-equation.* Quart. J. R. Met. Soc., **104**:31–38, 1978.

Houze, R. A.: *Stratiform precipitation in regions of convection: A meteorological paradox?* Bull. Amer. Soc., **78**:2179–2196, 1997.

Jones, S. C.: *The evolution of vortices in vertical shear. I: Initially barotropic vortices.* Q. J. R. Meteorol. Soc., **121**:821–851, 1995.

Jones, S. C.: *The evolution of vortices in vertical shear. II: Large-scale asymmetries.* Q. J. R. Meteorol. Soc., **126**:3137–3159, 2000.

Jones, S. C.: *The evolution of vortices in vertical shear. III: Baroclinic vortices.* Q. J. R. Meteorol. Soc., **126**:3161–3185, 2000.

Jones, S. C., and Coauthors: *The Extratropical Transition of Tropical Cyclones: Forecast Challenges, Current Understanding, and Future Directions.* Wea. Forecasting, **18**:1052–1092, 2003.

Kalnay, E.: *Atmospheric Modeling, Data Assimilation and Predictability.* Cambrige University Press, **1**:136–180, 2003.

Keyser, D., M. J. Reeder and R. J. Reed: *A Generalization of Petterssen's Frontogenesis Function and Its Relation to the Forcing of Vertical Motion.* Mon. Wea. Rev., **116**:762–780, 1988.

Kitabake, N.: *Extratropical transformation of Typhoon Vicki (9807): Structural change and the role of upper-tropospheric disturbances.* J. Meteor. Soc. Japan, **80**:229–247, 2002.

Klein, P. M., P. A. Harr and R. L. Elsberry: *Extratropical transition of western North Pacific tropical cyclones: An overview and conceptual model of the transformation stage.* Wea. Forecasting, **15**:373–395, 2000.

Klein, P. M., P. A. Harr and R. L. Elsberry: *Extratropical transition of western North Pacific tropical cyclones: Midlatitude and tropical cyclone contributions to reintensification.* Mon. Wea. Rev., **130**:2240–2259, 2002.

Lagouvardos, K., Y. Lemaitre and G. Scialom: *Importance of diabatic processes on ageostrophic circulations observed during the Fronts 1987 experiment.* Q. J. R. Meteorol. Soc., **119**:1321–1345, 1993.

Lorenc, A. C.: *Analysis methods for numerical weather prediction.* Q. J. R. Meteorol. Soc., **112**:1177–1194, 1986.

Maddox, R. A.: *Mesoscale convective complexes.* Bull. Amer. Meteor. Soc., **61**:1374–1387, 1980.

Martin, J. E.: *Quasigeostrophic Forcing of Ascent in the Occluded Sector of Cyclones and Trowal Airstream.* Mon. Wea. Rev., **127**:70–88, 1999.

Mohr, C. G., L. J. Miller R. L. Vaughan and H. W. Frank: *On the merger of mesoscale data sets into a common Cartesian format for efficient and systematic analysis.* J. Atmos. Oceanic Technol., **3**:143–161, 1986.

Moncrieff, M. W.: *Organized Convective Systems: Archetypal Dynamical Models, Mass and Momentum Flux Theory, and Parametrization.* Q. J. R. Meteorol. Soc., **118**:819–850, 1992.

Ooyama, K. V.: *The Cubic-Spline Transform Method: Basic Definitions and Tests in a 1D Single Domain.* Mon. Wea. Rev., **130**:2392–2415, 2002.

Pettersen, S. and S. J. Smebye: *On the development of extratropical cyclones.* Q. J. R. Meteorol. Soc., **97**:457–482, 1971.

Pomroy, H. and A. J. Thorpe: *The Evolution and Dynamical Role of Reduced Upper-Tropospheric Potential Vorticity in Intensive Observing Period One of FASTEX.* Mon. Wea. Rev., **128**:1817–1834, 2000.

Reasor, P. D., M. T. Montgomery and L. D. Grasso: *A New Look at the Problem of Tropical Cyclones in Vertical Shear Flow: Vortex Resiliency.* J. of Atmos. Sciences, **61**:3–22, 2004.

Riehl, H.: *A model for hurricane formation.* J. Appl. Phys., **21**:917–925, 1950.

Sanabia, E. R.: *The re-intensification of Typhoon Sinlaku (2008).* Dissertation at Naval Post Graduate School, Monterey, 2010.

Sauvageot, H.: *Radar Meteorology.* Artech. House, Boston, 1992.

Shimazu, Y.: *Classification of precipitation systems in mature and early weakening stages of typhoons around Japan.* J. Meteor. Soc. Japan, **76**:437–445, 1998.

Testud, J., P. H. Hildebrand and W. C. Lee: *A Procedure to Correct Airborne Doppler Radar Data for Navigation Errors Using the Echo Returned from the Earth's Surface.* J. Atmos. Oceanic Technol., **12**:800–820, 1995.

Thorpe, A. J. and K. A. Emanuel: *Frontogenesis in the presence of small stability to slantwise convection.* J. Atmos. Sci., **42**:1809–1824, 1985.

Thorncroft, C. and S. C. Jones: *The Extratropical Transitions of Hurricanes Felix and Iris in 1995.* Mon. Wea. Rev., **128**:947–972, 2000.

Vandenberghe, F. and Y. H. Kuo: *Introduction to the MM5 3D-VAR data assimilation system: Theoretical basis.* NCAR/MMM documents, 1999.

Velden, C. S.: *Winds derived from geostationary satellite moisture channel observations: Applications and impact on numerical weather prediction.* Meteorology and Atmospheric Physics, **60**:37–46, 1996.

Wang, Y. and G. Holland: *Tropical cyclone motion and evolution in vertical shear.* J. Atmos. Sci., **53**:3313–3332, 1996.

Wernli, H. and H. C. Davies: *A Lagrangian-based analysis of extratropical cyclones. I: The method and some applications.* Q. J. R. Meteorol. Soc., **123**:467–489, 1997.

Wolff, C. A., M. M. Bell and W. C. Lee: *Automatic Quality Control of Airborne Doppler Radar Data.* 34th Conference on Radar Meteorology, 2009.

Acknowledgements

My studies and this thesis benefited from the help of several people. To thank all of them is a particular concern of mine.

First of all, I am deeply grateful to Prof. Dr. Sarah Jones for trusting me with a challenging topic, for the facilitation of a stay abroad in the United States, the participation in conferences and resulting numerous contacts, as well as enlightening discussions and an extensive supervision.

I would also like to thank Prof. Dr. Christoph Kottmeier for agreeing to review this thesis.

I am very grateful to Prof. Dr. Pat Harr for an excellent mentoring in Monterey (USA), numerous advices and uncounted discussions. I also would like to kindly thank Dr. Michael Bell for providing the SAMURAI software, a lot of tips and tricks of handling radar data and SAMURAI, as well as for proofreading this thesis in advance. Many thanks to Dr. Chris Davis for inspiring discussions. I am grateful to the Helmholtz Association for funding the stay at Naval Postgraduate School in Monterey as part of the ATMO-Program. Thanks go to all members of the research group for new ideas and suggestions during numerous group sessions. In particular I would like to thank Christian Grams for his continuous support when having problems with applied software, as well as Simon Lang for providing several bytes of ECWMF data. I would also like to thank all the other colleagues at the IMK who supported me throughout my studies.

Many thanks to my co-students for creating a continuous pleasent working atmosphere. In particular I would like to thank Annette for an uncomplicated time in the United States and the friendly takeover of several time-consuming, organizational matters.

Last but not least I would like to express my gratitude to my parents, who supported me financially and mentally throughout my whole studies. Many thanks also to my brothers Manuel and Jannis for being there when I needed their help. Finally, I would like to thank Colli for lots of encouraging words and countless wonderful, recreative weekends.

Danksagung

Viele Personen haben mich während meines Studiums und vor allem während der Anfertigung der Diplomarbeit auf verschiedenste Art und Weise unterstützt. Bei diesen möchte ich mich an dieser Stelle herzlich bedanken.

Mein herzliches Dankeschön gilt Prof. Dr. Sarah Jones für eine herausfordernde Aufgabenstellung, die Ermöglichung meines Aufenthaltes in den Vereinigten Staaten, Teilnahme an Konferenzen, sich daraus ergebenden Kontakten, sowie aufschlussreichen Diskussionen und nicht zuletzt eine umfassende Betreuung.

Prof. Dr. Christoph Kottmeier danke für die freundliche Übernahme des Korreferates.

Für die großartige Betreuung in Monterey (USA), zahlreiche Ratschläge und unzählige Diskussionen möchte ich mich bei Prof. Dr. Pat Harr bedanken. Ebenso gebührt ein großes Dankeschön Dr. Michael Bell für das Bereitstellen der SAMURAI Analysemethode, vielen Tipps und Tricks im Umgang mit Radardaten und SAMURAI und die kritische Durchsicht einzelner Teile dieser Arbeit vor der Fertigstellung. Ebenso möchte ich mich an dieser Stelle bei Dr. Chris Davis für inspirierende Gespräche bedanken. Bedanken möchte ich mich bei der Helmholtz-Gemeinschaft für die Finanzierung meines Aufenthaltes an der Naval Post Graduate School in Monterey im Rahmen des ATMO-Programmes.
Vielen Dank auch an die Mitarbeiter der Arbeitsgruppe, die in den Gruppensitzungen immer wieder neue Ideen und Anregungen einbringen konnten. Besonderer Dank gilt Christian Grams für die stetige Unterstützung bei Problemen mit verwendenten Programmen, sowie Simon Lang für das Besorgen von ECMWF-Daten. Vielen Dank auch an alle anderen Kollegen am IMK, die mich während meines Studiums unterstützt haben.
Ein Dankeschön auch an meine Kommilitonen im Diplomandenraum, die stets für eine nette Arbeitsatmosphähre gesorgt haben. Besonderer Dank an Annette für die unkomplizierte Zeit in den USA und die Übernahme einiger zeitraubender, organisatorischer Angelegenheiten.

Meinen Eltern danke ich, da ohne deren großartige Unterstützung, sowohl finanzieller als auch moralischer Art, dieses Studium nicht möglich gewesen wäre. Auch meinen Brüdern Manuel und Jannis danke ich dafür, dass sie mir jederzeit hilfsbereit zur Seite standen. Nicht zuletzt danke ich meiner Freundin Colli für die aufmunternden Worte und für die vielen wunderschönen und erholsamen Wochenenden.

Erklärung

Hiermit erkläre ich, dass ich die vorliegende Arbeit selbst verfasst und nur die angegebenen Hilfsmittel verwendet habe.

Ich bin damit einverstanden, dass die Arbeit in die Bibliothek eingestellt wird und vervielfältigt werden darf.

Julian Quinting

Karlsruhe, den 17. Oktober 2011